CAVITY-ENHANCED NANOPHOTONIC SPECTROSCOPY IN OPTOFLUIDIC DEVICES

A Dissertation

Presented to the Faculty of the Graduate School

of Cornell University

in Partial Fulfillment of the Requirements for the Degree of

Doctor of Philosophy

by

Arthur Nitkowski

May 2011

CAVITY-ENHANCED NANOPHOTONIC SPECTROSCOPY IN OPTOFLUIDIC DEVICES

Arthur Nitkowski, Ph.D.

Cornell University 2011

The devices fabricated and explored in this thesis belong to an emergent research field referred to as optofluidics. Research innovations in the areas of integrated optics and microfluidics have brought forth this new and exciting area of study which combines photonics with fluid handling on the microscale. By taking advantage of tools designed for the microelectronics industry, optofluidics promises new innovations which may revolutionize the areas of diagnostic medicine, drug discovery, and environmental monitoring. In this thesis, I have explored how one of the main building blocks of photonics–the optical cavity–can be combined with microfluidic handling capabilities to perform spectroscopic measurements for life science applications.

This dissertation is divided into seven chapters with the following organization. In Chapter 1, I introduce the research field of optofluidics and its application in lab-on-a-chip technologies. Chapter 2 includes a motivation for the use of optical microcavities in biomedical sensing applications. I discuss the relevant parameters which describe the behavior of microring resonators and derive the equations governing their operation. Chapter 3 describes an experiment where polystyrene microspheres were optically trapped by the evanescent field from high index contrast silicon nitride waveguides. The use of a high-power broadband light source enables the simultaneous trapping, transport, and characterization of these microspheres by using their resonant properties. Chapter 4

discusses the use of optical microcavities to perform integrated laser absorption spectroscopy on nanoliter volumes of fluid. Relying on the cavity enhancement of light by silicon microrings, I demonstrate a sensitive and compact device which measures optical absorption in the near infrared regime. In Chapter 5 I demonstrate spectrophotometry measurements at visible wavelengths using microring resonators. Absorption products catalyzed by enzymes commonly used in bioassays are measured with microring resonator sensitive to the activity of individual enzymes. Chapter 6 builds on the work of the previous chapters to demonstrate microring measurements of optical absorption generated by bacteria growth. Results show the platform can be useful for fundamental studies on single bacteria. The final chapter includes a summary of the work and an outlook on the future of lab-on-a-chip devices.

BIOGRAPHICAL SKETCH

Arthur Nitkowski grew up in Randolph, New Jersey. He graduated from Cornell University in 2002 with a bachelor of science degree in engineering physics while a member of Professor Alex Gaeta's nonlinear optics group. Arthur then worked on adaptive optics for high-power laser propagation at the Massachusetts Institute of Technology's Lincoln Laboratory. In 2006, he returned to Cornell to pursue his graduate degree in applied physics and received his masters of science degree in 2010. Under the supervision of Professor Michal Lipson, Arthur has worked on several projects in the nanophotonics group with a focus on combining integrated optics with microfluidics for biomedical and life science applications.

For my loving wife and son.

ACKNOWLEDGEMENTS

My time at Cornell has been an enlightening experience, both professionally and personally. I would like to thank all the people that I have had the pleasure to work with that have made my graduate experience so memorable and rewarding.

My greatest thanks goes to my advisor and mentor, Professor Michal Lipson, who has been an incredibly enthusiastic and motivating supporter of my research. I am very grateful for her guidance and for allowing me to pursue my interests which have often been outside the normal focus of our group. Through our many meetings, discussions, paper revisions, and presentation practices, she has challenged me to become a better scientist and I am in awe of her dedication to our field. She has cultivated a research group where everyone is willing to help each other succeed, and this has had an enormous positive impact on my own work.

I would also like to thank my committee members, Professor Lois Pollack and Professor Antje Baeumner for their support and guidance during my graduate studies. Especially to Prof. Antje Baeumner, I would like to thank her for all our discussions and her invaluable insights into how my photonics research could be applied to the life sciences. She has been incredibly patient and helpful in expanding the scope of my research.

I also owe my thanks to Professor David Erickson for his support during the first years of my graduate studies. He provided access to his students and lab space which enabled the microfluidic components of my work. His insights into interesting area of research in biophotonics were very helpful in guiding my work.

I would also like to thank Professor Alex Gaeta who was my undergraduate

advisor at Cornell and allowed me to work in his nonlinear optics group. He oversaw my first research experience in optics which helped inspire me to continue working in this field. He encouraged me to pursue my graduate studies and I am very grateful for his early support.

This material is based in part on work supported by the IGERT Program of the National Science Foundation under Agreement No. DGE-0654112, administered by the Nanobiotechnology Center at Cornell. I would like to thank Professor Christopher Umbach and Professor Christopher Ober for allowing me to participate in the Integrative Graduate Education and Research Traineeship program. The ability to interact and communicate with students from diverse academic backgrounds was an enriching professional experience.

I am also thankful to all the members of the nanophotonics group that I have had the pleasure of sharing my time here with. I would not have been able to accomplish nearly as much without the considerable help of my experienced and intelligent colleagues. Special thanks are due to the people whose research had a direct and considerable impact on my own: Bradley Schmidt, Long Chen, and Sasha Gondarenko. To past group members: Qianfan Xu, Stefan Preble, Jacob Robinson, Po Dong, Bernardo Kyotoku, Danilo Spadoti, and Sasikanth Manipatruni—thank you for the knowledge and skills you passed down before you left. I would like to thank all the current members of the group, many of whom I consider close friends: Carl Poitras, Jaime Cardenas, Gustavo Wiederhecker, Mohammad Soltani, Michael Menard, Kyle Preston, Jacob Levy, Nicolas Sherwood Droz, Hugo Lira, Debo Olaosebikan, Lian-Wee Luo, Lucas Gabrielli, Biswajeet Guha, Taige Hou, Mian Zhang, Daniel Lee, Shreyas Shah, Lawrence Tzuang, and Vishal Chandrasekar.

The interdisciplinary nature of my research has provided me the opportunity

to collaborate with talented individuals from other research groups. I would also like to thank Sudeep Mandal and Allen Yang from the group of Prof. David Erickson for their advice in microfluidics. Thank you also to Barb Leonard from Prof. Antje Baeumner's group for her help in microbiology.

I would also like to thank all the staff and administrators in the departments of Applied Physics, Electrical and Computer Engineering, the Cornell Nanofabrication Facility, and the Nanobiotechnology Center. This work was performed in part at the Cornell NanoScale Facility, a member of the National Nanotechnology Infrastructure Network, which is supported by the National Science Foundation.

Finally, a special and heartfelt thanks is due to the most important people in my life, my family. I would like to thank my parents for their endless loving support and hard work so that I could be afforded all the opportunities to succeed in my endeavors. Thank you to my brother for helping to make me the competitive nut I am today. Thank you to my uncle for inspiring me to pursue a career in science and engineering. Finally, thank you to my wonderful wife, who is my best friend and my most enthusiastic supporter, and to our son Owen—you have both brought more joy and meaning to my life than I could have ever imagined.

TABLE OF CONTENTS

LIST OF TABLES

LIST OF FIGURES

CHAPTER 1

INTRODUCTION

1.1 Lab-on-a-chip technologies

The ability to scale down multiple laboratory processes onto a single chip format would enable highly functional and portable devices for life science applications. These 'lab-on-a-chip' technologies would take the place of many separate laboratory bench-top components and integrate them onto a chip that is less than a few centimeters in size. This high level of integration is made possible by lithography techniques borrowed from the microelectronics industry. By leveraging these microscale fabrication techniques, lab-on-a-chip devices are able to integrate fluidic, electrical, and optical capabilities onto a planar platform and perform highly parallelized and high throughput measurements. Because the devices are compact, these chips will enable field measurements in settings currently inaccessible by current environmentally sensitive laboratory equipment. Lab-on-a-chip technologies have the potential to revolution the way chemical analysis, environmental monitoring, and medical diagnostics are currently performed.

Specific areas of research where lab-on-a-chip devices have been developed include biochemical assays [5], immunoassays [6, 7], dielectrophoresis [8], sample preparation [9], genomics [10], proteomics [11], and drug development [12]. Devices are being developed to inexpensively and quickly sequence an entire human genome for diagnostic purposes [13]. Another embodiment can analyze and detect pathogens in blood samples using credit-card size instruments [14]. The promise of cheap and portable laboratory diagnostic devices can have an

enormous impact on global health in resource-limited countries [15]. Intense research in this area has resulted in more complex tools being added to the suite of lab-on-a-chip capabilities.

With all these potential applications and the considerable progress made in the development of lab-on-a-chip devices, it is surprising that they are not yet widely used and commercially available. Transitioning from academic laboratories and proof-of-concept demonstrations to commercial products has been slow. Some of the challenges are common to all new technologies such as issues dealing with intellectual property ownership and large costs of initial development. Another important factor, however, is that many lab-on-a-chip device demonstrations are not easily separated from the lab environment; these devices still require macroscale laboratory equipment or the attention of skilled laboratory technicians to operate. For devices which require optical detection, these devices still rely on the use of a large, complex, and expensive microscopes to perform the measurements or act as a detector [16]. In order to fully realize the potential of these technologies, they need to be integrated with all the necessary components required to operate them [5]. One of the most important and fundamental set of functions needed to enable versatile lab-on-a-chip devices are those which combine microfluidic handling capabilities with optical interrogation methods [17]. For the measurement techniques which rely on photonics, such as absorption [18, 19] and Raman spectroscopy [20], refractometry [21, 22], fluorescence detection [23], optical trapping [24], etc, the field of nanophotonics enables seamless integration with microfluidic technologies.

Optofluidic technologies have been demonstrated using a number of different fabrication techniques and material systems. In this dissertation, I have

investigated the combination of soft lithography microfluidic processing with high index contrast waveguides to develop fully integrated optofluidic devices. I discuss these two separate research fields below and the advantages of combining these two specific platforms.

1.2 Microfluidics

Microfluidics involves the manipulation of minute volumes of fluids using microscale channels. The control of fluid volumes ranging from 10^{-9} to 10^{-18} liters is performed using fabricated channels with dimensions on the order of 1 to 100 microns [25, 26]. The main applications for this area of research have been in fluid analysis, however many new areas have been explored ranging from chemical synthesis [27] to adaptive optics [28].

Shown in Fig. 1.1 is an example of a device [1] which demonstrates the scale typical of microfluidic devices as well as the level of integration possible. Intricate plumbing networks with robust capabilities can be fabricated on chips that fit easily in one's hand. Various fluidic handling building blocks have been demonstrated within a microfluidic platform including channels [29], pumps [30], valves [30], mixers [31], and splitters [32].

Fluids in this regime follow the same physics principles as fluids on the macroscale described by the Navier-Stokes equations, however, they exhibit a few unique characteristics which result due to their microscale confinement [33]. Microfluidic flow is laminar; the fluid flows in parallel layers. This is a result from viscous forces in the fluid dominating inertial forces, and therefore there is no turbulence. Laminar flow simplifies the design and simulation of microflu-

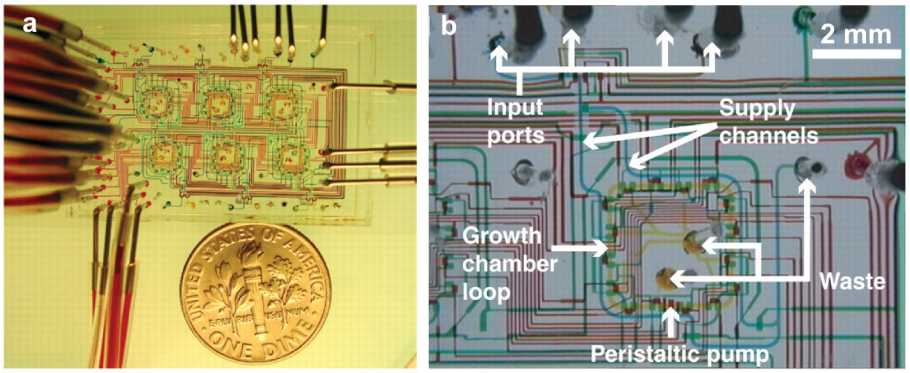

Figure 1.1: (a) Optical micrograph of a microfluidic device for bacteria growth. Microchannels are filled with food dye to show the size and density of the fluidic network. (b) Zoom-in of same device showing various integrated elements of the microbioreactor. Images reproduced from ref. [1].

idic flow, but adds some challenges. Mixing fluids, a common procedure for many applications, is diffusion-driven without turbulence and is less efficient [34]. Another unique characteristic is that surface tension is very strong on the microscale and capillary phenomena play an important role in the operation of devices [35].

Much of the potential of microfluidics is a result of the manner in which the devices are fabricated. Using photolithography techniques borrowed from the microelectronics industry, microfluidic devices have feature sizes on the order of microns. This degree of compactness allows the possibility of massively parallel measurements to be performed simultaneously and therefore reducing analysis time. Small feature sizes also translates to lower analyte and reagent consumption which is can reduce operating costs. Since multiple functionalities can be automated together, there is less need for trained personnel to operate them. Miniaturization of these devices makes them more portable, with the hope that they can be used in the field and in clinical settings. Just as the price of inte-

grated circuits is reduced by economies of scale of the microelectronics industry, the cost of microfluidic devices can be reduced by their mass-production. The use of soft polymers has the advantage of being bio-compatible, and prototyping of devices can be done quickly and inexpensively [36] .

1.3 Integrated optics

Integrated optics aims to develop miniaturized and versatile photonic circuits onto a planar substrate [37]. In these 'circuits', the familiar metallic wires of electronics are replaced with channel waveguides and the electrons which result in current flow are replaced by photons. The invention of the laser in 1960 provided a stable coherent source for the transmission and processing of signals using light. Lasers can be transmitted through air and manipulated with mirrors, lenses and prisms but these components are bulky and susceptible to environmental fluctuations. In the late 1960s, the field of integrated optics began to emerge for information technology applications in parallel with efforts to reduce losses within optical fibers [38]. Fabrication techniques have continually improved leading to smaller and more integrated optical components. Current lithography technology enable nanophotonic devices which have spatial features on the order of 10's of nanometers [39]. While the main driver for the advancement of integrated optics has been for the application of optical communication and signal processing, sensing applications have more recently received considerable interest [40].

Some of the main components which make up integrated optical circuits of devices include waveguides [41], splitters [42], couplers [43, 44], resonators

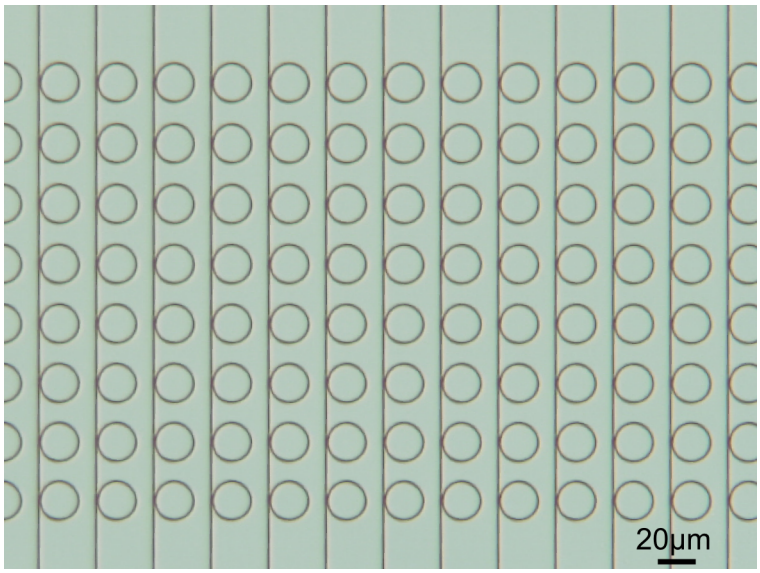

Figure 1.2: High index contrast waveguides can be used to make compact, highly parallelized integrated optical circuits. Shown is an optical micrograph of an array of over 100 silicon nitride microring resonators.

[45] and interferometers [46]. A scanning electron micrograph of an array of integrated optical microcavities is shown in Fig. 1.2 demonstrating the level of integration possible with these components. Active devices which incorporate electrical connection have also been demonstrated including electro-optic modulators [47], semiconductor lasers [48], optical amplifiers [49], and integrated detectors [50]. Many types of integrated optic sensors have been demonstrated including temperature [51], humidity [52], and pressure sensors [53].

Optical waveguides confine light due to total internal reflection at the walls. They can be made out of a variety of materials, provided that they are optically transparent in the wavelength range of interest and they have a higher refractive index than the materials around it. For dielectric materials, light propagating through a waveguide extends outside the waveguide material into its

surrounding. The level of confinement is determined by the refractive index contrast between the core guiding material and the outer cladding [54]. The presence of this evanescent field enables these structures to detect changes in the materials covering the waveguide [55]. High refractive index materials can confine light to smaller dimensions since the wavelength λ_o of light is decreased by the material index n by $\lambda = \frac{\lambda_o}{n}$. The decay length of the evanescent field is also inversely proportional to the index contrast. These properties lead to more compact devices capable of tighter bending radii and therefore a much higher level of integration [56].

For these reasons, the research presented here has concentrated on high refractive index material systems. For the near infrared, silicon is an ideal material due to its very high refractive index (n=3.5) and its fabrication maturity due to its use in the microelectronic industry. The band gap of silicon is 1.1 eV and it therefore absorbs light below ~1100 nm. Many applications in the life sciences use visible light (400-700 nm) and for these applications silicon nitride is an excellent waveguiding material. Silicon nitride is a commonly used insulator in microelectronics processing and has a high refractive index of n=2.0 and is transparent down into the UV spectrum [57, 58].

1.4 Optofluidic challenges

Microfluidics and integrated optics are very similar areas of research. They both fundamentally aim to miniaturize the handling capabilities for some type of medium (light or fluid), in order to form highly functional devices on a single platform. Fabrication is performed in a similar fashion, both using tools

and techniques from the microelectronics industry to achieve microscale and smaller spatial resolutions. They have in common many of the same potential advantages inherent with this type of processing including small size, low cost, increased throughput with parralelization, and portability. Yet their main applications are in vastly different fields, biomedical versus information technology. The form and processing commonalities shared between these fields make their combination especially elegant and seamless, while their disparate uses allow for new and unique applications that neither could accomplish individually.

Optofluidics, for all its potential, is not without its own set of challenges. For many applications, the sensitivity of a measurement does not scale favorably when dimensions are reduced to the microscale. One of the clearest examples of this is in the case of absorption spectroscopy measurements, which is one of the subject of study for much of this dissertation. Absorption spectroscopy involves shining light through a sample and measuring the transmitted intensity as a function of wavelength. The sensitivity of the measurement is directly related to the optical path length through the sample [59]. A detector will not be able to discern changes in intensity for a very weakly absorbing fluid unless the optical path through the sample is increased so that more light is absorbed. If I miniaturize a device to the microscale and limit the sample volume to less than a nanoliter, an optical absorbance measurements becomes very challenging because very little light is absorbed by the fluid.

In order to increase an optical devices sensitivity, integrated optics can draw upon techniques commonly used in free space optical systems to increase optical path length. Cavity enhanced absorption spectroscopy is a technique where a sample is placed within a cavity where light reflects back and forth many times

between mirrors [60]. Since the light makes multiple passes through the absorbing sample, the longer path length enables absorption measurements with higher sensitivity. This strategy can be applied to the microscale by using optical microcavities [61], which is the topic of the next chapter.

CHAPTER 2

MICROCAVITY RESONATORS

Optical microcavities are structures which allow light to build up due to feedback. In other words, light entering a cavity can constructively add to light already present within the cavity to increase the total intensity inside the structure. This condition is known as resonance, and it occurs for optical cavities of all sizes. Microcavities, however, differ from their large free space counterparts in that light can be confined to a much smaller volume, on the order of the wavelength of light [62]. This degree of confinement results in a range of new and interesting phenomena such as soliton effects [63], chaos [64], and enhancement or suppression of spontaneous emission [65]. These miniaturized structures can be used for applications ranging from fundamental research in quantum electrodynamics to commercial products in optical communications. Microcavities are well suited to magnify light/matter interactions and the research presented here takes advantage of this property. The subject of this dissertation is how microcavities can be used to enhance light interacting with minute volumes of fluid for life science applications [66].

There are a number of possible implementations of optical microcavities which can be generally divided into two groups: standing wave cavities and traveling wave cavities. Standing wave cavities have light patterns within them where the peaks and valleys of the optical wave remain in the same position within the cavity. Traveling wave microcavites have optical fields which circulate inside the cavity. These modes are called whispering gallery modes and the cavities and light propagates within them by total internal reflection at the boundaries. Fig. 2.1 shows a some of the commonly used integrated optical mi-

crocavities.

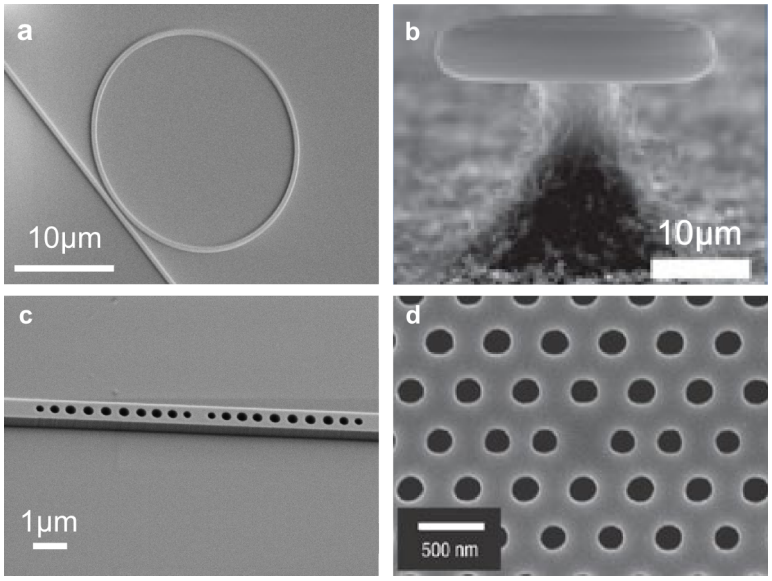

Figure 2.1: Scanning electron micrographs of various optical microcavities. (a) Microring resonator. (b) Microtoroid [2]. (c) One dimension photonic crystal. (d) Two dimensional photonic crystal nanocavity [3].

The research presented in the Chapters 4-6 takes advantage of resonant phenomena in ring resonator traveling wave cavities. These types of cavities are used due to their seamless integration with standard channel waveguides. They can be made low loss, their properties can be easily engineered to change their behavior, and their fabrication is less sensitive to processing errors than their photonic crystal counterparts. In the following sections I will cover the theoretical details governing the use of rings resonators as optical microcavities.

2.1 Microring resonator theory

In this section I derive the relevant equations which describe the performance of microring cavities. I also describe how the typical parameters used to characterize optical cavities can be reformulated in terms of microring resonator parameters. I loosely follow the derivation used in ref. [67, 68].

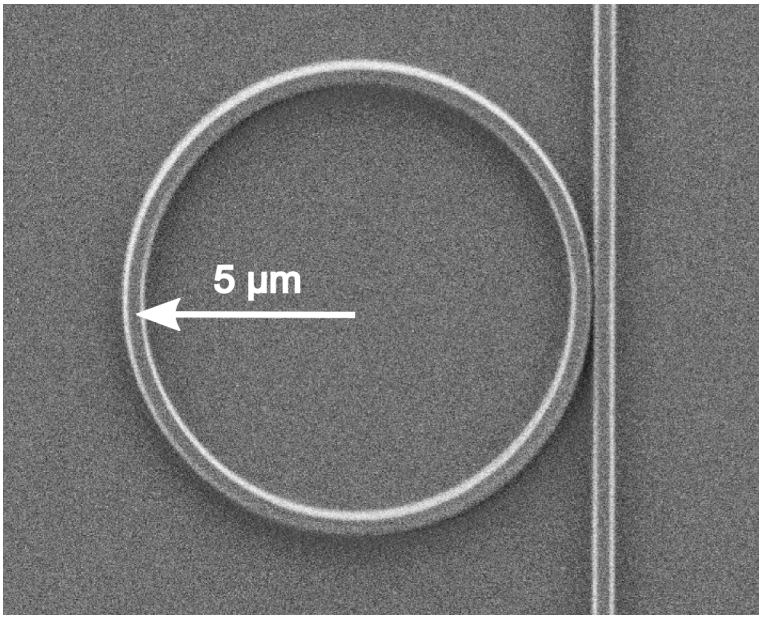

Figure 2.2: Scanning electron micrograph of a silicon nitride microring resonator. The vertical bus waveguide is used to couple light into the 5 µm radius microring cavity.

A scanning electron beam microscope (SEM) of the type of microring resonator used in this text can be seen in Fig. 2.2. The image shows a microring with 5 µm bending radius that has been coupled to a bus waveguide. Light input into one end of the bus waveguide will evanescently couple into the microring cavity. The coupling waveguide also provides an output where I can measure the response of the ring resonator to light input at varying wavelength.

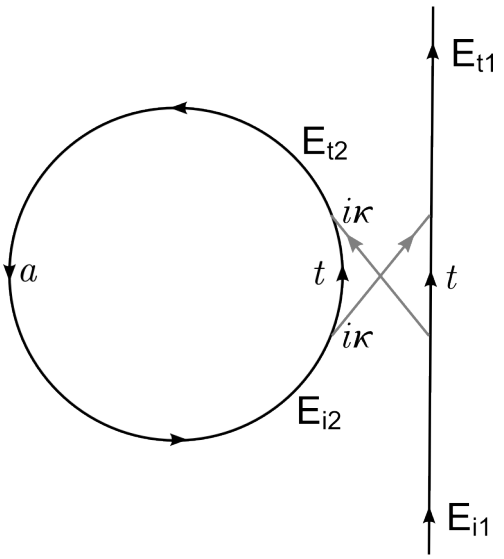

Figure 2.3: Diagram of a ring resonator and directional coupler.

If I only consider excitation and propagation from a single direction, as shown in Fig. 2.3, then the electric field magnitudes after coupling can be described by the following matrix:

$$\begin{bmatrix} E_{t1} \\ E_{t2} \end{bmatrix} = \begin{bmatrix} t & i\kappa \\ i\kappa & t \end{bmatrix} \begin{bmatrix} E_{i1} \\ E_{i2} \end{bmatrix} \tag{2.1}$$

where t and κ are the field transmission and coupling coefficients. For lossless coupling the following relation holds:

$$t^2 + \kappa^2 = 1 \tag{2.2}$$

Light will propagate around the ring while material absorption, bending losses, and surface scattering will lead to loss. These intrinsic losses are characterized by the field attenuation coefficient a shown in Fig. 2.2. Propagation in

the ring can then be described by

$$E_{i2} = ae^{i\theta}E_{t2} \tag{2.3}$$

where θ is the phase shift per round trip accumulated during propagation around the ring. The field magnitudes are normalized so that the input incident power $|E_{i1}|^2$ is equal to unity. Equations 2.1- 2.3 can be then be solved to determine the transmission characteristics of a ring and bus waveguide system. The power transmission at the output port of the bus waveguide is given by

$$P_{t1} = |E_{t1}|^2 = \frac{a^2 + t^2 - 2at\cos\theta}{1 + a^2t^2 - 2at\cos\theta} \tag{2.4}$$

The power circulating in the ring can similarly be found as

$$P_{i2} = |E_{i2}|^2 = \frac{a^2(1 - t^2)}{1 + a^2t^2 - 2at\cos\theta} \tag{2.5}$$

Considering Eq. 2.5, the maximum power in the ring occurs when

$$\theta = 2\pi n \tag{2.6}$$

where n is an integer. This is the resonance condition true for all optical cavities which occurs when the round trip phase shift is an integral number of 2π. The circulating power then can be described by

$$P_{i2} = |E_{i2}|^2 = \frac{a^2(1 - t^2)}{(1 - at)^2} \tag{2.7}$$

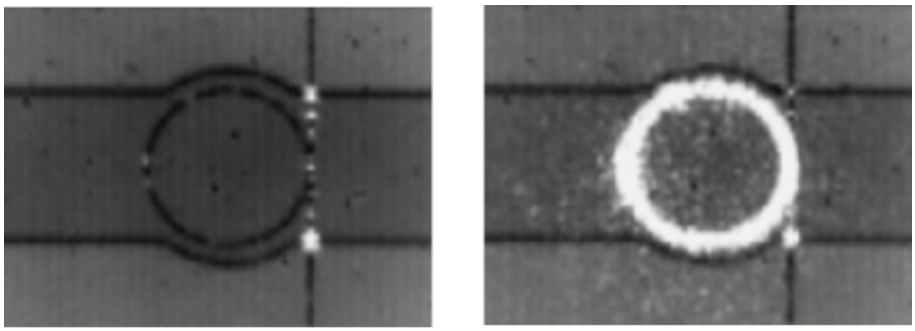

Figure 2.4: Top view microscope image of a silicon microring resonator with a vertical bus waveguide being excited at two different wavelengths but with the same optical power. Image (a) is off resonance while (b) shows the large intensity enhancement that occurs within the ring is on resonance. The horizontal lines are the edges of an oxide cladding which covers the bus waveguide.

As an illustrative example of the enhancement potential of a microring resonator, we can plug in values for the attenuation and transmission coefficients typically measured in the lab. The microrings described in Chapter 6 have coefficients $a \approx t \approx .995$. Plugging in these values into Eq. 2.7 we find the circulating power to be 100 times larger than the incident power in the bus waveguide. For microcavities which have lower losses, such as microdisks or microspheres, the resonant enhancement can be several orders of magnitude larger [21]. The intensity buildup is clearly evident in Fig. 2.4 which shows a microscope image of a 100 μm radius silicon microring being excited by infrared light at two different wavelengths corresponding to images (a) and (b). Due to surface roughness, a small fraction of light in the waveguide is scattered towards the camera showing the difference in the buildup of power when the ring is off and on resonance.

The transmission spectrum governed by Eq. 2.4 can be seen in Fig. 2.5 with ring coefficients typical of those measured for silicon nitride in the visible spec-

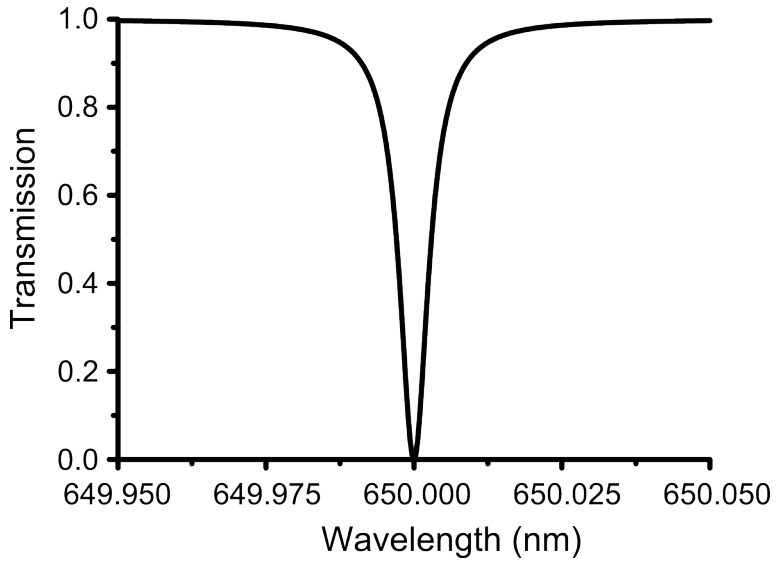

Figure 2.5: Simulated transmission spectrum of a 100 μm radius silicon nitride ring resonator with ring parameters $a = t = .9715$.

trum. When on resonance, the transmitted power measured at the output of the bus waveguide is at a minimum and Eq. 2.5 reduces to

$$P_{t1} = |E_{t1}|^2 = \frac{(a-t)^2}{(1-at)^2} \tag{2.8}$$

The minimum in the transmitted spectrum on resonance results from the interference between light in the ring coupling back to the bus waveguide (κE_{i2}) and transmitted bus waveguide light (tE_{i1}). The interference is destructive because of the total added π phase shift which occurs after coupling to and from the ring. Notice that when the condition

$$a = t = \sqrt{1-\kappa^2} \tag{2.9}$$

is satisfied, which occurs when the losses due to propagation in the ring are

equal to the losses due to coupling, then the transmitted power goes to zero. This condition is called critical coupling and is important because the transmission function (Eq. 2.4) is most sensitive to any changes in its dependent variables, a and t. This means any change in the losses or coupling of ring will have the largest effect on the shape of the resonance curve. For this reason, microring resonators are designed to be critically coupled for most sensing applications.

In order to maximize sensitivity of the rings for sensing applications, we not only want to operate near critical coupling, but we also want to minimize the propagation losses in the ring. The lower the propagation loss, the longer light circulates in the ring and the greater the interaction between the evanescent field of the ring and the environment which we are probing. The linewidth of the resonance, which we would like to minimize for various spectroscopy applications, is also related to the propagation losses. Several parameters are useful to quantify these various characteristics of the microring including the quality factor Q of the cavity. The quality factor is a dimensionless parameter which is a measure of the energy stored at resonance versus the energy lost per cycle [69]. Therefore light in a high quality factor cavity will decay more slowly, ie. have a longer photon lifetime as described by

$$Q = \omega\tau \tag{2.10}$$

where ω is the angular frequency ($\omega = 2\pi f$) and τ is the photon lifetime. The photon lifetime can be measured by sending a pulse into the cavity and looking at the decay of the pulse in the bus waveguide transmission. For the experiments described in the subsequent chapters, a continuous-wave tunable laser is used to measure the transmission spectrum of our devices. The quality

factor can then be deduced from the relation

$$Q = \frac{\lambda}{\Delta\lambda} \tag{2.11}$$

where λ is the free space wavelength and $\Delta\lambda$ is the full width at half maximum (FWHM) linewidth of the resonance. Quality factors on the order of 1×10^5 are typical of the microring structures fabricated in silicon and silicon nitride for this text. These high quality factors allow us to make very compact devices with high sensitivities to environmental changes.

The wavelength position of the resonance is important since we would like to design the microrings to operate at certain frequencies. The resonance condition described in Eq. 2.6 can be rearranged as

$$m\lambda = 2\pi R n_{eff} \tag{2.12}$$

where m is an integer, λ is the resonance wavelength, and R is the ring radius, and n_{eff} is the effective index. Eq. 2.12 simply states that resonance occurs when an integral number of wavelengths fits with the circumference of the ring. The effective index of the mode is normally calculated using a finite element mode solver and quantifies the increase in the vacuum wavenumber $k = {}^{2\pi}/_{\lambda}$ which light experiences when propagating through the waveguide material. This leads to a propagation constant $\beta = kn_{eff}$ which may be complex to include loss. The phase velocity of light in the waveguide is therefore $v_p = {}^{c}/_{n_{eff}}$ where c is the speed of light in vacuum. The effective index at a particular wavelength determines whether that wavelength is a resonance, however the effective index is also a function of wavelength which must be taken into ac-

count when evaluating, for example, Eq. 2.4-2.5. This wavelength dependence is included in the following relation for the group index

$$n_g = n_{eff} - \lambda \frac{\partial n_{eff}}{\partial \lambda} \tag{2.13}$$

The wavelength separation between consecutive resonances, also known as the free spectral range (FSR), can be determined from Eq. 2.12-2.13.

$$FSR = \frac{\lambda^2}{n_g L} \tag{2.14}$$

where L is equal to the circumference of the ring, $L = 2\pi R$. Note that Eq. 2.14 differs from the usual equation for the FSR of a Fabry-Perot cavity by the lack of a factor of 2 in the denominator. This is because light makes only a single pass in one round trip of a ring but makes two passes due to reflection at an end mirror of a Fabry-Perot cavity. Since the FSR can be directly measured experimentally, the group index can be determined without the need for simulation which can be useful when calculating various properties of the microring.

The filtering ability of the ring is characterized by the finesse, F, of the microcavity which is

$$F = \frac{FSR}{\Delta\lambda} \tag{2.15}$$

where $\Delta\lambda$ is again the FWHM of the resonance linewidth. The quality factor and finesse of a microring cavity can also be expressed in terms of the field coefficients from Eq. 2.1-2.3. For the case of critical coupling where Eq. 2.9 is satisfied, the quality factor can be shown [70] to satisfy

$$Q = \frac{\sqrt{ta}L\pi n_g}{(1-ta)\lambda_o} \tag{2.16}$$

which is the loaded quality factor of the cavity. The loaded quality factor depends on the internal losses as well as losses from coupling. The intrinsic quality factor, which is twice the loaded quality factor at critical coupling, excludes losses from the addition of the bus waveguide and is therefore a measure of the cavity itself. The intrinsic quality factor can be described by

$$Q_i = \frac{2\pi n_g}{\alpha\lambda_o} \tag{2.17}$$

where we have introduced the familiar power absorption coefficient α. The field attenuation coefficient a is related to the absorption coefficient by the formula

$$a = e^{-\alpha\pi R} \tag{2.18}$$

where R is again the radius of the ring. Eq. 2.17 provides an easy formula to determine what propagation losses need to be reduced to during fabrication to achieve a given Q, or conversely what the losses in the ring are for an experimentally measured Q. Similarly, the finesse of the microcavity can be described in terms of the the ring coefficients. At critical coupling and low loss, ie. $a = t \approx 1$ the finesse can be described by

$$F = \frac{\pi}{\kappa^2} \tag{2.19}$$

Under these conditions, the circulating power described by Eq. 2.7 can be simplified and expressed in terms of the finesse as:

$$P_{i2} = |E_{i2}|^2 = \frac{1}{\kappa^2} = \frac{F}{\pi} \tag{2.20}$$

which shows the cavity finesse is not only a measure of the filtering capabilities of the ring based on its definition, but also scales with the circulating power in the microcavity.

CHAPTER 3

ON-CHIP SUPERCONTINUUM TRAPPING WITH MICROSPHERES

In this chapter I demonstrate the simultaneous optical manipulation and analysis of microscale particles in a microfluidic channel. Whispering gallery modes (WGMs) in dielectric microspheres are excited using the evanescent field from a silicon nitride waveguide. A supercontinuum source is used to both trap the microspheres to the surface of the waveguide and excite their resonant modes. All measurements are in-plane, thus providing an integrated optofluidic platform for lab-on-a-chip biosensing applications[1].

3.1 Integrated optical trapping introduction

Optical trapping has been demonstrated as a critical tool for the manipulation of microscale particles for many biological applications [72]. Furthermore, it has been shown that the combination of optical trapping forces with the precise control provided by microfluidics can produce optofluidic devices with increased functionalities [73]. Recent progress in this area has included various devices to generate the near field intensity gradients required to achieve optical trapping [74, 75, 76, 24]. In most realizations of optical manipulation, a single narrowband light source is utilized. I show the use of broadband light to generate optical forces on an integrated structure as a tool for the characterization of microscopic objects. To demonstrate an application that takes advantage of the broadband nature of our source, I investigate the spectral response of trapped microspheres in a microfluidic environment.

[1] Portions of this chapter are reproduced with permission from [71]

The ability to simultaneously manipulate and characterize a single microscopic object is an important functionality for biomedical applications [77]. The platform demonstrated here utilizes both microfluidic flow and optical forces from a broadband source to position dielectric microparticles for individual analysis. Following transport within a microfluidic channel, the particle position is controlled by optical forces generated by a waveguide evanescent field. These radiation forces, which are due to changes in the incident light momentum, can be decomposed into transverse and longitudinal components as shown in Fig. 3.1. The decay of the evanescent field intensity results in a gradient trapping force that attracts the particle to the waveguide [78]. Particle scattering and absorption of the incident light momentum leads to a radiation pressure force that propels the particles in the direction of light propagation [78]. Since the trapping light source is broadband, the spectral response of the trapped microparticle can be used for characterization.

Several design parameters were considered to ensure broadband operation and the generation of strong optical forces. The waveguiding material is stoichiometric silicon nitride Si_3N_4, which has low absorption in the visible and near infrared and allows fabrication of low-loss waveguides [79]. Silicon nitride's high refractive index n=2.0 relative to water n=1.33 leads to strong gradient-trapping forces. The dimensions of the waveguide are 200 nm tall by 2 μm wide, and nanotapers at the ends of the waveguides ensure that light couples into the fundamental quasi-TM waveguide mode. The light source is a commercially available supercontinuum (SC) source (Fianium SC-450) that generates a broad output spectrum 500 nm to 2.0 μm and high average powers 4 W. Due to the high degree of spatial coherence in the light source [80], the SC light can be efficiently focused down by a tapered lens fiber to mode match with the

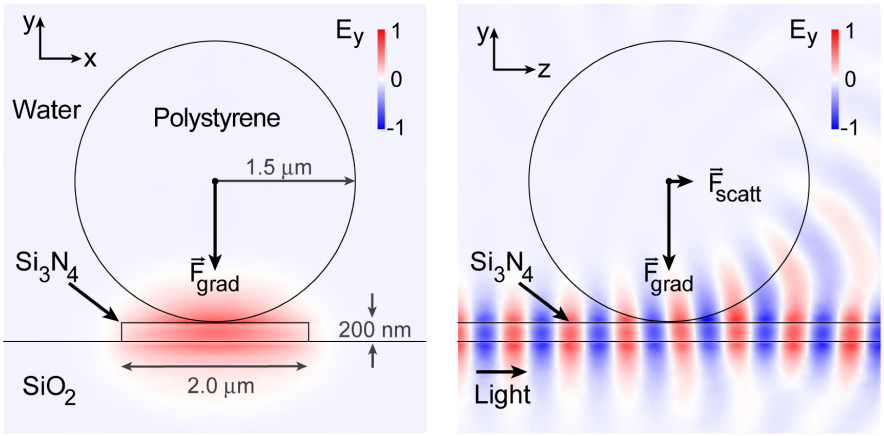

Figure 3.1: 3D simulation results for the electric field Ey profile of the quasi-TM mode at a wavelength of 850 nm in a silicon nitride waveguide. The optical forces on a dielectric microsphere can be decomposed into a transverse gradient force F_{grad} that traps the sphere to the waveguide surface and a longitudinal force F_{scatt} that propels it along the direction of light propagation (z axis).

waveguide nanotapers. The input spectrum of the SC source along with the waveguide transmission spectrum is shown in Fig. 3.2. I measure only a 10 dB power loss between the input and the output of the waveguide while efficiently coupling light at wavelengths across the near infrared spectrum.

3.2 Fabrication and methods

The optofluidic devices were fabricated using standard microlithography techniques. Details on the waveguide fabrication can be found in [79] and Appendix A, where the same process was used with demonstrated waveguide propagation losses of 0.1 dB/cm in the near infrared. Microfluidic channels

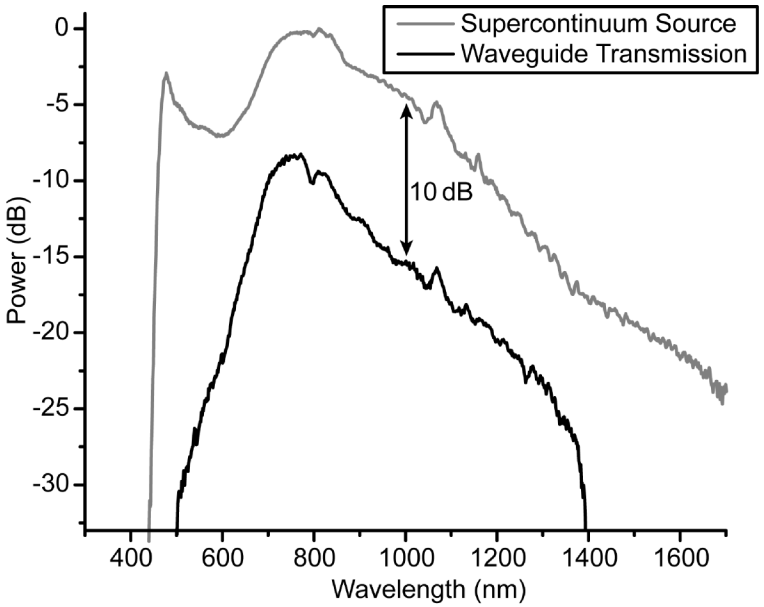

Figure 3.2: Spectra of the supercontinuum source and waveguide transmission showing efficient broadband coupling to the waveguide from 700 nm to 1400 nm.

with 30 μm height and 300 μm width were fabricated from polydimethylsiloxane (PDMS). Inlet and outlet ports for fluids were punched through the PDMS, and the channels were aligned orthogonal to the waveguide to allow passing microspheres to interact with the waveguide's evanescent field.

The experimental procedure requires coupling broadband light onto the photonic chip and measuring the waveguide's transmission spectrum and the setup is shown in Fig. 3.3. The free space output of the SC source is coupled into a single-mode polarization-maintaining fiber (Thorlabs P5-1550PM). The tapered fiber is butt coupled to the waveguide input and oriented to excite the waveguide quasi-TM mode. The waveguide output is collected with an achromatic microscope objective (Olympus Plan 40) and passed through a polarization analyzer (Newport 10GL08). The light is then coupled into a multi-mode

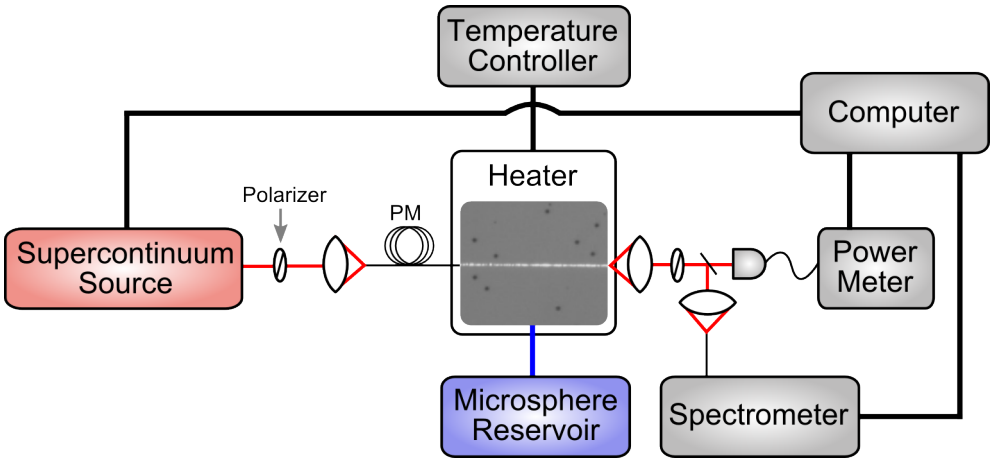

Figure 3.3: Schematic of the optical experimental setup used for optical trapping and whispering gallery excitation of polystyrene microspheres.

fiber and its spectrum measured with a spectrometer (Ocean Optics HR2000). Polystyrene microspheres (Duke Scientific n=1.59) of various diameters are prepared in deionized water with surfactant to prevent aggregation. The microsphere solution is injected into the microfluidic channels, and flow velocity is controlled by adjusting the height of the microsphere solution reservoir.

3.3 Demonstration of optical trapping, transport, and analysis

Microspheres of various diameters were flowed through the microfluidic channel and were optically trapped and transported by the waveguide's evanescent field. Fig. 3.4, along with its accompanying video (Media 1), shows the manipulation of 3μm diameter particles using broadband light with 10 mW of guided power. Optically induced damage to biomolecules should not be a concern for this system due to the relatively low optical powers used along with operation

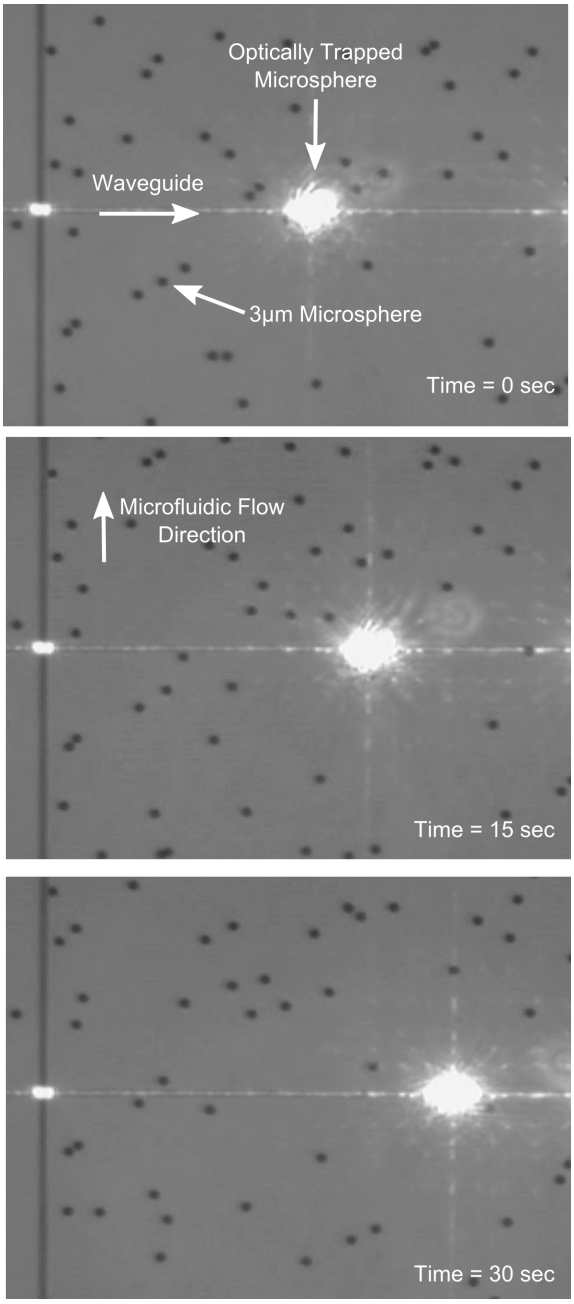

Figure 3.4: Optical trapping and transport of a 3 μm diameter polystyrene microsphere in a microfluidic channel using a supercontinuum broadband light source.

in the low-absorption near infrared regime [81]. Roughly 25% of the microspheres in this video are trapped by the waveguide; this trapping efficiency can be improved by decreasing the channel height, increasing the optical power, or slowing the flow speed. The optical forces on a polystyrene microsphere were calculated using 3D finite-element analysis with the Maxwell stress tensor formalism [76]; the simulated mode results are shown in Fig. 3.1. For a 3 μm diameter particle with 5 nm waveguide separation and 850 nm trapping wavelength, the gradient force and scattering force are 1.5 nN/W and 0.21 nN/W, respectively. These values are in good agreement with previous results obtained for silicon nitride waveguides [82]. The forces on the sphere decrease as the distance between the sphere and waveguide increases due to the decay of the evanescent field, as shown in Fig. 3.5. Trapping of microspheres with diameters ranging from 500 nm to 20 μm was observed.

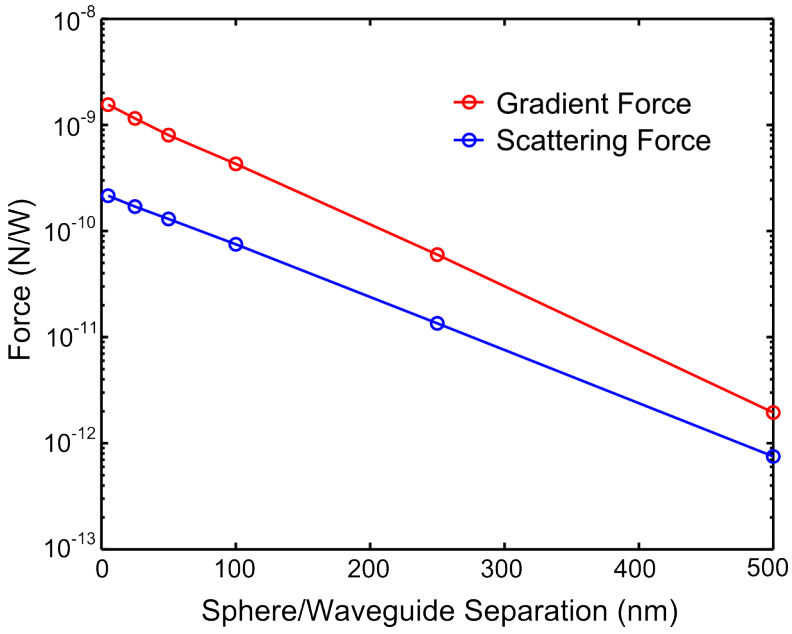

Figure 3.5: Gradient and scattering forces on a 3 μm diameter polystyrene sphere as a function of distance from a silicon nitride waveguide excited at 850 nm.

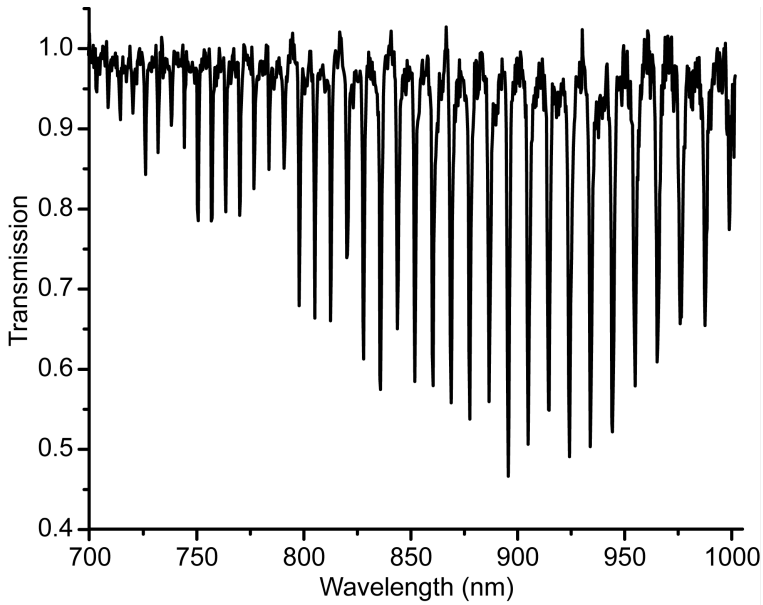

Figure 3.6: Waveguide transmission spectrum showing WGM resonances of an optically trapped 18 μm diameter polystyrene microsphere with quality factors of ~2,000.

Particles that are trapped by the intensity gradient of the broadband light source can be simultaneously analyzed by measuring the spectrum of the waveguide transmission. Fig. 3.6 shows the transmission spectrum of the waveguide while an 18 m polystyrene microsphere is trapped. The curve is normalized to the spectrum when no particle is present. The transmitted spectrum displays a series of dips that correspond to the whispering gallery mode (WGM) resonances of the trapped microsphere. Wavelengths that are integer multiples of the sphere circumference build up as a result of total internal reflection at the boundaries of the sphere. Fig. 3.7 shows the free spectral range measured using microspheres of different diameters. By controlling the microsphere concentration and fluid flow velocity, we trap single microspheres at a time to simplify the analysis of the transmitted spectra. The solid lines represent the theoretical curves for WGM resonances calculated using the known refractive indices of the

materials and the measured size of the particles [83]. The agreement between the data and the theoretical curves affirms that light is coupling into the fundamental resonant cavity modes of these microspheres. Therefore, not only is the broadband light being used to physically manipulate the particle, but it also provides a spectral signature of the interaction, allowing analysis of the particle. Changes in the resonance wavelength and linewidth can be used to sense changes in the local fluidic environment such as adsorption of biomolecules to the microsphere surface.

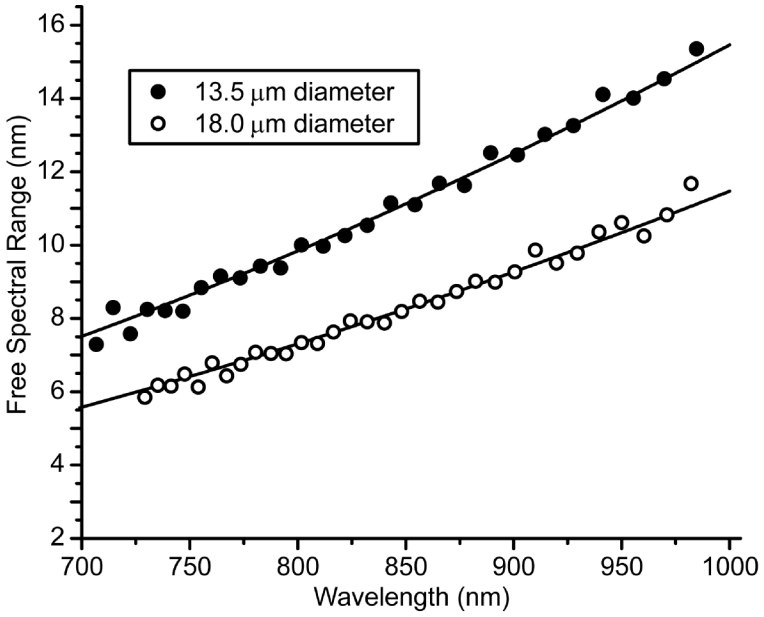

Figure 3.7: Experimental free spectral range (circles) in microspheres of different diameters with theoretical curves (solid lines) for WGMs in spherical cavities.

3.4 Summary

I have demonstrated the simultaneous optical trapping, manipulation, and analysis of single microscale particles using silicon nitride waveguides and a broadband supercontinuum light source. To the best of our knowledge, this is the first time a white-light source has been used for integrated optical trapping, which may enable new lab-on-a-chip biosensors with increased functionalities. Several broadband particle-characterization methods could be used in conjunction with the technology demonstrated here, including fluorescence and scattering spectroscopy [84] as well as coherent anti-Stokes Raman spectroscopy [85]. Measurements of WGMs in various structures have been used successfully to detect the binding of single biomolecules [86] including proteins with sub attogram molecular mass [21]. To date, coupling light into these high-quality-factor devices is done using a tapered optical fiber or a prism, and therefore a complete integrated system cannot be fabricated using standard photolithography techniques. The use of in-plane waveguide excitation of flowing microspheres presents a potential method to fully integrate WGM-based biosensors.

CHAPTER 4

CAVITY ENHANCED ABSORPTION SPECTROSCOPY

In this chapter I demonstrated on-chip laser absorption spectroscopy using silicon microring resonators integrated with PDMS microfluidic channels. A 100 μm radius microring resonator with Q> 100,000 is used to enhance the interaction length between evanescent light and a cladding liquid. I measure absorption spectra of less than 2 nL of N-methylaniline from 1460 nm to 1610 nm with 1 nm resolution and effective free space path lengths up to 5 mm. This work can help realize a completely on-chip spectroscopy device for lab-on-a-chip applications[1].

4.1 Integrated absorption spectroscopy introduction

Optofluidic techniques where microfluidics are integrated with photonic components are gaining widespread use in biosensing and chemical analysis applications [73]. Incorporating advanced fluid handling techniques at the micron scale with highly sensitive photonic devices has the potential to provide compact, effective sensors for lab-on-a-chip tools [87]. Many optofluidic transduction methods for sensing and analysis have been demonstrated including refraction [88], absorbance [89], fluorescence [90], surface-plasmon-resonance [91], and interferometric [92] measurements. Absorbance-based optofluidic techniques are particularly attractive since they offer the potential to provide label-free spectral information for detection and identification of an analyte [93]. However, the miniaturization of microfluidic devices reduces the optical path length for absorption based sensors as compared to macroscopic experi-

[1]Portions of this chapter are reproduced with permission from [19]

ments. A shortened optical path reduces the interaction length of light with a fluid and thus limits the sensitivity of a device and its ability to detect an absorbing species. Several methods have been proposed to mitigate this problem including using slow-light in photonic crystals [94] or novel waveguide geometries [95]. It has been shown that high quality factor cavities, both passive [96, 97, 98] and active [99], can be used to enhance the interaction length between the guided light and an analyte. Previous work has required large scale components thus negating much of the benefit of using a microresonator or has involved detection at a particular wavelength thus providing little spectral information. In this work I demonstrate both integrated and broadband absorption spectroscopy in the near infrared using microring resonators and microfluidic channels.

The proposed device is a silicon microring resonator covered by a microfluidic channel, as shown in Fig. 4.1(a). We design the device so that the evanescent light traveling in the ring resonator interacts with the upper fluidic cladding. At resonance, light circulates many times within the ring which leads to a large enhancement in the interaction length between the evanescent field and the cladding liquid. Any losses present in the fluid will alter the quality factor and extinction ratio of the transmission resonance. By extracting the absorption contribution from an analyte to a resonance and repeating this process for many resonances over a range of wavelengths, an absorption spectrum for an analyte can be measured.

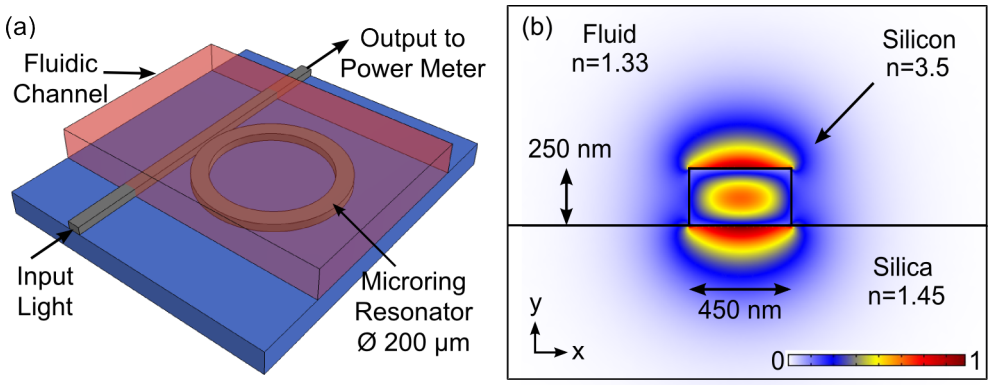

Figure 4.1: (a) Illustration of our device design with a straight waveguide coupled to a ring resonator and a microfluidic channel on top. (b) The electric field mode profile (y-component) for the quasi TM mode propagating in a silicon waveguide in an aqueous environment.

4.2 Absorption spectroscopy

Absorption spectroscopy refers to the technique of measuring the absorption of electromagnetic radiation by a sample as a function of wavelength. The sample may be in the solid, liquid or gas phase and the absorption spectrum provides a great deal of characteristic information about the sample. In this section I will cover the relevant terminology and clear up the different notations used in the literature for the absorption coefficient of a material.

A conceptual drawing of an absorption spectroscopy measurement in shown in Fig. 4.2 where a sample is illuminated by incident radiation of intensity I_o and the transmitted intensity I is measured by a detector. The transmittance of the sample is defined simply as the ratio of the intensities:

$$T = \frac{I}{I_o} \tag{4.1}$$

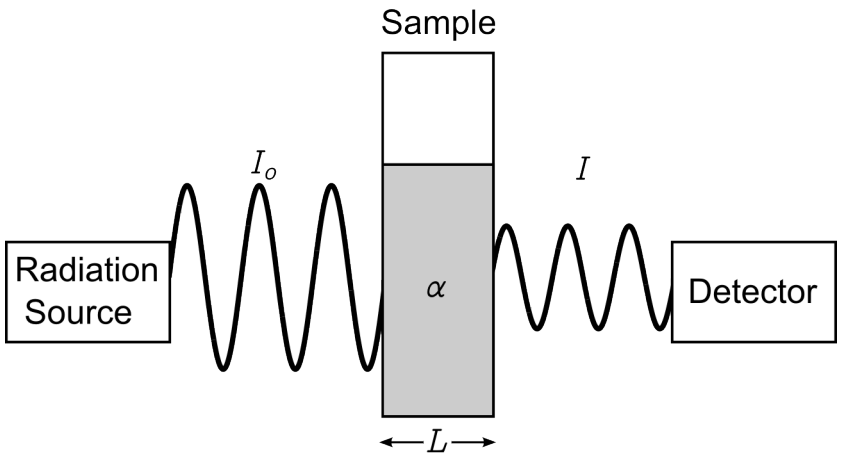

Figure 4.2: A typical absorption spectroscopy measurement consists of a source of light with intensity I_o passing through a sample with path length L and wavelength dependent absorption α. A detector then measures the decrease in the incident intensity I.

Due to the large variability of absorption between samples, it is often more convenient to express the change in intensity as the dimensionless quantity known as absorbance A, where

$$A = -log_{10}\frac{I}{I_o} = -log_{10}T \tag{4.2}$$

For each factor of 10 that the transmittance decreases, the absorbance of the sample increases by one. From Fig. 4.2 we can see that the transmitted intensity not only depends on the sample absorption, but also on the sample holder, specifically the path length L that light traverses through the sample. The relationship between the transmittance of a sample and the path length is described by the Beer-Lambert law. This law states that there is an exponential decay of transmitted radiation as a function of the path length L of a sample:

$$T = \frac{I}{I_o} = 10^{-\alpha L} \tag{4.3}$$

which also defines the absorption coefficient α as the per unit power loss coefficient of the material. The absorbance A can then be written simply in terms of the sample properties as

$$A = -log_{10}\frac{I}{I_o} = -log_{10}T = \alpha L \tag{4.4}$$

Confusion in the literature occurs because various fields use different definitions of the absorption coefficient α [100]. For liquids, Eq. 4.3 defines α, whereas for gases the alternate definitions are used:

$$T = \frac{I}{I_o} = e^{-\alpha' L} \tag{4.5}$$

and

$$A = -ln\frac{I}{I_o} = -ln\, T = \alpha' L \tag{4.6}$$

This definition is also used to quantify losses experienced by light propagating in a waveguide. Specifically

$$I = I_o e^{-\alpha_{wg} L} \tag{4.7}$$

where α_{wg} is the loss per unit distance for a waveguide. Note that α_{wg} therefore differs from the α in Eq. 4.3 used to describe liquids, which we rename as

α_{liquid}. Comparing Eq. 4.3 and 4.7, we find that

$$\alpha_{wg} = \alpha_{liquid}\, ln\, 10 \tag{4.8}$$

which can be used to convert between the two conventions. In the remainder of this text I will use the absorption coefficient definition described by Eq. 4.7 to describe losses in our integrated photonic devices, which is the convention.

4.3 Design and fabrication

The integrated absorption measuring device was designed to maximize interaction with a cladding fluid. The cross section of the ring and waveguide are 450 nm wide by 250 nm tall which supports a single mode at λ=1.5 μm. The resolution of our absorption spectroscopy device is determined by the free spectral range between resonances, therefore the ring radius (100 μm) was chosen to provide a FSR of ~1 nm. The y-component of the electric field mode profile for quasi TM polarized light with an aqueous upper cladding is shown in Fig. 4.1(b). The coupling distance between the bus waveguide and ring is 300 nm. The straight waveguides are oxide clad which provides a symmetric index profile to increase input light coupling through optical fiber and also reduces waveguide losses. The ring resonators are exposed (uncladded) which allows maximum interaction of the evanescent light trapped in the ring with any subsequent fluidic cladding.

The optical structure was fabricated using standard microfabrication techniques on a silicon-on-insulator wafer with a 3 μm buried oxide layer and

250 nm device layer. The devices were patterned with a JEOL electron beam lithography system and then etched using inductively coupled plasma etching. Lift-off resist and then photoresist were spun onto the wafer and patterned using contact lithography to mask the ring resonators. A 1.7 μm cladding layer of silicon dioxide was then evaporated over the wafer using an electron gun source and cryopumped evaporator. After dicing and polishing, the oxide and resist over the ring resonator were removed using Microposit Remover 1165 leaving the ring exposed (as shown in Fig. 4.3).

The microfluidic channels were made from PDMS using soft lithography processes. A master mold for the microfluidic channels was made by spin-coating SU-8 photoresist to a thickness of 30 μm on a silicon wafer. Using contact lithography, channels with a width of 300 μm were patterned onto the SU-8 including alignment marks to later align the channels to the photonic devices. PDMS was then poured over the mold and baked at 80 °C for several hours. The PDMS was then cut and peeled off the master wafer and holes were punched through the PDMS to act as inlet and outlet ports for fluids. The chip and fluidics layer were then oxygen plasma cleaned before a contact aligner was used to irreversibly bond the PDMS to our device chip. Finally, we connect Tygon tubing to the microfluidic channel inlets to allow fluid to be introduced into the channel. Detailed fabrication instructions can be found in Appendix A. The completed device is shown in Fig. 4.3 and includes over 50 waveguides and ring resonators with their output offset by 3 mm to prevent input light from scattering into the output light detector. A microfluidic channel connects the two inlets and crosses the ring resonators that are coupled to each waveguide. The required volume of fluid to cover a single ring resonator with the channel size used for this device is less than 2 nL.

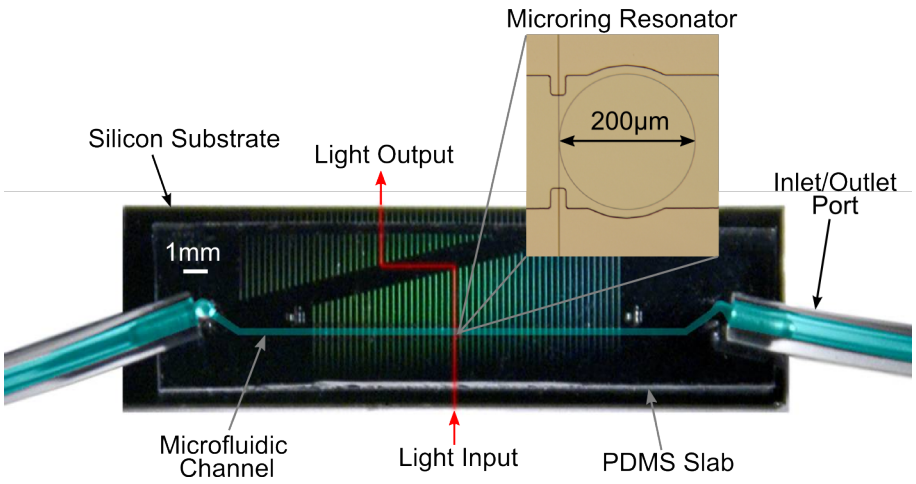

Figure 4.3: Photograph of the optofluidic device with an integrated PDMS microchannel spanning 50 waveguides with ring resonators. A waveguide is highlighted in red and the microfluidic channel is in blue. Inset shows a zoomed in microscope image of an exposed silicon microring resonator with an oxide clad waveguide.

4.4 Experimental methods

The experimental procedure for extracting the spectral information of the analyte consists of tuning the wavelength of the input light source while recording the transmission of the bus waveguide for various fluids present in the microfluidic channel. The setup, shown in Fig. 4.4, includes a tunable laser source (Tunics Reference SCL) which is coupled into our waveguides using a tapered lens fiber to increase coupling efficiency. Transmission through the device is collected with a microscope objective lens and focused onto a photodetector. Voltage outputs from both the power meter and laser source are sent to a DAQ card (National Instruments USB-6009) and recorded and synchronized by a computer running a LabView (National Instruments) script. The laser is tuned continuously at 1 nm/sec from 1460 nm to 1610 nm and the power meter

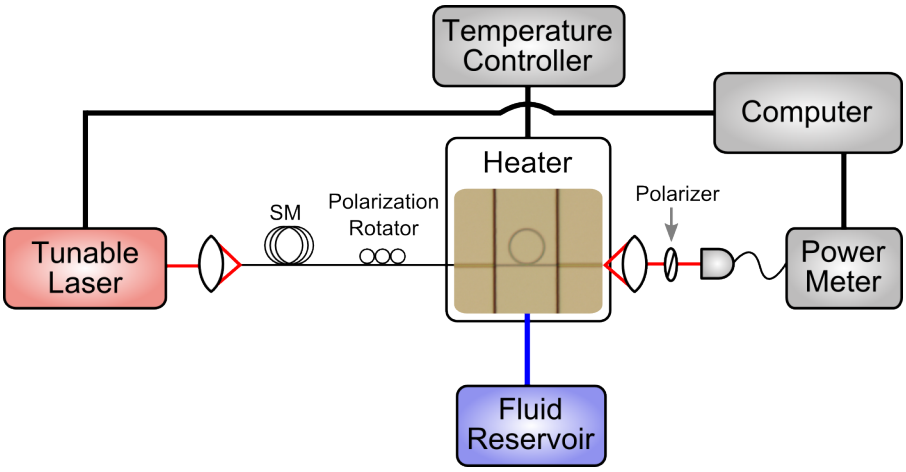

Figure 4.4: Schematic of the optical experimental setup used for microcavity-enhanced absorption spectroscopy measurements.

samples the detector at 500 Hz resulting in a spectral resolution of 2 pm. The acquisition time for this 150 nm window is 2.5 minutes; however, this can be greatly reduced by using a faster detector. With a 50 KHz detector and a maximum laser sweep speed of 100 nm/sec, the acquisition time would be reduced to 1.5 seconds while maintaining 2 pm resolution. The fluids of interest are controlled by pressure driven flow from a syringe pump (New Era Pump Systems, Inc NE-1000). The photonic chip is placed on a thermo-electric cooler to maintain temperature stability.

To determine the loss contribution of the analyte from the recorded transmission resonance curve, the following method is employed. Resonance in the ring corresponds to a dip in the transmission through the straight waveguide due to destructive interference between the transmitted light and ring light coupling back into the straight waveguide. As we derived in Chapter 2, the transmission at resonance is given by [67]:

$$T(\theta) = \frac{a^2 + t^2 - 2at\cos\theta}{1 + a^2t^2 - 2at\cos\theta} \tag{4.9}$$

where a is the field attenuation coefficient, t is the field transmission coefficient at the waveguide/ring coupling region, and θ is the phase shift per circulation. The phase shift can be expressed in terms of the free space wavelength as $\theta = {}^{2\pi L n_{eff}}/_{\lambda}$ where L is the ring circumference and n_{eff} is the effective index of the mode [101]. It is beneficial to restate Eq. 4.9 in terms of experimentally measurable quantities so that the only fitting parameters are the attenuation and transmission coefficients. This can be done by expanding the cosine term in Eq. 4.9 for small wavelength deviations around a resonant wavelength λ_o:

$$\cos(\theta) = \cos(2\pi L n_{eff}/\lambda) \cong 1 - \frac{2\pi^2 L^2 n_g^2}{\lambda_o^4}(\lambda - \lambda_o)^2 \tag{4.10}$$

where L is the ring circumference and the group index n_g can be calculated directly from the resonance spacing using the relation $FSR = {}^{\lambda^2}/_{n_g L}$ [70].

Fitting the theoretical curve described by Eq. 4.9 to a resonance yields values for the attenuation and transmission coefficients. However, since these coefficients are interchangeable they need to be distinguished. This can be done by comparing the coefficient values for two rings of equal radius but with different size gaps between the ring and bus waveguide. The field transmission coefficients which describe coupling will shift to lower values (greater coupling) for smaller gap distances while the attenuation coefficients remain the same. The total absorption coefficient α_T for propagation within the ring is then determined from the relation $a = e^{\alpha_T L/2}$. The total absorption is related to the absorption of the fluid by

$$\alpha_T = \alpha_I + \Gamma\alpha_A \tag{4.11}$$

where α_I is the intrinsic waveguide loss, α_A is the absorption from the analyte, and Γ is the confinement factor which is a measure of how much of the total guided light is interacting with the cladding material. The confinement factor can be determined from a simulation of a waveguide's mode profile using [102]:

$$\Gamma = \frac{n_A \int_A |E|^2 dA}{Z_o \int_\infty \mathrm{Re}\{\ E \times H^*\} \cdot \hat{z}\, dA} \tag{4.12}$$

where the top integral is over the analyte cladded region, n_A is the refractive index of the analyte and Z_o is the free space impedance.

4.5 Results and discussion

In order to measure the absorption spectrum of an analyte, we first perform measurements with no fluid in the channel (air exposed devices) to determine the intrinsic waveguide loss, α_I . We chose to make this measurement with no fluid in the channel both for simplicity and because the change in coupling due to the addition of a fluid will not significantly alter the intrinsic waveguide loss. We measure the transmission through the device and analyze each resonance to determine the waveguide loss over the spectral range of our tunable source. An example of the curve fitting can be seen in Fig. 4.5 which shows a loaded Q value of ~120,000. Using the methods described above, the resonance is known to be slightly under-coupled and the resulting fitting parameters are $t = 0.981$ and $a = 0.967$ for the field transmission and attenuation coefficients respectively.

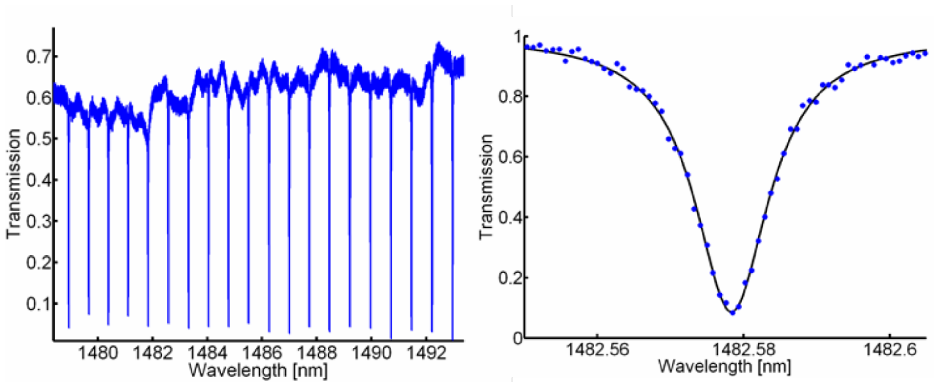

Figure 4.5: (a). Ring resonator transmission showing a 15 nm window of the complete transmission spectrum (1460 nm - 1610 nm). (b) A close up of a representative resonance dip (points) and the resulting curve fitting (solid line). The waveguide loss at the resonance wavelength is 4.67 dB/cm and the resonance has a quality factor of 120,000.

The attenuation value for this resonance corresponds to an intrinsic waveguide absorption of $\alpha_I = 1.07\, cm^{-1} = 4.67\, {}^{dB}/_{cm}$ for waveguide propagation.

We demonstrate the ability to detect absorption features in an analyte by injecting undiluted N-methylaniline into the microfluidic channels. This analyte was chosen since the N-H bonds in N-methylaniline lead to an absorption peak near 1500 nm [89] which is within the limits of our tunable laser. The FSR between resonances is ~1 nm and each resonance is fitted to determine the attenuation and transmission coefficient, shown in the inset of Fig. 4.6. Once the total absorption is known, we determine the contribution from the fluid using Eq. 4.11 and subtracting the intrinsic absorption measured while the device is air clad. The confinement factor for our waveguide dimensions was calculated from Eq. 4.12 using a refractive index of 1.56 for N-methylaniline. The absorption spectrum of N-methylaniline measured using the ring resonator device is plotted in Fig. 4.6 along with the absorption measured using a commercial

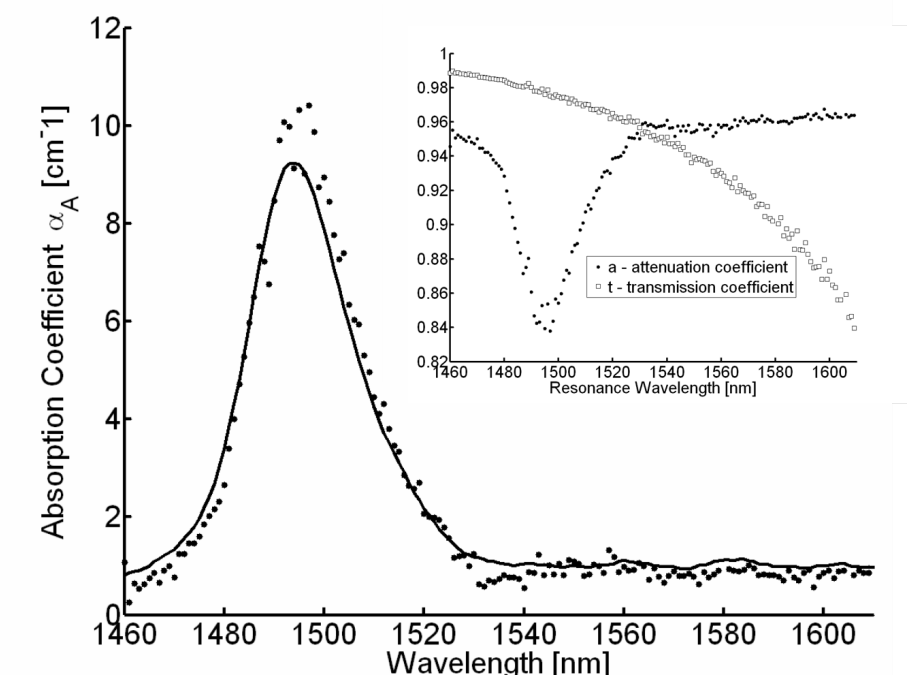

Figure 4.6: Absorption spectrum for N-methylaniline measured using a microring resonator (points) and with a commercial spectrophotometer (solid line). The inset shows the attenuation and transmission coefficients for each resonant wavelength.

spectrophotometer (Shimadzu UV-3101PC UV/Vis/Near-IR Spectrophotometer) and there is very good agreement between the two curves. The results plotted in Fig. 4.1 are the average of 8 consecutive measurements for a single microring resonator with an average standard deviation of $0.25\,\mathrm{cm}^{-1}$. The additional noise present at the absorption peak is likely due to the decrease in the extinction ratio of the resonances at these wavelengths which lowers the signal to noise ratio of the measurement.

The sensitivity of the device is related to the effective path length traveled by light circulating within the ring. The free space equivalent path length can be determined from the quality factor Q of the ring resonance as $L_{eff} = \Gamma\frac{Q\lambda_o}{2\pi n_{eff}}$. For the resonance measured in our device with a Q~120,000, effective index of $n_{eff} =$

2.5, and confinement factor of $\Gamma = 0.43$, the calculated effective path length is ~5 mm. A straight waveguide without a ring would have to be ~20 times longer to achieve the same sensitivities in measurement. The long equivalent free space path length shows that microring resonators can be efficiently used to increase the sensitivity of a miniaturized on-chip device.

The resolution of measurements with our device is determined by the FSR between resonance wavelengths. The FSR is dependent on the ring circumference which can be lengthened if higher resolution is required or shortened to make the device more compact. With a 1 nm FSR, the resolution of our device is higher than that of the spectrophotometer used as a comparison in Fig. 4.6 which had a minimum slit width of 2 nm. The resolution of a straight waveguide would be only limited by the linewidth of the laser but this increased resolution comes with the cost of reduced sensitivity as mentioned earlier. Another important quantity for determining the quality of a spectroscopy measurement is the signal to noise ratio (SNR). The light source, detector and coupling into the photonic chip contribute to the noise of a measurement. The first two sources are present for any spectrometer measurement while the third contribution is unique to integrated photonic devices. Coupling noise is due to both mechanical vibrations as well as reflections from the end facets which lead to Fabry-Perot noise at the output. The SNR of a signal from our laser source to the detector is ~50 dB. With coupling into a photonic chip, the SNR is reduced to ~43 dB. This additional source of noise for photonic devices due to coupling could be eliminated by using an integrated light source and detector which would allow the SNR of the measurement to approach that of commercial spectrophotometers.

4.6 Summary

In this work I have demonstrated cavity-enhanced absorption of an analyte with an integrated on-chip device. A 100 μm radius microring resonator with Q values > 100,000 was used to measure the absorption spectra of N-methylaniline from 1460 to 1610 nm with a resolution of 1 nm. The wavelength range of the device was limited by laser tunability and in principle measurements could be extended from 1.2 to 6 μm using silicon waveguides with an appropriate buried oxide thickness. We have shown good agreement between measurements with a commercial spectrophotometer and the extracted absorption using our device with less than 2 nL of fluid and a device footprint of less than 0.03 mm^2. While the infrared wavelength range is useful for spectroscopy applications for chemical analysis, it would also be beneficial to extend this technique into the UV/Vis spectrum for biological analyte measurements. Similar measurement could be performed with waveguides and resonators made using silicon nitride (Si_3N_4) which is transparent in the visible spectrum. This technique can help realize a completely on-chip spectroscopy device for label-free massively parallel detection of analytes for lab-on-a-chip applications.

CHAPTER 5

INTEGRATED SPECTROPHOTOMETRY FOR BIOANALYSIS USING MICRORING RESONATORS

In this chapter I demonstrate optical absorption measurements on minute volumes of fluid in the visible regime using a similar ring resonator based optofluidic device which was presented in Chapter 4. This application, however, takes advantage of the ring resonator's nanoscale sensing volume to perform sensitive absorption-based measurements. I measure the colored products of an enzyme-catalyzed reaction commonly used in bioassays and investigate the limit of the device's sensitivity[1].

5.1 Introduction to visible absorption-based bioanalysis

The ability to perform spectroscopic measurements on-chip by combining microfluidic and nanophotonic capabilities would enable miniaturized, low-cost, fully automated, and massively parallel devices for lab-on-a-chip applications [18, 87, 104, 17, 93]. Many biomedical techniques would benefit from an on-chip spectrophotometry tool such as the quantification of DNA/RNA/protein samples [105, 106] and the analysis of colorimetric assays [107]. Also, current methods of bacteria detection include growing bacteria on selective and identifying media such as chromogenic agars [108]. These media change color as enzymes produced by the bacteria convert substrate molecules in the nutrient agar into a colored visible product. However, this method requires an incubation period of many hours to several days [109] in order for the color change to be strong enough for it to be identifiable by the naked eye or a microscope.

[1]Portions of this chapter are reproduced with permission from [103]

We demonstrate here a platform that can, in principle, detect minuscule color changes produced by individual enzymes in a manner of minutes and therefore can be used in rapid chromogenic-based bacteria detection.

The platform is based on microring resonators for ultrasensitive absorption measurements in the visible regime [110]. These microcavities have been shown to be effective sensors for performing absorption spectroscopy on nanoliter volumes of fluids in the infrared regime [96, 111, 19] for chemical analysis. Here I show on-chip spectroscopic measurements of enzyme-produced absorption at visible wavelengths where nearly all biologically relevant chromophores and fluorophores have spectral features [112]. The microring resonators detect the color change that is produced by the conversion of a substrate molecule into a colored product by an enzyme commonly used in enzyme-linked immunosorbent assays (ELISA). ELISA is a powerful biochemical technique used to detect the presence of antibodies and antigens (such as proteins, clinical markers, pathogens, toxins, etc) in a sample [113]. The substrate molecule used often for these experiments is tetramethyl benzidine (TMB) which turns blue by the action of the enzyme horseradish peroxidase (HRP) [114]. In one example of an ELISA, HRP is conjugated to an antibody which is used to determine the presence of a target antigen. After binding to the antigen and the addition of the TMB substrate, the chromogenic reaction products can then be quantified at 650 nm which is the designed wavelength of operation for our device.

The principle of operation relies on the cavity enhancement of a microring in order to detect changes in its local environment [97], as shown in Fig. 5.1(a). Light is coupled into the bus waveguide and a small fraction of light evanescently couples to the microring cavity. Light with a wavelength which fits an

integral number of times within the ring circumference builds up due to constructive interference. In this way light can circulate around the ring many times resulting in an effective path length that is orders of magnitude greater than the ring circumference. Due to this cavity enhancement, the ring is very sensitive to any changes in or around the waveguide since the effect of any perturbation is multiplied by the number of round trips that light undertakes. Since the evanescent field of the waveguide mode extends into the analyte (see Fig. 5.1(b)), any optical absorption present in the analyte will alter the transmission characteristics of the device. Note that this technique is fundamentally different from refractive index based sensors which measure a shift in the resonance position due to a binding event [115, 116, 66]. Refractive index sensors can be compromised by binding of non-target molecules as well as thermal fluctuations which can also shift the resonant wavelength. In contrast, by using absorption as the measurement metric, the sensor presented here provides reaction specific spectral information which does not suffer from the above drawbacks.

5.2 Materials and methods

As derived in Chapter 2, and demonstrated in Chapter 4, the parameters of a ring resonator can be determined by curve fitting to the transmission spectrum of the device. The goal of this curve fitting is to find a, the field attenuation coefficient which quantifies the sidewall scattering, bending loss, and most importantly the absorption induced by the enzymatic reaction. The field attenuation coefficient is related to the more familiar power attenuation coefficient, α, by the relation $\alpha = -2ln\frac{a}{L}$. The field transmission coefficient, t, accounts for coupling losses between the ring and waveguide, and θ is the phase shift per

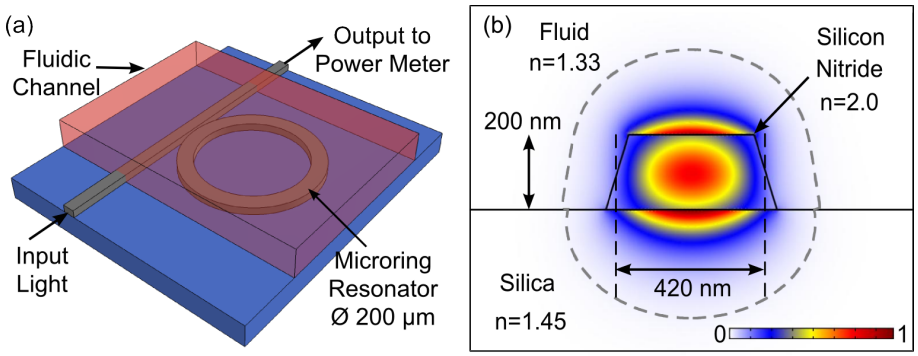

Figure 5.1: (a) Device design for a microring resonator covered by a microfluidic channel. The microring enhances the interaction length between the cladding fluid and the evanescent field of the guided mode. (b). E^2 profile of the TM mode in a silicon nitride waveguide at a wavelength of 650 nm and covered with an aqueous solution. The dashed line is the contour at which the field decays to 1% its maximum value.

round trip. The phase shift can be expressed in terms of the light frequency, ω, circumference of the ring, L, and the effective index n_{eff} as $\theta = {}^{\omega L n_{eff}}/_{c}$. Since the evanescent field of the mode in the ring extends into the analyte material, any optical absorption in the material will increase the round trip propagation losses and decrease the value of the measured attenuation coefficient. The absorption in the analyte can be related to the absorption in the ring by numerically calculating the mode overlap of the field with the analyte. For our case this mode overlap, also called the confinement factor, is $\Gamma = 0.22$. Fig. 5.2 shows how the resonance curve changes as the absorption in the cladding material increases. The resonance linewidth broadens and the extinction ratio decreases as losses increase. Also shown in Fig. 5.2 are the curves fit to each transmission spectrum, from which we extract the ring's attenuation coefficient and determine the loss contribution due to the analyte.

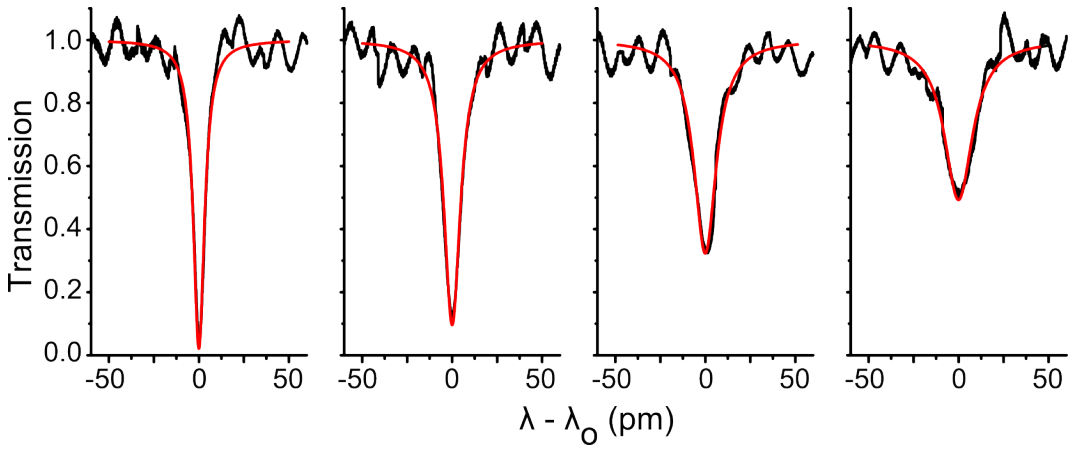

Figure 5.2: Experimentally measured transmission spectrum of a microring resonator (black line) with fluid analytes of increasing absorbance (left to right) showing the change in extinction ratio and linewidth as the resonator loss increases. The data was fit (red line) to extract the absorption coefficient of the cladding fluids.

5.3 Fabrication of microrings for bioanalysis in the visible spectrum

The nanophotonic devices are fabricated using standard microlithography techniques and a more detailed list of steps can be found in Appendix A. Four microns of thermal oxide was first grown on top of a silicon wafer. Stoichiometric silicon nitride was then deposited, 200 nm thick, using low pressure chemical vapor deposition (LPCVD). An electron beam resist (MaN 2403) was spun on top of the wafer followed by a conductive layer (ESPACER). The ring resonators and bus waveguides were patterned using a JEOL 9300 E-beam system. After the wafer was developed to remove unexposed resist, the wafer underwent a post exposure bake for 5 minutes at 145 °C to reflow the resist surface to minimize roughness. The devices were then etched using inductively coupled

reactive ion etching (ICP RIE) with a CHF_3/O_2 process chemistry . The devices were then annealed at 1200 °C for 20 minutes at atmospheric pressure. The devices were cut from the wafer with a dicing saw and the end facets polished to improve optical coupling into the waveguides. A lift off process is used to mask a 250 μm channel perpendicular to the waveguide while the rest of the waveguide is clad with 3.5 μm of evaporated silicon oxide. Further details on the waveguide fabrication can be found at [79] where a similar process was used with demonstrated waveguide propagation losses of 0.1 dB/cm in the near infrared.

Microfluidic capabilities are integrated with the photonics using polydimethylsiloxane (PDMS) soft lithography processes [117]. A 30 μm tall by 300 μm wide channel mold is patterned with SU8 channels on a silicon wafer. PDMS is poured over the channel mold, allowed to cure, and then inlet holes are punched to access the channels. The microfluidic slab is then aligned on top of the unclad portion of the waveguides using a contact aligner. The device performance is measured with various fluids which are prepared by controlling the enzyme concentration. First, 5 mg of horseradish peroxidase powder (Thermo Scientific) was dissolved into 5 mL of deionized water. This solution was twice diluted by 100 times to generate a solution with concentration of 100 ng/mL. Separately in a 96-well plate, 100 μL of the substrate TMB (KPL SureBlue Reserve) was added to 6 wells. Different amounts of the HRP enzyme solution was then added to the 6 substrate-containing wells to produce a final enzyme concentration in the wells of 6, 4, 2, 1, 0.5, and 0 ng/mL. Upon addition of the enzyme solution, the color of the fluid in the wells began to produce a blue tint due to the HRP catalyzed conversion of the TMB substrate into a colored product. The color was allowed to develop for 5 minutes and then a stopping solu-

tion (KPL TMB BlueSTOP) was added. The stopping solution prevents further enzyme reactivity and the absorbance values of the fluid in the wells maintain a constant level which allows reliable measurements to be performed on the samples over an extended time period. The absorbance values of the well-mixed fluids were measured with a commercial spectrophotometer (Spectramax Plus 384) and the absorption spectrum is shown in Fig. 5.4(a). The fluids are then individually measured by our optofluidic device.

5.4 Results and discussion

The performance of the device is characterized by measuring the ring resonator response to fluids with a range of absorbance values, as shown in Fig. 5.2. For each fluid with different enzyme concentration, the ring transmission is experimentally measured using a tunable laser which sweeps the frequency of light through a resonance and records the transmitted optical power. The experimental setup is shown in Fig. 5.3.

The light source is a 1 mW fiber coupled external cavity diode laser (Sacher Lasertechnik TEC 530) with wavelength range of 640 nm to 653 nm. Note that for future applications the transmission spectrum can be measured in principle using a single light source and a heater to temperature tune the resonances [118]. Light is coupled into the waveguides using a polarization maintaining optical fiber that is positioned into physical contact with the polished waveguide end facet. The waveguide output is collected with a high numerical aperture microscope objective and sent through a polarizer to ensure measurement of the proper polarization. The polarized light is split to both a wavemeter

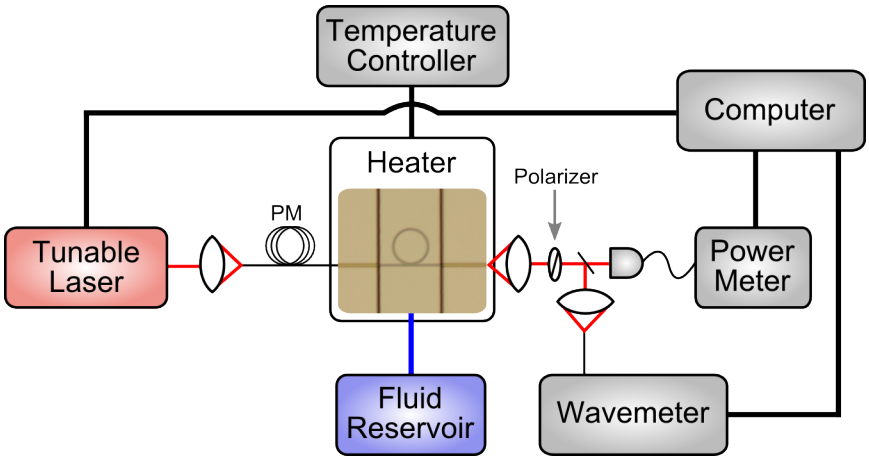

Figure 5.3: Schematic of the optical experimental setup used for absorption measurements of ELISA enzyme reaction products.

(Advantest) and power meter to simultaneously record power and frequency. The intrinsic ring performance is determined by measuring a ring resonance without any additional absorption caused by the addition of HRP enzymes. The extracted field attenuation coefficient is $0.965 \pm .004$ which corresponds to an intrinsic quality factor of ~180,000 and a waveguide propagation loss of 4.9 dB/cm.

We show a linear relationship between the absorbance of the analyte fluid (as measured from a commercial spectrophotometer) and the total waveguide propagation loss in the ring (see Fig. 5.4(b)), indicating the ability of the device to accurately determine the absorbance of an analyte within the range commonly measured (0-4 AU) with spectrophotometers. The absorbance values for the fluid are normalized by the spectrophotometer to a path length of 1 cm. The limit of detection is determined by making multiple measurements and the resulting standard deviation is considered the noise floor of our experiment. After 10 consecutive scans on the same resonance, the deviation in the extracted field

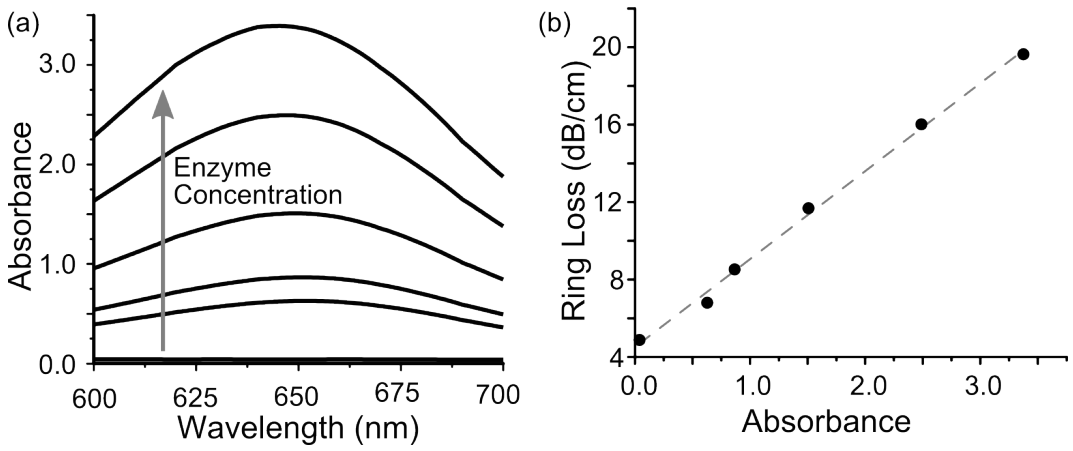

Figure 5.4: (a) The absorbance measured with a commercial spectrophotometer of each of the enzyme concentrations tested with the microring resonator. (b) The resulting ring propagation losses as a function of the absorbance of the fluid covering the resonator at λ=650 nm.

attenuation coefficient is σ = 0.0038 which is less than 0.4 % its nominal value of a=0.965. This deviation in the ring performance metric corresponds to a detection limit of 0.1 cm^{-1} in the fluid absorption coefficient. The noise floor is currently limited by the laser intensity fluctuations due to mode-hopping during wavelength tuning which could be reduced by either using a different light source or using temperature tuning for spectral measurements.

Based on the data presented, we calculate a best-case sensitivity capable of measuring the products of individual enzyme molecules after only a few minutes of activity. The sensitivity of the device can be determined by considering the concentration of enzymes within the sensing volume of the ring resonator. The microfluidic channel covering the ring resonators transports fluid to the device and has cross sectional dimensions of 300 µm by 30 µm. The volume to cover the ring resonator is on the order of a few nanoliters, and therefore contains thousands of enzymes. However, the effective sensing volume of the

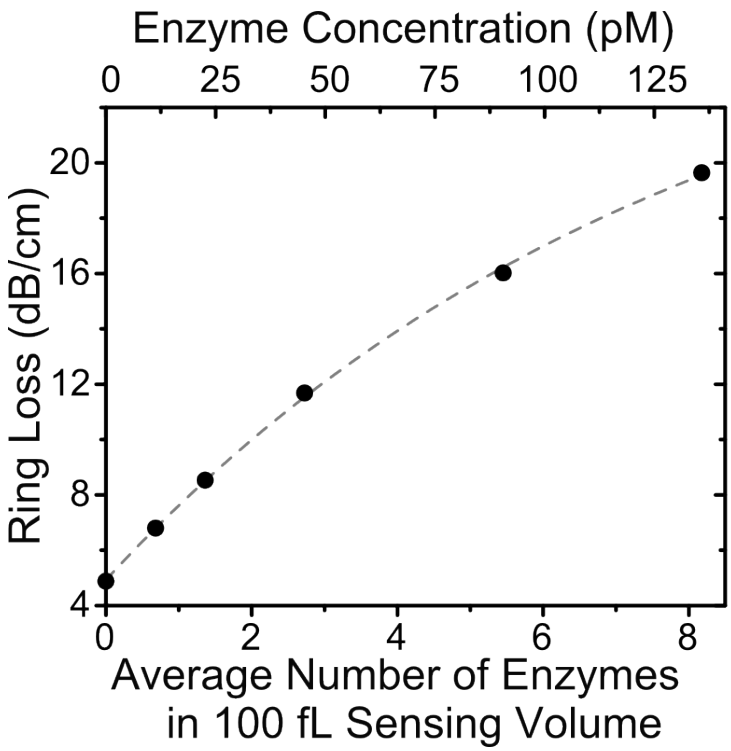

Figure 5.5: Ring propagation loss as a function of both enzyme concentration and the number of enzymes within the sensing volume of the microring resonator (~100 fL).

device is much smaller since the squared electric field magnitude, $|E|^2$, decays to 1% of its value within ~200 nm (as shown by the gray contour line in Fig. 5.1(b)). Changes of absorption in the analyte beyond this contour have minimal effect on the device performance due to a lack of overlap with the field. Multiplying the sensing area within the fluid by the ring circumference we find the effective fluidic sensing volume of the device to be ~100 fL. Since we know the concentration of enzymes used for each fluid preparation, we can determine the average number of enzymes within this sensing volume of the ring resonator. Note that the resonator does not actually detect enzymes, but rather the multitude of absorbing reaction products catalyzed by the enzyme. In Fig. 5.5 we show the average number of enzymes within the 100 fL effective sensing volume of the

ring resonator in a well-mixed sample, or equivalently, the number of enzymes it takes to generate the optical absorption present around the ring resonator. For the various fluid preparations used in the experiment, we show that in principle the device can be used to measure the activity of single enzyme molecules. In order for this sensitivity to be fully realized, the sample volume would need to be reduced to the order of tens of femtoliters which is already within current capabilities of nano reaction chambers [119]. This sensitivity will become important for localized detection of enzyme reactions in microarray applications, in bacterial metabolism identification and in multiplexed highly parallel nano-ELISA systems.

5.5 Summary

We have demonstrated the ability to detect chromogenic changes in nanoliter volumes of fluid in an optofluidic device at visible wavelengths. The change in the transmission spectrum of a 100 μm radius ring resonator was used to quantify the optical absorbance of fluids covering the microring with a limit of detection of $0.1\,\mathrm{cm}^{-1}$. The device was used to measure fluid absorbance over the optical density range covered by typical spectrophotometers and is sensitive to the activity of individual enzymes for a 100 fL sample volume. The high sensitivity, low analyte consumption, and miniaturization enable the device to be used for on-chip antibody or antigen detection with ELISA as well as other chromogenic based techniques such as bacteria detection.

CHAPTER 6

OPTICAL ABSORPTION-BASED MICRORING RESONATOR BACTERIA SENSOR

Next we apply the microring resonator absorption-sensor platform for the detection of live bacteria. We propose a bacteria sensor which would enable the detection of a live bacterium in much shorter time period than current day-long incubation based test. Towards this goal, I demonstrate an optofluidic device which uses enzyme catalysis to identify the presence of bacteria and can therefore be used to quantify the number of viable bacteria in a fluid sample[1].

6.1 Introduction

A number of different technologies exist for the detection and identification of pathogenic bacteria in diagnostic laboratories. Traditional techniques include biochemical and microbiological assays [120] where bacteria are incubated for days and identified based on their phenotype. Powerful new techniques have been developed, such as polymerase chain reaction (PCR) [121] and immunoassays [113], which can be very sensitive and provide rapid results. However, these tests are expensive, labor intensive, and consume the sample being analyzed. Furthermore, these tests do not determine the viability of the pathogen nor can they test for antibiotic resistance. Therefore, there is a great need to develop a rapid, sensitive, and low cost detection technique that can test viability and enable follow-up analysis.

We propose a device which has the potential to detect single bacteria without

[1]Portions of this chapter are reproduced with permission from [4]

consuming expensive reagents or requiring high cost equipment. The high sensitivity means that day-long incubation periods to grow colonies is unnecessary and therefore the measurements can be done rapidly. By combining nanophotonics with microbiological testing, the device can take advantage of the benefits of a microfabricated platform which include massive parallelization of measurements and low cost [122].

The proposed device would use chromogenic agars which change color due to enzymatic activity to detect bacteria [123]. Typical use of these agars includes incubation for many hours/days, after which identification of colonies is done by observing the change in color of the agar by eye [108]. Instead of simply placing these agars on a plate, we propose depositing a very thin layer of hydrogel on top of a microring resonator. These types of thin agar layers have been demonstrated previously [124]. The microring cavity allows for very sensitive optical absorbance measurements on surrounding materials as demonstrated in Chapters 4 and 5. The hydrogel would then serve as a growth media for the bacteria to live on and the subsequent color change induced in the agar could be measured directly by the microring resonator.

The chromogenic assay relies on the cleavage of the tetrazolium salt XTT 2,3-bis(2-methoxy-4-nitro-5-sulfophenyl)-5-[(phenylamino) carbonyl]-2H-tetrazolium hydroxide to generate a water soluble orange formazan product [125]. The conversion is due to metabolic activity in viable cells, including mitochondrial dehydrogenase. The amount of the formazan dye, which is measured using optical absorbance, is correlated with the number of viable cells [4]. Therefore XTT has been widely employed in a variety of assays to evaluate cell viability including studies in bacteria [126], fungi [127], human cell growth [128]

as well as drug susceptibility studies [129]. The model bacterium tested in this investigation is *Escherichia coli* strain K-12.

In order to test the feasibility of the proposed bacteria/hydrogel/microring device, we perform measurements in solution and flow the absorbing liquid over top of the microring resonators. This will allow us to determine the sensitivity of the microring resonators to metabolic activity of bacteria.

6.2 Arrayed microring device design

I have previously shown that microring cavities can be used very effectively as optical absorbance sensors for fluids using a microfluidic platform, as shown in Fig. 6.1a. As described in Chapter 4, the enhancement of light by the microring resonator allows for sensitive measurements of the optical absorbance of fluids which are flowed on top of the ring resonator. The proposed device will utilize the bacterial enzyme catalyzed reaction of XTT into a colored product. The absorption spectrum of this dye can be seen in Fig. 6.8 and has a peak around 470 nm. Since there are no commercially available tunable wavelength lasers that operate at this wavelength I will describe below a novel measurement method which allows us to use a fixed wavelength source to measure the resonance response of a microring.

The measurement technique relies on the thermo-optic effect where the refractive index of materials changes with temperature [130]. As the indices of the waveguide and surrounding materials change, the resonance wavelength with shift to longer wavelength for a positive thermo-optic coefficient. To illustrate how this can be helpful, consider a laser that is slightly red shifted in

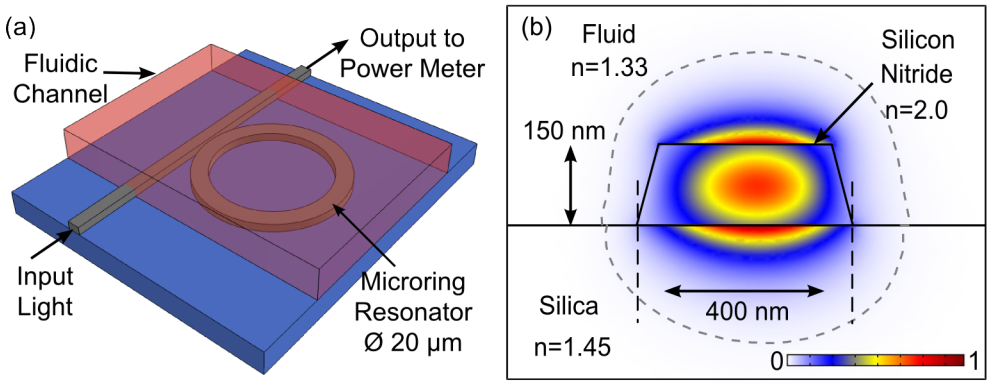

Figure 6.1: (a) Schematic layout of the optofluidic device which includes a microring resonator inside a microfluidic channel. (b) $|E^2|$ profile of the TM mode in a silicon nitride waveguide at a wavelength of 496 nm and covered with an aqueous solution. The dashed line is the contour at which the field decays to 1% its maximum value.

wavelength with respect to the resonance wavelength. This single wavelength is input into the device and then the ring is heated. If the device is heated so that the resonance wavelength is shifted over and past the wavelength of the laser, the transmitted power at the single frequency will also go through a dip in power as the resonance is swept across it (shown graphically in Fig. 6.2). This method allows the integration of an inexpensive laser to the device and permits measurement at other wavelengths which are not available with current commercial tunable laser sources. The only limitation on the laser is that its linewidth be as narrow as the resonance feature being measured.

The microring is designed to operate at 496 nm which is one of the emission lines of an Argon ion laser. While not at the peak of the absorption of XTT (see Fig. 6.3), the absorbance does reach 80% of its maximum value. The material platform is the same as in Chapter 5, which is silicon nitride (Si_3N_4) as the waveguiding material on top of silicon dioxide (SiO_2). The schematic layout of

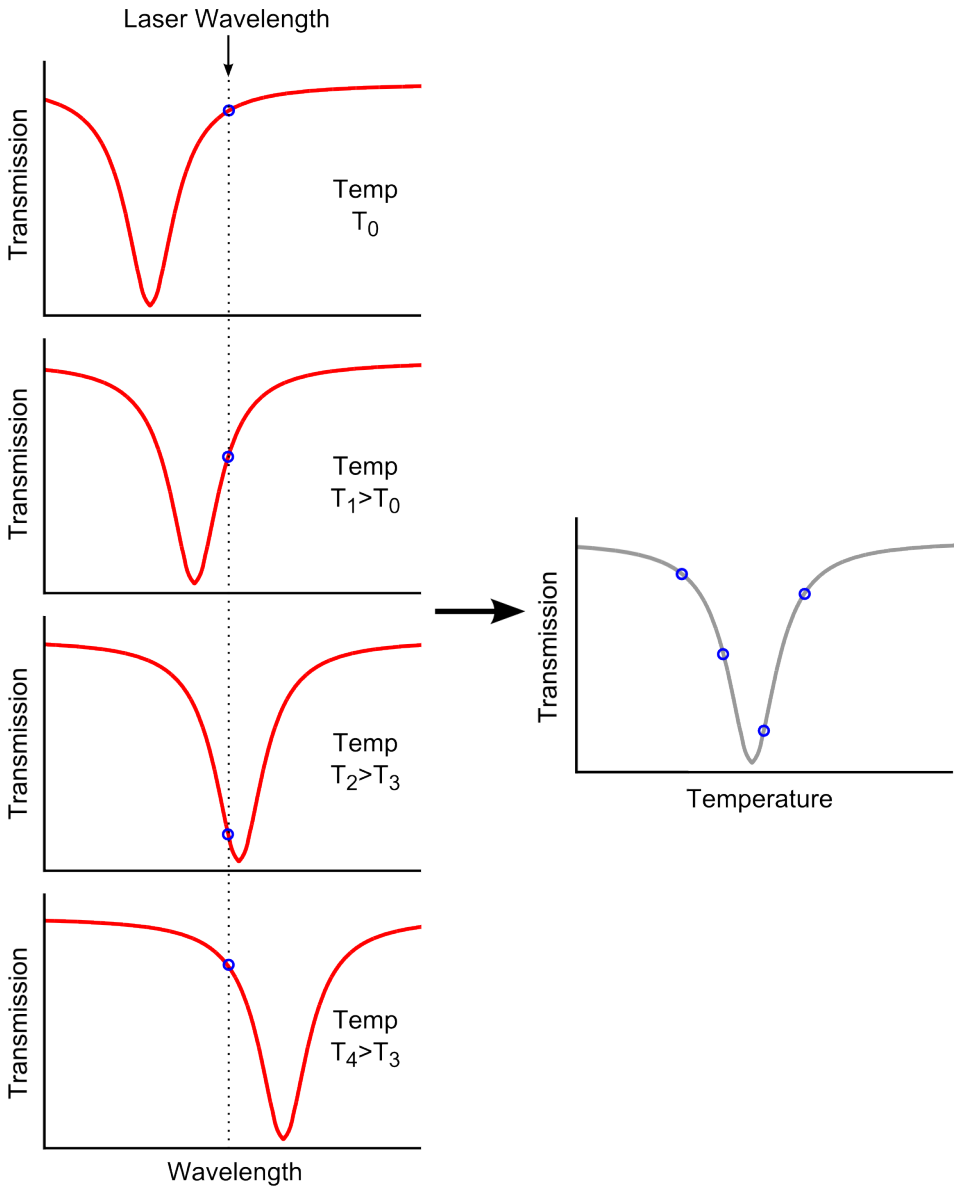

Figure 6.2: On left, resonance feature shifts towards longer wavelength as temperature increases. On right, the transmission as a function of temperature at the single wavelength represented by the dotted line.

the device and the mode profile of the tranverse magnetic (TM) mode is shown in Fig. 6.1. The dimensions of the waveguide are chosen to ensure single mode operation at the wavelength of operation. We demonstrated in Chapter 5 that

due to the very small effective sensing volume around a microring resonator, the device can be sensitive to the activity of individual enzymes. In order to decrease the sensing volume further, we reduce the bending radius of the microring to 10 μm. The free spectral range of this sized resonator is expected to be several nanometers. Since we expect only small shifts of wavelength by using the thermo-optic effect, on the order of 0.1 nm, we fabricate arrays of microrings each with slightly wider radii. This ensures that a resonance will be within tuning range of the device.

6.3 Temperature-tuned microring theory

In Chapters 4 and 5, the microring resonator based optical absorption measurement were performed by scanning a tunable wavelength laser and measuring the output power from the device. These large tunable sources are expensive and are only available at particular wavelengths. Therefore, it would be beneficial in terms of portability, miniaturization, and cost to develop a technique to measure microcavity resonances without relying on tunable optical sources. In fact, laser diodes are readily available at a large number of different wavelength throughout the visible regime. Here I demonstrate for the first time the use of a single wavelength source to measure the transfer function of the microring device. As described in Chapter 2, the transmitted power can be characterized by the following relation:

$$P(\theta) = \frac{a^2 + t^2 - 2at\cos\theta}{1 + a^2t^2 - 2at\cos\theta} \tag{6.1}$$

where a field attenuation coefficient , t is the field transmission coefficient,

and θ is the phase shift of light upon circulation around the ring. The phase shift can be rewritten as

$$\theta = \frac{2\pi L n_{eff}}{\lambda} \tag{6.2}$$

where L is the ring circumference and n_{eff} is the effective index of the guided mode. A tunable source varies the phase shift by continuously tuning the wavelength λ, of the light. However, the phase shift can be similarly varied by controlling any of the other variables that affect the phase, namely the cavity length L and the effective index n_{eff} of the guided mode. By using the thermo-optic effect, where the refractive index of a material changes with temperature, we can alter the effective index of the mode by heating our microcavity. Therefore, even for a constant wavelength λ, the phase shift θ can be varied and the transmission spectrum can be measured by controlling the temperature of the microring.

Heating an optical cavity leads to a change in the optical path length due to two factors: the thermo-optic effect and thermal expansion. The change in the optical path, S, can be described by [131]:

$$\frac{dS}{dt} = \alpha n + \frac{dn}{dT} \tag{6.3}$$

where the α is the thermal expansion coefficient, n is the refractive index and $^{dn}/_{dt}$ is the thermo-optic coefficient of the cavity material. This equation can be generalized to the case of optical microcavities formed with waveguides by replacing the refractive index with the effective index, n_{eff}. In Table 6.1 we show the relevant material physical quantities which determine the microring resonators optical path change due to temperature changes at the wavelengths

$\lambda_1 = 1.5\ \mu m$ and $\lambda_1 = 0.5\ \mu m$.

Table 6.1: Temperature Dependent Material Properties

Material	$\frac{dn}{dT}$ $(10^{-5}\ K^{-1})$	α_T $(10^{-5}\ K^{-1})$	ref.
Silicon Nitride	4.0_{λ_1}	0.16	[132],[133]
Glass	1.0_{λ_2}	0.055	[134],[134]
Silicon	18.3_{λ_1}	0.36	[135],[136]
Water	-14.9_{λ_2}	$\beta = 25.6$	[137],[134]

As shown in Table 6.1, the linear thermal expansion coefficients α_T, are on average an order of magnitude less then the thermo-optic coefficients $^{dn}/_{dt}$. Therefore, we expect that the mechanical elongation of the cavity does not play a significant role in changing the optical path length and we will assume that the optical path length change is dominated by the change in refractive index of the materials. The resonance wavelength shift $\Delta\lambda$ due to a change in the effective refractive index Δn_{eff} can be derived from the resonance condition to be:

$$\frac{\Delta\lambda}{\lambda} = \frac{\Delta n_{eff}}{n_g} \tag{6.4}$$

where n_g is the group index. The change in the effective index n_{eff} is due to all the changes in the refractive indices of the various materials that make up the waveguide system. As shown in Fig. 6.1, the evanescent field of the mode exists not just in the waveguide material, but extends into the lower oxide cladding as well as the upper aqueous cladding. Changes in the material indices must therefore be properly weighted by the confinement factor Γ of light within each region to determine the total change in the effective index [102].

$$\Delta n_{eff} = \Gamma_{Si_3N_4}\,\Delta n_{Si_3N_4} + \Gamma_{SiO2}\,\Delta n_{SiO_2} + \Gamma_{clad}\,\Delta n_{clad} \tag{6.5}$$

where n_{clad} is the index of the material that is cladding the ring which in our case will be either air or an aqueous solution. The confinement factor Γ_{mat} was introduced in Chapter 3 and is equal to

$$\Gamma_a = \frac{n_a \int_a |E|^2 dA}{Z_o \int_\infty \mathrm{Re}\{\ E \times H^*\} \cdot \hat{z}\, dA} \tag{6.6}$$

and quantifies the overlap of the optical mode in a region a with refractive index n_a. For changes in the material indices due to small temperature changes dT, Eq. 6.5 can be expressed by the differential:

$$\frac{dn_{eff}}{dT} = \Gamma_{Si_3N_4}\,\frac{n_{Si_3N_4}}{dT} + \Gamma_{SiO_2}\,\frac{n_{SiO_2}}{dT} + \Gamma_{clad}\,\frac{n_{clad}}{dT} \tag{6.7}$$

The above equation allows us to determine the change in the resonance wavelength due to a changes in the material indices with temperature by plugging in dn_{eff}/dT into the following equation:

$$\frac{d\lambda}{dT} = \frac{\lambda}{n_g}\,\frac{dn_{eff}}{dT} \tag{6.8}$$

This allows us to determine the wavelength shift with temperature, $\frac{d\lambda}{dT}$, with knowledge of the group index n_g and the effective index change with temperature, $\frac{dn_{eff}}{dT}$.

6.4 Fabrication of optofluidic device for bacteria detection

The nanophotonic devices are fabricated using standard microlithography techniques in similar fashion to the description found in Chapter 5, and covered in detail in Appendix A, with a few modifications. Four microns of thermal oxide was first grown on top of a silicon wafer to provide a lower buried oxide layer to isolate the waveguide from the silicon substrate. Stoichiometric silicon nitride was then deposited to a thickness of 150 nm using low pressure chemical vapor deposition (LPCVD). An electron beam resist (MaN 2403) was spun on top of the wafer followed by a conductive layer (ESPACER). The ring resonators and bus waveguides were patterned using a JEOL 9300 E-beam system. After the wafer was developed to remove unexposed resist, the wafer underwent a post exposure bake for 5 minutes at 145 °C to reflow the resist surface to minimize roughness. The devices were then etched using inductively coupled reactive ion etching (ICP RIE) with a CHF_3/O_2 process chemistry. The devices were then annealed at 1200 °C for 120 minutes at atmospheric pressure. An individual microring is shown in Fig. 6.3. To ensure a resonance exists within the limited tuning range available by using the thermo-optic effect, we fabricate an array of rings with changing path lengths; these rings are shown in Fig. 6.4.

The next step involved depositing oxide on the bus waveguide while allowing the ring resonators themselves to remain unclad to maximize light interaction with fluids. There are a number of ways to accomplish this, including using lift-off processing on evaporated oxide as described in Chapters 4 and 5. Another method includes completely covering both bus waveguides and rings with a higher quality plasma enhanced chemical vapor deposition (PECVD) silicon dioxide. The oxide is selectively wet etched with a resist mask with hy-

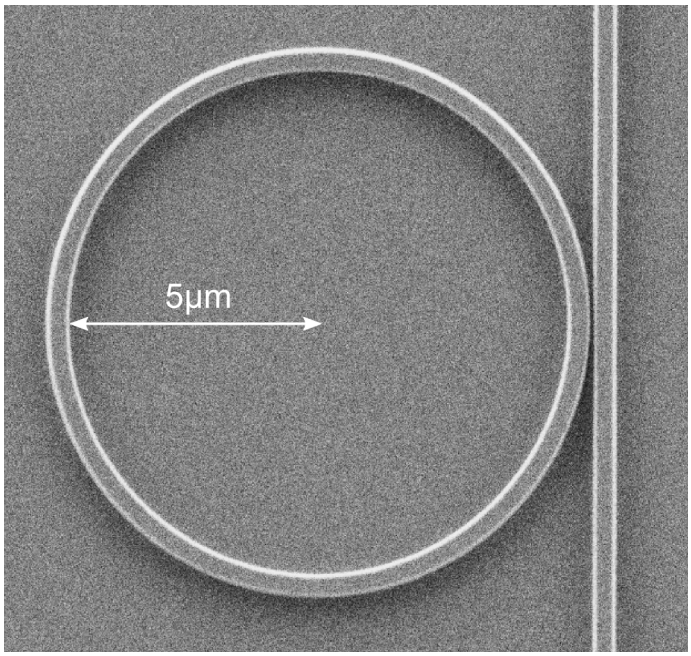

Figure 6.3: Scanning electron micrograph of a 5 µm radius silicon nitride microring resonator. The micorings used to detect the absorbance due to bacteria growth have twice the radius shown here.

drofluoric acid (HF) to expose the microrings. This etching can add roughness to the surface of the silicon nitride waveguide which will decrease the quality of the microring cavities. Therefore, I developed a new process which would allow us to deposit high quality PECVD silicon oxide on the wafer without exposing the microrings to an etching process. First we diced slivers of silicon from a bare wafer with dimensions of 1 mm by 25 mm. We carefully placed the silicon slivers on top our unclad microring devices and then placed larger pieces of silicon around the slivers to prevent them from moving during the tool loading process. The slivers of silicon are then removed after a 2 µm oxide deposition. Small amounts of damage to the waveguides was observed but this did not significantly affect waveguide losses and more importantly, the microrings were not affected. Finally, the devices were cut from the wafer with a dicing saw and

the end facets polished to improve optical coupling into the waveguides.

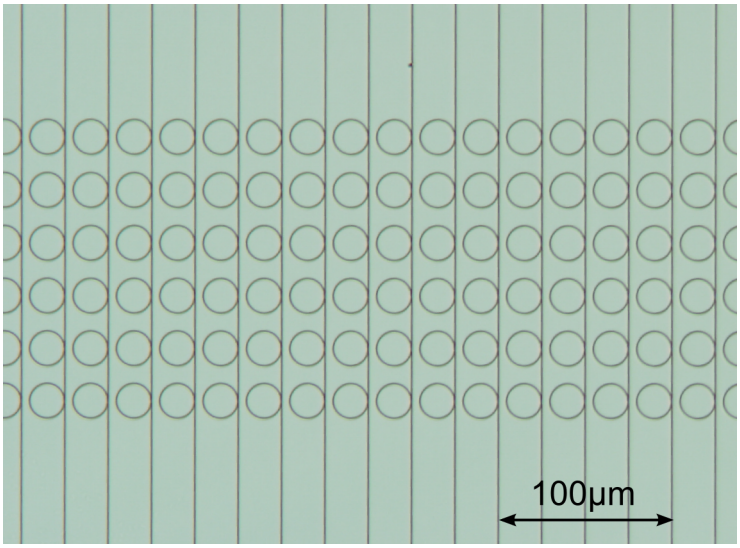

Figure 6.4: Microscope image of an array of silicon nitride waveguides with 8 microrings per waveguide with diameter of ≈20 µm. Each microring is differs in radius by 1.25 nm to vary the resonant wavelength position.

Microfluidic capabilities are integrated with the photonics using polydimethylsiloxane (PDMS) soft lithography processes [117]. A 30 µm tall by 350 µm wide channel mold was patterned with SU8 channels on a silicon wafer. PDMS is then poured over the channel mold, allowed to cure, and inlet holes are punched to access the channels. The microfluidic slab was then aligned on top of the unclad portion of the waveguides using a home-made contact aligner. The completed optofluidic device is shown in the coupling setup in Fig. 6.6

6.5 Materials and methods

The experimental process involved first growing *E. coli* in a liquid media containing XTT. Aliquots of bacteria solution were taken at various time and measured using the microring resonators to determine their optical absorbance. The following sections describe the materials and methods used to prepare the bacteria and perform the optical measurements.

6.5.1 Bacteria preparation

E. Coli (Strain K-12) bacteria were grown on 1.5 % w/v agar (DIFCO 281230) plates with 2 % w/v lysogeny broth (LB DIFCO 240230). Separately, solutions of growth media were mixed by dissolving the dehydraged LB culture media in Milli-Q (Millipore) water to a concentration of 2 % w/v. The tetrazolium salt XTT (Sigma-Aldrich) was separately dissolved in Milli-Q water to a working concentration of 2 mg/ml, stored at 4 °C and protected from light exposure. An aliquot of the XTT was warmed to 37 °C in a water bath before use. Then 1 ml of the XTT solution was added to 4 ml of the liquid growth media. The samples were then inoculated with ~10 colonies of *E. coli* and incubated at 37 °C.

At various times during incubation, 500 µL aliquots of the mixed bacteria suspension were taken and centrifuged at 5000 RPM for 5 minutes. The supernatant was used to eliminate non-specific optical scattering from the absorbance measurements. This scattering would not be present for the application discussed in Section 6.1, where bacteria are grown on top of a hydrogel covering a microring resonator. The optical absorbance of the supernate was measured

with a commercial spectrometer (Spectramax Plus 384) and then also using our microring resonator device.

6.5.2 Optical absorbance measurements with thermally-tuned microrings

The experimental setup is similar to that described in Chapter 5 and is shown in Fig. 6.5. The optical source used in these measurements is an Argon ion laser (Coherent Innova 90) with output powers of up to 100 mW producing a free space 1.4 mm diameter TEM_{oo} beam. The laser has a intracavity prism which allows manual selection between the discrete laser lines of 476.5 nm, 488.0 nm, 496.5 nm, and 514.5 nm. The free space beam is coupled into a visible PM fiber (ThorLabs P3-488PM-FC-5) using a fiber collimator (Thorlabs CFC-8X-A). The opposite end of the fiber is mounted in a fiber rotation chuck (Thorlabs HFR007) and is placed in physical contact with the polished input facet of the photonic chip. The chuck is graduated and can be rotated to excite either TE or TM polarized light in the photonic chip. The argon ion laser input light source was substituted at times by a tunable visible laser (Sacher Lasertechnik TEC 530) in order to aid in calibrating the device.

The photonic chip sits on a thermoelectric (TEC) heater module (TE Technology, Inc TE-23-1.0-1.3) along with a standard 10 kΩ thermistor attached to the top surface of the TEC module by thermal paste (shown in Fig. 6.6). The thermoelectric module is controlled by a temperature controller (ILX Lightwave LDT-5910B). The output light from the photonic chip is collimated by a high numerical aperture microscope objective (Olympus RMS40x) and sent through a

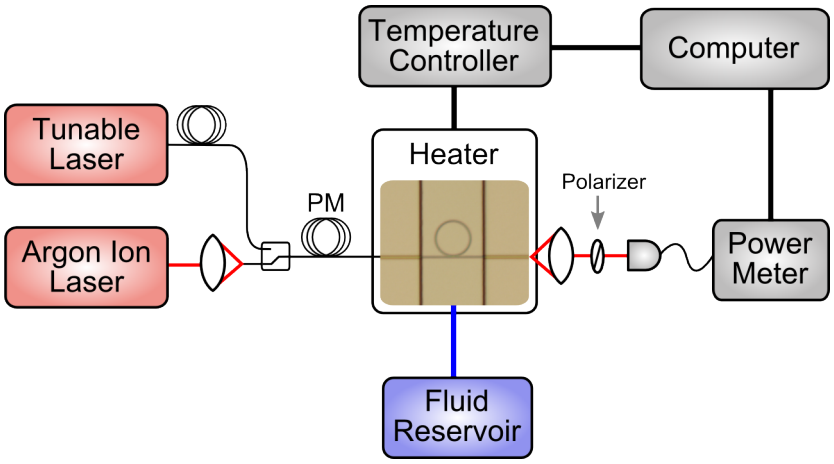

Figure 6.5: Schematic of the optical experimental setup used for absorption measurements of bacteria enzyme reaction products.

polarizing prism (Newport 10GL08AR.14) which can also be rotated to ensure measurement of either TE or TM polarized light. Three dimensional translation stages control the fiber tip and microscope objective to facilitate alignment and coupling. The power is measured with a photodetector (Newport 818-SL/CM) and power meter (Newport 2832-C). The various instruments are controlled by computer running a LabView (National Instruments) program. Analog output signals from the power meter and temperature controller are collected by a data acquisition card (National Instruments USB-6218).

Before each measurement, the temperature is allowed to stabilize to 20° Celsius. Data acquisition begins with a command to the temperature controller to maintain a new temperature of 60° Celsius. This causes a rapid and repeatable change in temperature of the photonic chip over a period of 30 seconds. The transmitted power from the bus waveguide and the temperature of the thermistor are recorded as a function of time. The devices were then calibrated using a 650 nm tunable source to determine how the resonance wavelength shifts dur-

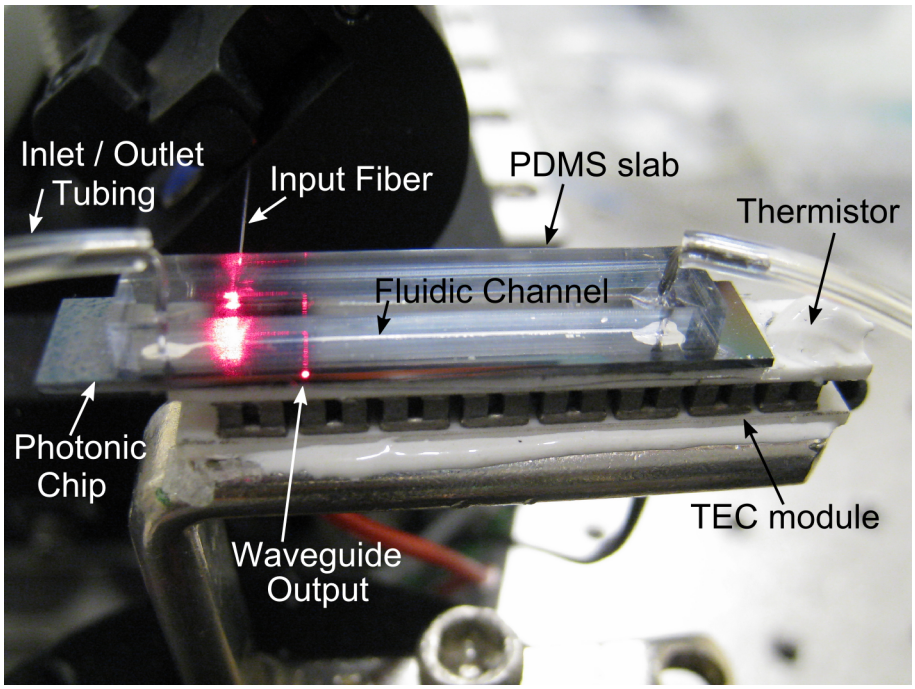

Figure 6.6: Various components of the coupling setup used to test optofluidic devices. Input light at 650 nm is being coupled into an S-shaped waveguide.

ing the heating time. This calibration, including calculations on how operation at 650 nm relates to operation at 496 nm is described in Appendix B . The results of this analysis are shown in Fig. 6.7 which shows the wavelength shift of a resonance over the data acquisition period for the operation wavelength of 496 nm. This allows us to plot the device transmission as a function of wavelength. The curve fitting methods described in previous chapters can then be applied to determine the ring parameters including the loss introduced be covering the ring with a fluid analyte.

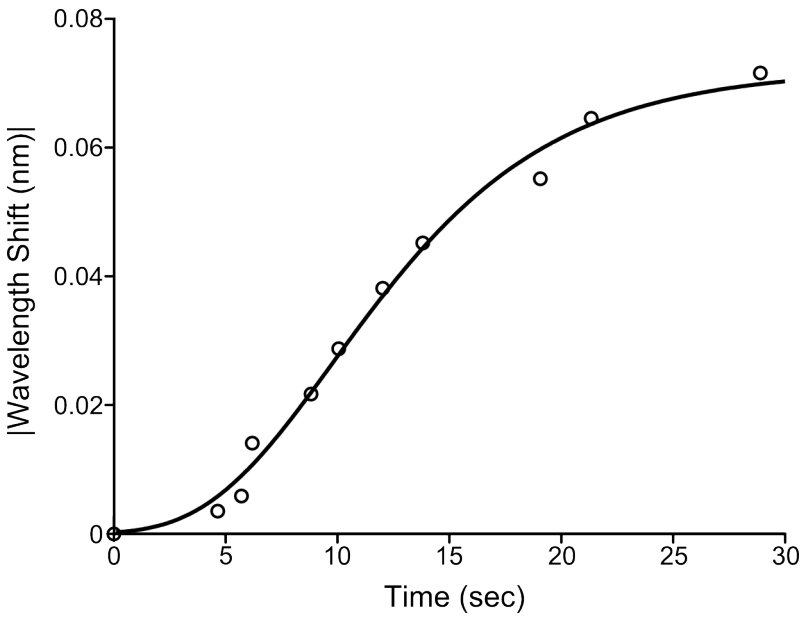

Figure 6.7: Resonance wavelength shift at 496 nm due to thermal tuning. Data points are determined by analyzing measurement at λ=650 nm and correcting for chromatic effects.

6.6 Results and discussion

Samples from the *E. coli* suspension, incubated with XTT, were extracted at roughly 8 hour time periods over the course of a 24 hour incubation period. These samples were measured with a conventional laboratory spectrophotometer as well as with our microring resonator. The absorbance of the various samples of bacteria are shown in Fig. 6.8.

The peak of the absorbance at 460 nm is in good agreement with the expected spectral features of the formazan dye [138]. The curves demonstrate that the bacterial cell count is increasing since the absorbance of the solution is proportional to the number of viable bacteria. We have marked the points on the curve that correspond to the absorbance of the aliquots at the wavelength of 496 nm,

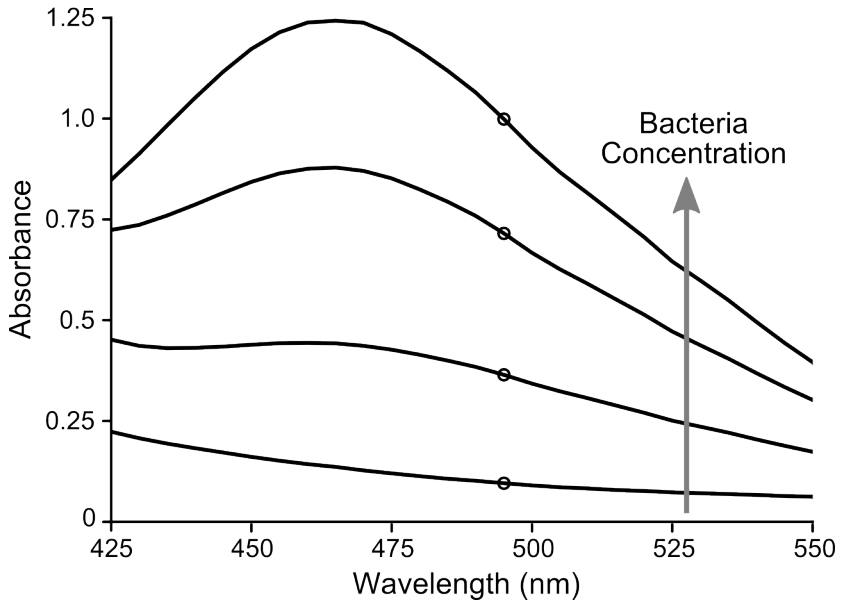

Figure 6.8: Absorbance due to XTT in bacteria samples measured with a commercial spectrophotometer. Absorbance values are circled at 496 nm, the Argon Ion laser line used during subsequent measurements performed with microrings.

which is the wavelength of operation of our microring device. The absorbance values at this wavelength are 0.095 AU, 0.364 AU, 0.715 AU, and .999 AU. The absorbance values are normalized to a path length equal to 1 cm.

The four samples are then individually measured by our optofluidic device. Fig. 6.9 shows an example of the resonance measurement along with a curve fitting to determine the microring attenuation coefficient.

There is very good agreement between the measured data and the curve fit using Eq. 6.1 demonstrating the successful use of our novel temperature tuning method for ring characterization. The limit of detection for an absorbance measurement is determined by taking a series of measurements of the same resonance and the resulting standard deviation for the resulting absorption mea-

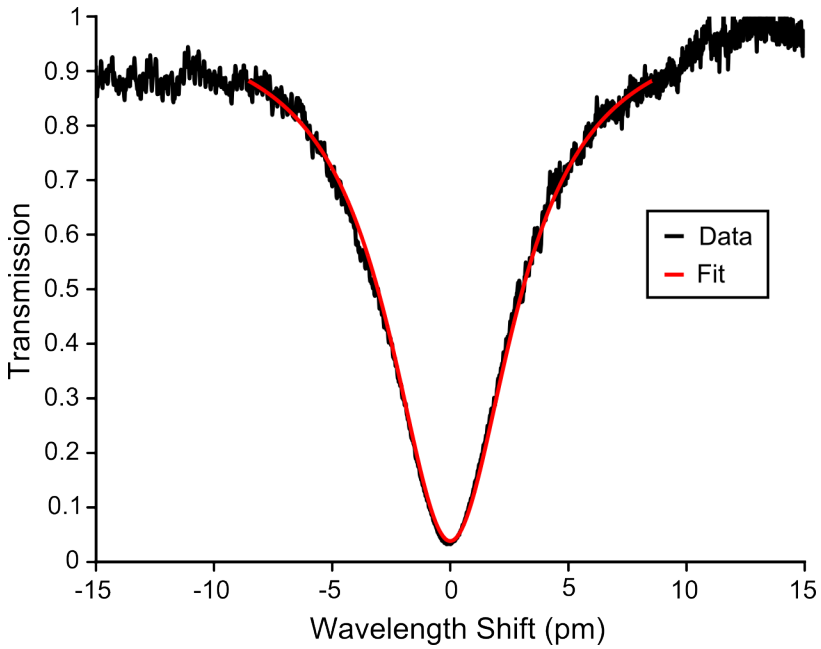

Figure 6.9: Measured (black) and curve fit (red) ring resonance transmission using the thermo-optic effect to shift the resonance position. The quality factor of this 10 μm radius silicon nitride microring is ~80,000.

surement is considered the noise floor of our experiment. After consecutive scans on the same resonance, the deviation in the extracted field attenuation coefficient leads to a detection limit of 0.1 cm^{-1} in the fluid absorption coefficient. This limit is similar to that previously reported in Chapters 2 and 3 for wavelength tuned resonance measurements showing that thermal tuning is a reliable and repeatable method to measure resonance features.

In Fig. 6.10, we show the results of measurements on the four bacterial samples, plotted as propagation loss in the ring as a function of the absorbance of the fluid measured. The ring propagation loss increases monotonically with absorbance of the fluid and the relationship is well described by a linear fit. The change in the microring performance is clearly visible over the tested range

of absorbance values of 0 to 1 AU. These results demonstrate the ability of a microring resonator to measure cell proliferation and viability in chromogenic assays.

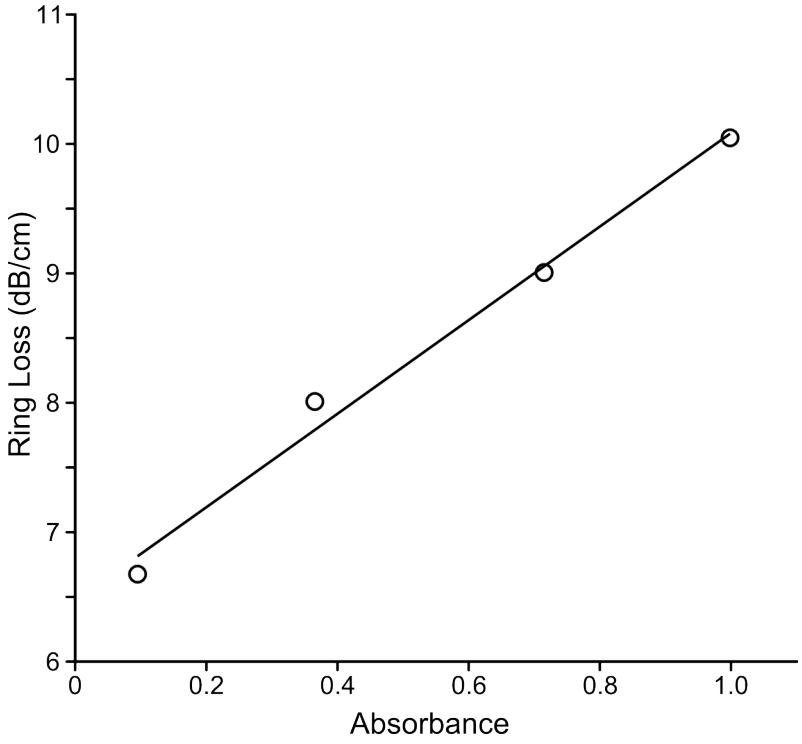

Figure 6.10: Extracted ring propagation loss from curve fitting to resonances covered with fluids of various absorbance values generated by a chromogenic bacterial enzyme catalyzed reaction.

The limit of detection of 0.1 cm^{-1} for our microring resonator is larger than the accuracy of a laboratory spectrometer which are typically below 0.01 cm^{-1}. However, the microring resonator is far superior in terms of sensitivity per volume of fluid analyzed. The microchannel used in these experiments required about ~2 nl of volume to cover the ring which is about 5 orders of magnitude smaller then a the volume required to fill a microwell plate. If we consider only the volume which overlaps with the evanescent field of the ring resonator, see Fig. 6.1b, the effective volume for the sensor is ~5 fL.

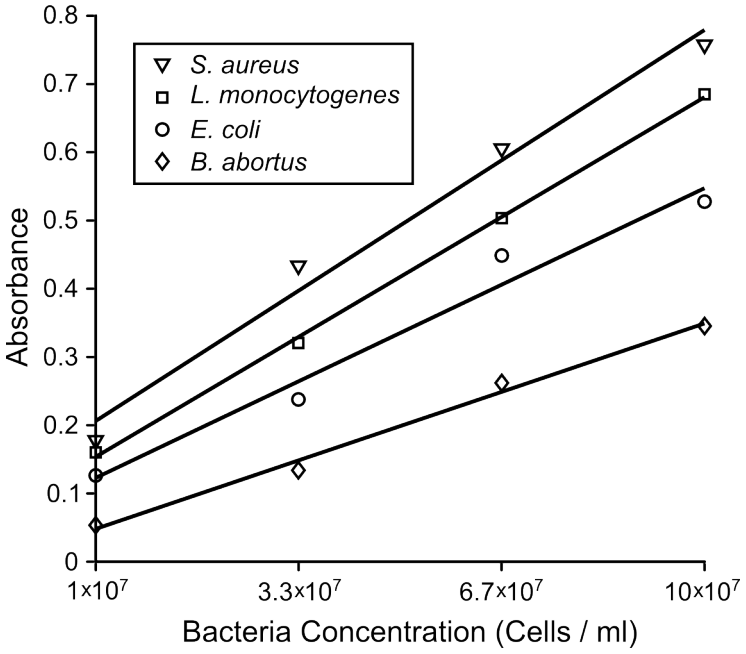

Figure 6.11: Optical absorbance at 450 nm for various bacteria incubated for 30 min in a solution containing XTT and coenzyme Q. Reproduced with permission from [4].

The use of XTT in chromogenic assays has been studied extensively and we can use results from literature to determine the concentration of the bacteria as a function of optical absorbance from the cleavage of XTT. Fig. 6.11 shows the absorbance at 450 nm of various bacteria using XTT with coenzyme Q[4]. According to the absorption spectra of XTT (Fig. 6.8), the absorption at 450 nm is approximately the same as the absorption at 496 nm. Therefore we can use Fig. 6.11 to estimate the sensitivity of our own device. The maximum concentration of *E. coli* bacteria is $1x10^8$ cells per ml and this led to an absorbance of 0.6 which we demonstrated is within the dynamic range of our microring device. At this bacteria concentration, the number of bacteria required to generate an absorbance of 0.6 within the 2 nl channel volume is 200 cells. Or equivalently, this amounts to a sensitivity of 1 bacterium per 10 picoliter volume which is sev-

eral orders of magnitude larger than the sensing volume of the ring resonator. This means that the ring would be able to detect the absorbance generated by a single bacterium in a droplet of 10 picoliters sitting on top of the microring resonator.

The ability to manipulate picoliter volumes of fluids is within the capability of current microfluidic technology [139, 140]. Therefore, the demonstrated microring resonator device can be used to perform fundamental single bacterium studies. The proposed platform of growing bacteria on thin layers of chromogenic hydrogels is promising. Further studies on the deposition of ~100 nm layer hydrogels and its change in absorbance due to bacteria metabolic activity need to be carried out.

6.7 Summary

I have demonstrated a novel measurement technique which allows single wavelength lasers to be used to measure optical absorbance on an integrated optofluidic device. Using silicon nitride ring resonators with 10 μm radius and quality factors greater than 80,000, we measured the absorption due to the cleavage of XTT by the metabolic activity of *E. coli* bacteria. The limit of detection of the device corresponds to a fluid absorption coefficient of 0.1 cm^{-1} and can detect the absorbance due to a single bacterium in a 10 pL volume, which is 2000 times larger than its own sensing volume. These results demonstrate the suitability of microring resonators as inexpensive, compact and sensitive sensors for chromogenic assays and single cell studies.

CHAPTER 7

SUMMARY AND FUTURE WORK

Lab-on-a-chip devices which combine multiple fluid-handling processes onto a single planar format have the potential to revolutionize the healthcare and life science industries. By leveraging fabrication techniques developed for the microelectronics industry, this technology can offer cheap, miniaturized, and high-throughput tools which can quickly peform multiplexed analysis with low sample consumption. One of the main hurdles to the widespread adoption of lab-on-a-chips is their dependence on traditional laboratory equipment to operate. To take full advantage of the potential for compact and portable diagnostic tools, these devices need to be highly versatile with minimal external requirements. Labor intensive procedures such as sample preparation and detection have to be integrated into the capabilities of these systems. An important toolset to incorporate onto these planar devices is optical analysis which is one of the most fundamental ways in which chemicals are analyzed. Towards this goal, I have investigated the combination of integrated optical components with microfluidics to develop chips with advanced functionalities. The main contribution of this work is demonstrating how optical microcavities can improve the performance and versatility of optofluidic devices to ultimately enable stand-alone fluid analysis systems. I hope that this list of future applications of resonator-based optofluidic devices demonstrates the enormous potential of these devices to make a significant impact in a wide area of technologies.

Silicon nitride waveguides with microfluidic channels were used to simultaneously manipulate and characterize microscale particles. By using broadband light from a supercontinuum source, we were able to excite and measure whis-

pering gallery modes within polystyrene microspheres for the first time. Future work in this area could take advantage of the unique optical properties of supercontinuum sources for applications including on-chip scattering [84] and Raman [85] spectroscopy. The high spatial coherence but low temporal coherence of supercontinuum sources make them an ideal light source for broadband on-chip optical coherence tomography [141, 142]. Microspheres are commonly used in molecular diagnostic [143] and sensing applications [144], however, detection often relies on free space optical components. The use of integrated waveguides for microsphere analysis could enable real-time measurement of molecular binding events by optically trapping a microsphere and measuring changes in resonance features. Further research is also needed to quantify the performance of these devices to measure clinically relevant concentrations of analytes in complex media. The characterization capabilities demonstrated here could also be applied to flow cytometery [145] to enable high-throughput microfluidic devices by monitoring waveguide transmission when cells flow through the evanescent field.

Many of these possible applications depend on the efficient coupling of light from the waveguide to the microsphere which depends on careful control of their separation distance. Microspheres in direct contact with the waveguide surface are over-coupled and therefore an oxide separation layer could be deposited on top of the waveguide to achieve critical coupling. The tradeoff between optical forces and coupling gap needs to be investigated to determine whether waveguide optical trapping or another trapping modality, such as electrical [146] or microfluidic [147], is best suitable for waveguide-based microsphere analysis.

Much of this dissertation focuses on the use of microring resonators to increase the sensitivity of optical absorbance measurements. We began with a proof a principle experiment where cavity enhancement from microcavities effectively increased the optical interaction length between light and an analyte fluid. This was the first demonstration of ring resonance curve fitting to determine the absorption spectrum of a fluid for a broad range of wavelengths. This proof of concept experiment can be followed up with research into the suitability and performance of this technology in specific applications in food safety [148] or pharmaceutical analysis [149] which utilize the same wavelength regime. The sensitivity of the devices can be improved by lowering the ring losses which would translate to a greater interaction length between light and analyzing fluid. The main loss mechanism is waveguide sidewall roughness which can be reduced by optimizing the fabrication process. The principle of operation could be extended to other wavelength regimes by appropriate choice of waveguide materials. Devices for the infrared regime, where chemical vibrations provide rich data on the composition of chemical analytes [150], could be fabricated using the silicon-on-sapphire material system [151]. Waveguides and ring resonators suitable for wavelengths between 200-400 nm would enable analysis on DNA/RNA and proteins which have characteristic absorption features in the ultraviolet. Possible materials for UV-transparent integrated optics include diamond [152] and silicon oxynitride [57]. It would also be useful to investigate broadband light sources, such as light emitting diodes, to perform similar cavity enhanced measurements [153]. This would eliminate the need for a tunable laser and increase the bandwidth of the measurement since the tuning range of lasers is limited.

Taking advantage of the low analyte consumption and high sensitivity of microcavity-based optical absorption measurements, we applied the technique to the visible regime for bioanalysis applications. We measured the colored products of enzyme catalyzed reactions with silicon nitride microrings and demonstrated absorbance measurements over ranges typical of commercial spectrophotometers. We calculate the device is sensitive to the activity of individual enzymes within a few minutes. This platform can be used to miniaturize immunoassays to enable compact and sensitive diagnostic tools [154]. Demonstration of a completely integrated and automated ELISA platform with detection of real-world samples would be a major contribution to the field. The ability to measure absorption products in sub-picoliter volumes make microring resonators a promising component for planar optical detection in such a system. Another interesting area of research would be the combination of droplet based microfluidics [155] with microring resonators for integrated fluid analysis. These devices manipulate femtoliter to nanoliter volume drops of liquid for biomedical applications. By moving a droplet on top of a microring resonstor, the optical absorbance of each droplet could be determined and the chemical reactions taking place can be monitored.

I have also described my work towards a bacteria biosensor which is fast, sensitive, and cost-effective; a combination of qualities which are currently unavailable with current detection methods. We showed that cavity enhancement in a microring could be used to detect bacterial growth within solution and that in principle, the growth of individual bacteria could be monitored. The ability to quickly detect the presence of viable bacteria would be especially useful in combination with microwell devices [119] which can include hundreds of microscale reaction chambers. Instead of free space imaging optics being used to

detect microwell absorption or fluorescence, microring resonators could be fabricated on the bottom surface of each well. The microcavities could detect any changes in the optical properties of the fluid analytes and therefore enable a completely integrated and highly multiplexed optical biosensor.

The ability to perform on-chip optical measurements on liquids is an essential capability for life science applications and I have shown that resonance-based methods are an effective means to increase device performance. By exploiting the unique characteristics of optical microcavities, compact and highly sensitive devices can be realized. Although the commercial progress of lab-on-a-chip devices has been slower than initially hoped, I strongly believe in their potential to have a significant impact on society. It is very likely that over the next decade these technologies will play a more prominent role in our lives and I hope that this work helps researchers to develop new solutions by illustrating the potential of optofluidic devices.

APPENDIX A

FABRICATION PROCEDURES FOR OPTOFLUIDIC DEVICES

In this section I describe in detail the steps to fabricate the various photonic components used in this dissertation. Every effort has been made to include any 'tricks' to allow an interested reader to reproduce these structures with minimal difficulty. All the photonic structures were created at the Cornell NanoScale Science and Technology Facility. The tools and recipes described in this section refer to equipment available at this facility.

A.1 Silicon Nitride Waveguides and Ring Resonators

Silicon nitride is a dielectric material commonly used as an insulator in microelectronics. The benefits of silicon nitride as a waveguiding material include the availability of mature processing techniques, a high refractive index (n=2.0), and low optical absorption in the visible and near infrared. The silicon nitride photonic structures used in this research were fabricated starting with standard 4 inch silicon wafer (Silicon Quest International,Inc.). The wafers are MOS cleaned and then put into a furnace tube for oxidation. A wet oxidation is performed on the wafers for 20 hours to form a silicon dioxide layer of approximately 4 μm on the silicon wafer. The wet oxidation is sandwiched between two 10 minute dry oxidation steps in order to improve the quality of the upper and lower oxide interfaces. The oxide thickness across the wafer is measured using filmetrics and results in RMS deviations on the order of several nanometers.

Once the lower index buffer layer of oxide has been grown, the waveguid-

ing layer of silicon nitride can be deposited using low pressure chemical vapor deposition (LPCVD). Two bare silicon baffle wafers are placed on either side of the oxidized silicon wafers to increase the uniformity of the nitride deposition. The stoichiometric recipe deposits silicon nitride at a rate of ~3.6 nm/min and has a refractive index ~2.0. The wafers are then prepared for patterning by performing a hot piranha (sulfuric acid and hydrogen peroxide) clean on a Hamatech wafer processor. An adhesion promotion layer for the subsequent electron beam resist is then applied. Surpass 3000 (DisChem, Inc) is dispensed at a rate of ~2 ml/sec continuously for 30 seconds at a spin speed of 250 RPM. During the first 30 seconds and the final 30 seconds of the spin cycle, deionized water is continuously dispensed. The wafer is immediately dried by spinning for 90 sec at 2000 RPM with 1000 RPM/sec acceleration.

An electron beam resist (MaN 2403) was then spun on top of the wafer. A resist film thickness of ~300 nm results from a 90 sec spin at 2000 RPM and 1000 RPM/sec. After a 1 minute bake at 90°C, a conductive layer of ESPACER (Showa Denko America, Inc) was also spun onto the wafer to prevent stitching errors during electron beam exposure due to charging. The wafer was covered with green ESPACER formulation and spun for 90 sec at 2000 RPM and 1000 RPM/sec and was allowed to sit covered in the fume hood for 30 minutes prior to exposure. Patterns in GDS format were created and converted to files compatible with the 100 kV JEOL 9300FS electron beam system using Layout BEAMER (GenISys). The wafer was exposed at 2 nA of e-beam current with a dose of 1000 $\mu m/\mu m^2$.

After exposure, the wafer was rinsed with deionized water to remove the ESPACER and then developed in a Hamatech wafer processor using a 90 sec

300 MIF process. Development removes the bulk of resist from wafer locations that were not exposed to electrons, and then a descum to remove residual resist was performed on a Branson P2000 barrel etcher using a 2 minute resist removal recipe. The resist was then reflowed to smooth out any sidewall roughness due to the discrete e-beam shot location placement. Reflow was performed on a hot plate for 5 min at 145 °C.

The devices were then etched using inductively coupled reactive ion etching (ICP RIE) with a CHF_3/O_2 process chemistry in an Oxford PlasmaLab 100 system. A 10 minute plasma clean was first performed on a silicon wafer to clean the chamber followed by a 2 minute chamber seasoning step using the nitride etching CHF_3/O_2 process. This seasoning step may not be necessary and some evidence showed it may have contributed to unwanted polymerization on the wafer. The seasoning step is used to characterize the etch rate which is ~85 nm/min. The etch time was then calculated for the thickness of nitride on the patterned wafer. We typically add an additional 25% to the etch time to allow for the slower etch rate which occurs at narrow gaps in the photonic structures. Filmetrics is used to verify the complete removal of the silicon nitride from the unpatterned portions of the wafer.

The resist which is still left on top of the photonic structures is removed using a resist hot strip bath which contains a heated solvent. This step may be etching into the silicon nitride and so an alternative method may prove beneficial. Any remaining resist is removed using an Gasonics Aura 1000 resist strip tool with the 03F recipe. After a MOS clean of the wafer, the wafer is annealed in a furnace oxide tube using a nitrogen anneal recipe for 3 hours at 1200°C to reduce material absorption losses.

In order to improve coupling into the waveguides and reduce scattering losses, the unclad waveguides can be covered with silicon dioxide. Since our applications required the ring resonators and trapping portions of the waveguide to remain unclad, a lift off process was used to achieve this outcome. A 1 minute plasma clean was first performed on the Bransom etcher to prepare the wafer. Then LOR-5A lift off resist was spun on the wafer at 3000 RPM and 1000 RPM/sec acceleration for 60 sec. This layer must be thicker (typically 1.5x) than the layer of oxide that will be deposited in order for the lift off to work properly. The wafer is then baked at 180 °C for 5 minutes. A top layer of resist is then spun on; we typically use a photo resist such as Shipley 1827 with spin parameters of 3000 RPM and 500 RPM/sec for 60 seconds. The wafer is again baked at 115 °C for 1 min. We then use an ABM contact aligner to expose the areas of our wafer which we want to cover with oxide. We typically over expose during this step (~20 seconds) because the feature sizes are on the order of 100's of microns and are not critical. We then develop the wafer at 60 second intervals until the resist is cleared and an undercut of the lift off resist is visible. This typically takes ~4 minutes for the ~micron thick resists. Filmetrics is used to check resist removal and the wafer is prepared for evaporation by performing a 1 minute descum on the Branson etcher.

Evaporation of silicon dioxide is performed on a CVC SC4500 e-gun evaporator. A single crucible of silicon dioxide is used per 750 nm of required deposition thickness. Evaporation is performed slowly at first, at the rate of 0.3-0.4 Å/sec to promote adhesion. After 20 nm of deposition, the rate is increased to 1 Å/sec. The deposition rate is increased by ~1 Å/sec for every 100 nm of oxide deposited up to a maximum of 10 Å/sec. The quality of the oxide is checked using filmetrics and we typically measure a refractive index of n=1.42 which

is lower than oxide deposition using other methods such as plasma enhanced chemical vapor deposition (PECVD). However, testing with these devices has shown evaporated oxide is of sufficient quality to enable coupling losses of less then 10 dB. Note that the CNF no longer allows more than 100 nm of oxide to be evaporated.

The lift off process is completed by allowing the wafer to sit in Microposit 1165 for ~12 hours. The wafers are then cleaned using acetone and isopropyl alcohol and covered with photoresist such as Shipley 1813 to protect the unclad photonic structures during the next step of dicing. The wafer is divided into small rectangular chips on the order of several millimeters long and one to two centimeters wide. A KS 7100 dicing saw with a silicon blade is using to dice the wafer. The dicing blade leaves ~1-3 microns of RMS surface roughness on the chip edge. To improve coupling this edge is polished using an Allied Multiprep polisher with 1 μm and 0.5 μm diamond lapping films.

A.2 Microfluidic channels and integration with nanophotonics

The microfluidic channels fabricated for this research were made from poly-dimethylsiloxane (PDMS) using soft lithography processes. The overall process includes steps to create a wafer mask for the channels which are then imprinted onto PDMS. The wafer mask starts as a 4 inch silicon wafer which is cleaned using a hot piranha clean (sulfuric acid and hydrogen peroxide) on a Hamatech wafer processor. To create channels with a height of ~30 μm, SU8 formulation 2025 is spun at 500 RPM for 10 seconds with a ramp of 100 RPM/sec, followed by a 3000 RPM spin for 30 seconds and ramp of 300 RPM/sec. The wafer is then

baked at 65 °C for 3 minutes and then moved to a 95 °C hot plate for 5 minutes. Separately, a 5 inch chrome mask with a 2D array of fluidic channels is created using a 3600F PG mask writer. This mask is then developed and etched using a Hamatech wafer processor and the residual resist is removed with a hot resist strip bath.

The photomask is used to pattern the fluidic channels onto the SU8-clad wafer using a ABM contact aligner. The wafer is exposed for 20 seconds and then baked for 1 minute at 65 °C and 5 minutes at 95 °C. The wafer is then developed for 5 minutes with SU8 developer followed by a wash with isopropyl alcohol. If a white film develops during this step then the wafer requires more time under the SU8 developer. The wafer is finally hard-baked at 185 °C for 10 minutes.

The wafer with the array of SU8 fluidic channel molds is then placed into a plastic 6 inch petri dish. In a separate dish the PDMS is prepared by mixing the base and curing agent (Silicon Elastomer 184, Dow Corning) in a 10:1 ratio measured by weight. A total weight of 50 grams is sufficient for a PDMS slab thicknesses of ~2 mm. The two components are mixed with a glass rod for 5 minutes which will also incorporate air bubbles into the mixture. The air is removed from the PDMS using a vacuum chamber and vacuum pump at 1 minute intervals until the PDMS mixture stops bubbling which indicates all the air has been expelled. The PDMS is then poured on top of the SU8 channel mold wafer and the petri dish is baked in an oven at 85 °C for 2 hours.

After the PDMS has hardened, the microfluidic channels are cut out using a scalpel and the PDMS slab is pulled out with tweezers. Conventional invisible tape is used to clean the surface of the PDMS. Gooseneck fiber illumination is

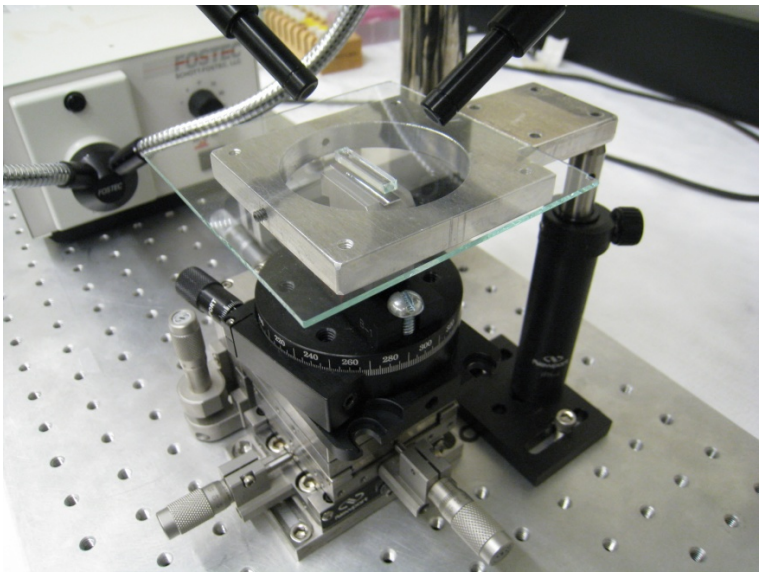

Figure A.1: Aligner built to allow microfluidic channels to be accurately positioned on top of a photonic chip.

used to highlight the contours of the fluidic channel which is placed channels facing upwards on a cutting mat. A 50 μm biopsy punch (Ted Pella, Inc) is used to punch inlet and outlet holes through the PDMS to provide access to the microfluidic channels.

The next step includes aligning the PDMS slab with microfluidic channels on top of the photonic chip. This process ensures that the fluids will reach and interact with the intended portions of the photonic chip. As shown in Fig. A.1, the aligner includes a 3 dimensional translation stage on the bottom and a rotational stage to fix angle offsets. The photonic chip is placed on top of these stages which allows motion relative to the microfluidic channels. The PDMS slab hangs upside down on the bottom of a square piece of glass with the fluidic channels facing downward toward the photonic chip. The setup is illuminated and observed with a long working distance microscope. The photonic chip is brought towards the PDMS slab until the waveguides and the microfluidics can

both be seen through the microscope. The photonic chip is aligned beneath the PDMS slab and then brought into contact with the PDMS. In order to permanently bond the PDMS to the photonic chip, the PDMS slab can be plasma cleaned prior to the contact alignment.

The device can then be connected to tubing to flow fluids through the channels. A 3 mm length of hypodermic metal tubing (HTX-24T-12-10, Small Parts) is inserted halfway into tygon tubing (TGY-020, Small Parts). The other half of the metal tubing is inserted into the PDMS hole created with the biopsy punch. At this point the completed optofluidic device can be attached to a syringe or reservoir for pressure driven flow.

APPENDIX B

CALIBRATING THERMALLY-TUNED MICRORING TRANSMISSION MEASUREMENTS

I described in Chapter 6, how the thermo-optic effect can be used to change the refractive index of a ring to shift its resonance wavelength. This method allows a single wavelength light source to be used to characterize a microring, instead of sweeping the frequency with a tunable laser. One challenge in implementing this innovation, is that in order to extract useful information from the ring transmission spectrum, the temperature tuning has to be calibrated. I can only apply the curve fitting techniques described in Chapter 4 and 5 if we know the transmission as a function of wavelength, not temperature.

There are several methods that can be used to calibrate the temperature response of a microring resonator. The easiest method would be to use a tunable light source at the wavelength we want to calibrate the device for. The resonance wavelength shift can then be measured directly. Unfortunately, tunable sources do not exist for all wavelength ranges of interest and the lasers that are available are expensive. Another method for calibration is to use a single wavelength source and a very large cavity with closely spaced resonance features. If we tune across across many of these features, we can determine the total wavelength shift if we know the free spectral range of the cavity and count the number of resonances we pass. Unfortunately, this method has some practical limitations if we want to keep the devices compact. For example, to have a FSR=10 pm, we would need a silicon nitride cavity to be over 1 cm in length. Reflections at the end facets of the waveguide can act like a long Fabry-Perot cavity and these features can be used for calibration if the cladding material of

the bus waveguide is the same as the cladding on the microring. In our case, the bus waveguides have a glass cladding, while the rings are covered by the fluid analyte we are studying.

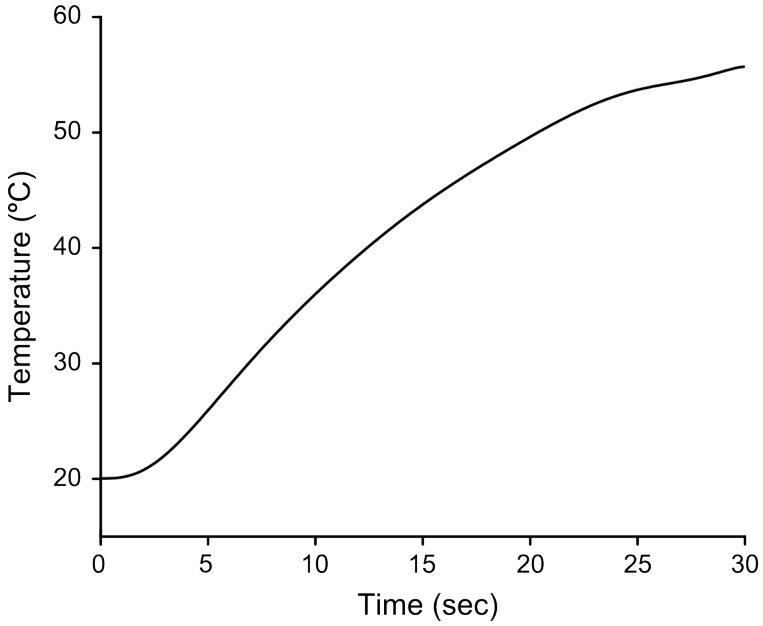

Figure B.1: Temperature change of the thermistor in contact with the TEC module controlling the temperature of the photonic chip.

The method of calibration we used for measurements at 496 nm involved several steps. We used a tunable light source at 650 nm to measure the wavelength shift with temperature with no fluid in the channels, i.e. simply air covering the microrings. This measurement allows us to determine the thermo-optic coefficient of our silicon nitride waveguide material. We then covered our rings with the growth media fluids, and again measured the wavelength shift with temperature. This measurement, along with the air-clad measurement, provided us with the thermo-optic coefficient of the cladding fluid. Since the thermo-optic coefficient of glass in the visible regime is well-known, we then used the measured thermo-optic coefficients to determine what the wavelength

shift would be at 496 nm. The details of these steps are described below.

A plot of the thermistor temperature for a typical run is shown in Fig. B.1. Repeated temperature scans shown an average temperature deviation of less then 1% between consecutive runs demonstrating that we can reliably and repeatably affect the temperature of our photonc structures.

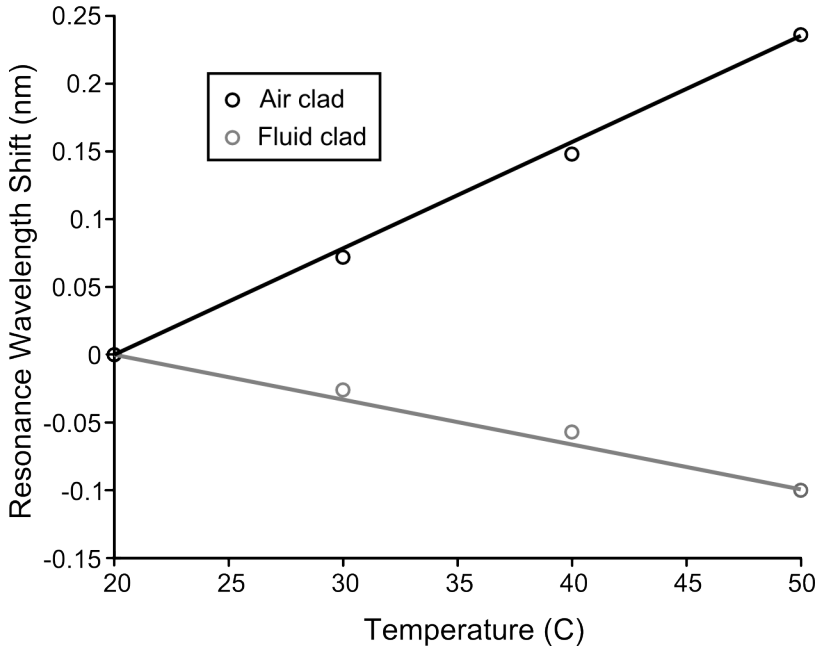

Figure B.2: Resonant wavelength shift of a 10 μm radius silicon nitride ring resonator for an air clad and fluid clad ring. The fluid is a 2% LB medium for bacterial growth. Note that the shift becomes negative for the fluid clad ring because of the large negative thermo-optic coefficeint of the fluid.

To determine the resonance shift as a function of temperature, we set the temperature of the TEC module and tuned the 650 nm visible laser into a ring resonance, then recorded the wavelength with a wavemeter. We repeat this process for a number of temperatures and the resonance wavelength shift is shown in Fig. B.2 for the two cases of an unclad ring and a ring covered with the bacterial growth medium of Lysogeny broth (LB). The change in the resonance

wavelength λ_o as a function of temperature T, is well described by a linear fit and the slope is the resonant wavelength shift per degree. The values for $\frac{d\lambda_o}{dT}$ are 7.8 pm $^\circ C^{-1}$ and -3.3 pm $^\circ C^{-1}$ for the air and fluid clad rings respectively.

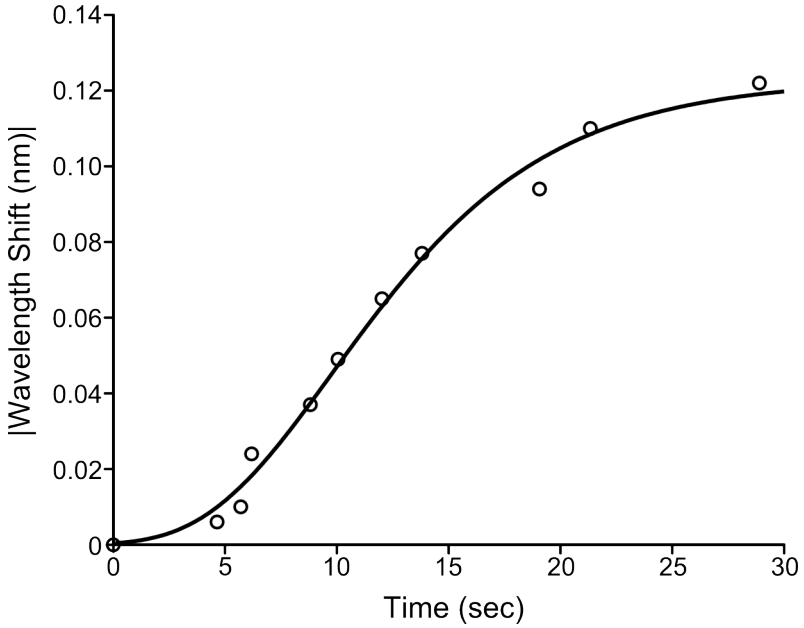

Figure B.3: Absolute value of the wavelength shift vs time for our 10 μm radius silicon nitride ring resonator covered with LB growth media. Circles are data points and the line is a sigmoid fit.

Values for $\frac{d\lambda_o}{dT}$ coupled with the thermistor temperature as a function of time (Fig. B.1) can be used to provide a first order approximation of the wavelength shift over time. However, due to different heat conductivit

The data points in Fig. B.3 are fit to the following sigmoid equation:

$$\lambda_{shift}(t) = A\, e^{-e^{-B(t-C)}} \tag{B.1}$$

where A, B, and C are fitting coefficients used to describe the wavelength shift, λ_{shift}, as a function of time, t. The coefficients are found to be:

A=0.12,B=0.18, and C=9.79. According to the Fig. B.3, our experimental setup is able to tune the resonant wavelength of a 10 μm radius microring by over 0.1 nm over a time period of 30 seconds by applying a temperature change of approximately 40 $^{\circ}C$. These measurements were performed at a wavelength of 650 nm where we had access to a tunable source, but the goal is to calibrate the device for its operation wavelength of 496 nm. Because the confinement of the optical mode in the waveguide changes depending on the wavelength of operation, we calculate how the wavelength shift measured in Fig. B.3 would change for the shorter wavelength of operation. Table B.1 shows the simulated effective and group indices, and confinement factors for the relevant optical modes.

Table B.1: Optical Mode Parameters for a 10 μm Radius Silicon Nitride Microring (150 nm x 400 nm)

	TE Air-Clad	TE Water-Clad	TM Water-Clad
$\lambda(nm)$	650	650	496
n_{eff}	1.486	1.540	1.590
n_g	2.040	2.012	2.128
$\Gamma_{Si_3N_4}$	0.554	0.682	0.673
Γ_{SiO_2}	0.346	0.233	0.213
$\Gamma_{cladding}$	0.100	0.222	0.298

To calculate $\frac{d\lambda}{dT}$ for 496 nm, we need to know the thermo-optic coefficients $\frac{dn}{dT}$ of our silicon nitride and cladding fluid. These numbers can be determined from our previous measurements of the $\frac{d\lambda}{dT}$ at 650 nm. Applying Eq. 6.7 and 6.8 for the case of the air clad resonator at 650 nm, we calculate $\frac{dn_{Si_3N_4}}{dT}$ to be equal to 3.8x10^5 K^{-1} which is good agreement with its known value in the infrared of 4.0x10^5 K^{-1}. Using this value for silicon nitride, we can then determine the thermo-optic coefficient of the growth media in the same way and find $\frac{dn_{LB}}{dT}$=-

$17.5 \times 10^5\ K^{-1}$. The growth medium is mostly water so it is not surprising that the growth media has a similarly large and negative thermo-optic coefficient.

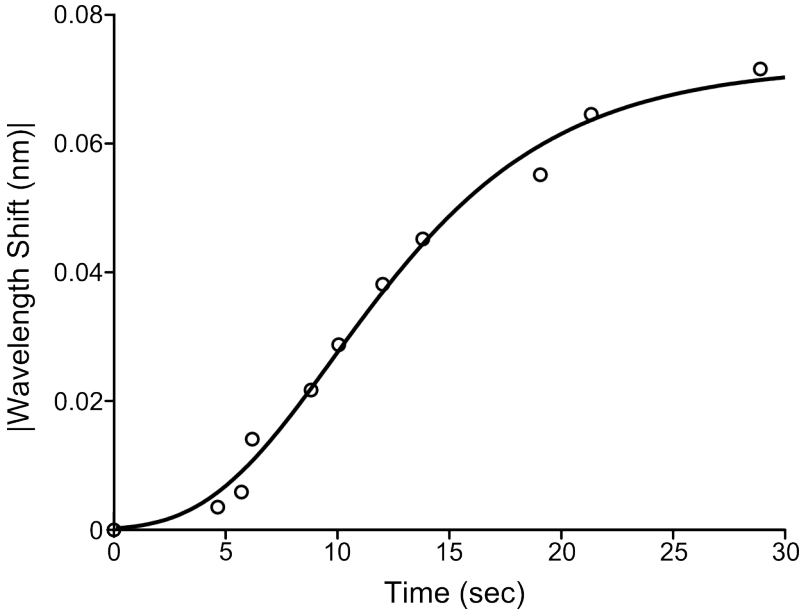

Figure B.4: Resonance wavelength shift at 496 nm due to thermal tuning. Data points are determined by analyzing measurement at λ=650 nm and correcting for chromatic effects.

Using the experimentally determined thermo-optic coefficients at 650 nm and the waveguide parameters from Table B.1, we can then determine how the resonance shift at the experiment wavelength of 496 nm relates to the measured shift at 650 nm. Using Eq. 6.7 and we calculate that the shift at the lower wavelength will be reduced by 40%. The wavelength-corrected resonance shift as a function of time for our experimental setup is shown in Fig. B.4 which completely characterizes the device response with temperature when excited with light a wavelength of 496 nm.

BIBLIOGRAPHY

[1] F. K. Balagadde, L. C. You, C. L. Hansen, F. H. Arnold, and S. R. Quake. Long-term monitoring of bacteria undergoing programmed population control in a microchemostat. *Science*, 309(5731):137–140, 2005.

[2] Jiangang Zhu, Sahin Kaya Ozdemir, Yun-Feng Xiao, Lin Li, Lina He, Da-Ren Chen, and Lan Yang. On-chip single nanoparticle detection and sizing by mode splitting in an ultrahigh-q microresonator. *Nat Photon*, 4(1):46–49, 2010.

[3] Toshihiko Baba. Photonic crystals: Remember the light. *Nat Photon*, 1(1):11–12, 2007.

[4] Mark G. Stevens and Steven C. Olsen. Comparative analysis of using mtt and xtt in colorimetric assays for quantitating bovine neutrophil bactericidal activity. *Journal of Immunological Methods*, 157(1-2):225–231, 1993.

[5] Lidija Malic, Daniel Brassard, Teodor Veres, and Maryam Tabrizian. Integration and detection of biochemical assays in digital microfluidic loc devices. *Lab on a Chip*, 10(4):418–431, 2010.

[6] Lonnie J. Lucas, Jennine N. Chesler, and Jeong-Yeol Yoon. Lab-on-a-chip immunoassay for multiple antibodies using microsphere light scattering and quantum dot emission. *Biosensors and Bioelectronics*, 23(5):675–681, 2007.

[7] Jaephil Do and Chong H. Ahn. A polymer lab-on-a-chip for magnetic immunoassay with on-chip sampling and detection capabilities. *Lab on a Chip*, 8(4):542–549, 2008.

[8] Roberto Gambari, Monica Borgatti, Enrica Fabbri, Riccardo Gavioli, Cinzia Fortini, Claudio Nastruzzi, Luigi Altomare, Melanie Abonnenc, Nicol Manaresi, Gianni Medoro, Aldo Romani, Marco Tartagni, and Roberto Guerrieri. *Lab-on-a-Chip Devices for Cellular Arrays Based on Dielectrophoresis*, pages 231–243. Humana Press, 2007.

[9] Robin Hui Liu, Jianing Yang, Ralf Lenigk, Justin Bonanno, and Piotr Grodzinski. Self-contained, fully integrated biochip for sample preparation, polymerase chain reaction amplification, and dna microarray detection. *Analytical Chemistry*, 76(7):1824–1831, 2004.

[10] Giles H. W. Sanders and Andreas Manz. Chip-based microsystems for genomic and proteomic analysis. *TrAC Trends in Analytical Chemistry*, 19(6):364–378, 2000.

[11] Stephane Mouradian. Lab-on-a-chip: applications in proteomics. *Current Opinion in Chemical Biology*, 6(1):51–56, 2002.

[12] Bernhard H. Weigl, Ron L. Bardell, and Catherine R. Cabrera. Lab-on-a-chip for drug development. *Advanced Drug Delivery Reviews*, 55(3):349–377, 2003.

[13] Harold Craighead. Future lab-on-a-chip technologies for interrogating individual molecules. *Nature*, 442(7101):387–393, 2006.

[14] Joerg Schotter, Astrit Shoshi, and Hubert Brueckl. Development of a magnetic lab-on-a-chip for point-of-care sepsis diagnosis. *Journal of Magnetism and Magnetic Materials*, 321(10):1671–1675, 2009.

[15] Curtis D. Chin, Vincent Linder, and Samuel K. Sia. Lab-on-a-chip devices for global health: Past studies and future opportunities. *Lab on a Chip*, 7(1):41–57, 2007.

[16] G. M. Whitesides. The origins and the future of microfluidics. *Nature*, 442(7101):368–373, 2006.

[17] C. Monat, P. Domachuk, and B. J. Eggleton. Integrated optofluidics: A new river of light. *Nature Photonics*, 1(2):106–114, 2007.

[18] Mark L. Adams, Markus Enzelberger, Stephen Quake, and Axel Scherer. Microfluidic integration on detector arrays for absorption and fluorescence micro-spectrometers. *Sensors and Actuators A: Physical*, 104(1):25–31, 2003.

[19] Arthur Nitkowski, Long Chen, and Michal Lipson. Cavity-enhanced on-chip absorption spectroscopy using microring resonators. *Opt. Express*, 16(16):11930–11936, 2008.

[20] Miao Wang, Nan Jing, I. Hsien Chou, Gerard L. Cote, and Jun Kameoka. An optofluidic device for surface enhanced raman spectroscopy. *Lab on a Chip*, 7(5):630–632, 2007.

[21] A. M. Armani, R. P. Kulkarni, S. E. Fraser, R. C. Flagan, and K. J. Vahala.

Label-free, single-molecule detection with optical microcavities. *Science*, 317(5839):783–787, 2007.

[22] I. M. White, H. Zhu, J. D. Suter, N. M. Hanumegowda, H. Oveys, M. Zourob, and X. Fan. Refractometric sensors for lab-on-a-chip based on optical ring resonators. *Sensors Journal, IEEE*, 7(1):28–35, 2007.

[23] Lukas Novak, Pavel Neuzil, Juergen Pipper, Yi Zhang, and Shinhan Lee. An integrated fluorescence detection system for lab-on-a-chip applications. *Lab on a Chip*, 7(1):27–29, 2007.

[24] A. H. J. Yang, S. D. Moore, B. S. Schmidt, M. Klug, M. Lipson, and D. Erickson. Optical manipulation of nanoparticles and biomolecules in sub-wavelength slot waveguides. *Nature*, 457(7225):71–75, 2009.

[25] David C. Duffy, J. Cooper McDonald, Olivier J. A. Schueller, and George M. Whitesides. Rapid prototyping of microfluidic systems in poly(dimethylsiloxane). *Analytical Chemistry*, 70(23):4974–4984, 1998.

[26] Teruo Fujii. Pdms-based microfluidic devices for biomedical applications. *Microelectronic Engineering*, 61-62:907–914, 2002.

[27] Chung-Cheng Lee, Guodong Sui, Arkadij Elizarov, Chengyi Jenny Shu, Young-Shik Shin, Alek N. Dooley, Jiang Huang, Antoine Daridon, Paul Wyatt, David Stout, Hartmuth C. Kolb, Owen N. Witte, Nagichettiar Satyamurthy, James R. Heath, Michael E. Phelps, Stephen R. Quake, and Hsian-Rong Tseng. Multistep synthesis of a radiolabeled imaging probe using integrated microfluidics. *Science*, 310(5755):1793–1796, 2005.

[28] Nikolas Chronis, Gang Liu, Ki-Hun Jeong, and Luke Lee. Tunable liquid-filled microlens array integrated with microfluidic network. *Opt. Express*, 11(19):2370–2378, 2003.

[29] J. Cooper McDonald and George M. Whitesides. Poly(dimethylsiloxane) as a material for fabricating microfluidic devices. *Accounts of Chemical Research*, 35(7):491–499, 2002.

[30] Marc A. Unger, Hou-Pu Chou, Todd Thorsen, Axel Scherer, and Stephen R. Quake. Monolithic microfabricated valves and pumps by multilayer soft lithography. *Science*, 288(5463):113–116, 2000.

[31] Timothy J. Johnson, David Ross, and Laurie E. Locascio. Rapid microfluidic mixing. *Analytical Chemistry*, 74(1):45–51, 2001.

[32] Hao Chen and Jens-Christian Meiners. Topologic mixing on a microfluidic chip. *Applied Physics Letters*, 84(12):2193–2195, 2004.

[33] Todd M. Squires and Stephen R. Quake. Microfluidics: Fluid physics at the nanoliter scale. *Reviews of Modern Physics*, 77(3):977, 2005.

[34] Andrew Evan Kamholz and Paul Yager. Theoretical analysis of molecular diffusion in pressure-driven laminar flow in microfluidic channels. *Biophysical Journal*, 80(1):155–160, 2001.

[35] Philippe Lam, Kenneth J. Wynne, and Gary E. Wnek. Surface-tension-confined microfluidics. *Langmuir*, 18(3):948–951, 2002.

[36] S. K. Sia and G. M. Whitesides. Microfluidic devices fabricated in poly(dimethylsiloxane) for biological studies. *Electrophoresis*, 24(21):3563–3576, 2003.

[37] Hiroshi Nishihara, Masamitsu Haruna, and Toshiaki Suhara. *Optical integrated circuits*. McGraw-Hill optical and electro-optical engineering series. McGraw-Hill Book Co., New York, 1989.

[38] Robert G. Hunsperger. *Integrated optics : theory and technology*. Springer, New York; London, 2009.

[39] Paras N. Prasad. *Nanophotonics*. Wiley, Hoboken, NJ, 2004.

[40] P.V. Lambeck and H.J.W.M. Hoekstra. Integrated optical sensors, 2003 2003.

[41] Wim Bogaerts, Roel Baets, Pieter Dumon, Vincent Wiaux, Stephan Beckx, Dirk Taillaert, Bert Luyssaert, Joris Van Campenhout, Peter Bienstman, and Dries Van Thourhout. Nanophotonic waveguides in silicon-on-insulator fabricated with cmos technology. *J. Lightwave Technol.*, 23(1):401, 2005.

[42] Yusheng Qian, Jiguo Song, Seunghyun Kim, and Gregory P. Nordin. Compact 90 trench-based splitter for silicon-on-insulator rib waveguides. *Opt. Express*, 15(25):16712–16718, 2007.

[43] F. Van Laere, G. Roelkens, M. Ayre, J. Schrauwen, D. Taillaert, D. Van Thourhout, T. F. Krauss, and R. Baets. Compact and highly efficient grating couplers between optical fiber and nanophotonic waveguides. *Lightwave Technology, Journal of*, 25(1):151–156, 2007.

[44] Vilson R. Almeida, Roberto R. Panepucci, and Michal Lipson. Nanotaper for compact mode conversion. *Optics Letters*, 28(15):1302–1304, 2003.

[45] Yurii Vlasov, William M. J. Green, and Fengnian Xia. High-throughput silicon nanophotonic wavelength-insensitive switch for on-chip optical networks. *Nat Photon*, 2(4):242–246, 2008.

[46] Ling Liao, Dean Samara-Rubio, Michael Morse, Ansheng Liu, Dexter Hodge, Doron Rubin, Ulrich Keil, and Thorkild Franck. High speed silicon mach-zehnder modulator. *Opt. Express*, 13(8):3129–3135, 2005.

[47] Qianfan Xu, Bradley Schmidt, Sameer Pradhan, and Michal Lipson. Micrometre-scale silicon electro-optic modulator. *Nature*, 435(7040):325–327, 2005.

[48] J. Van Campenhout, P. Rojo Romeo, P. Regreny, C. Seassal, D. Van Thourhout, S. Verstuyft, L. Di Cioccio, J. M. Fedeli, C. Lagahe, and R. Baets. Electrically pumped inp-based microdisk lasers integrated with a nanophotonic silicon-on-insulator waveguide circuit. *Opt. Express*, 15(11):6744–6749, 2007.

[49] Mark A. Foster, Amy C. Turner, Jay E. Sharping, Bradley S. Schmidt, Michal Lipson, and Alexander L. Gaeta. Broad-band optical parametric gain on a silicon photonic chip. *Nature*, 441(7096):960–963, 2006.

[50] Long Chen and Michal Lipson. Ultra-low capacitance and high speed germaniumphotodetectors on silicon. *Opt. Express*, 17(10):7901–7906, 2009.

[51] L. M. Johnson, F. J. Leonberger, and Jr. G. W. Pratt. Integrated optical temperature sensor. *Applied Physics Letters*, 41(2):134–136, 1982.

[52] M.N. Weiss, R. Srivastava, and H. Groger. Experimental investigation of a surface plasmon-based integrated-optic humidity sensor. *Electronics Letters*, 32(9):842–843, 1996.

[53] Masashi Ohkawa, Masayuki Izutsu, and Tadasi Sueta. Integrated optic pressure sensor on silicon substrate. *Appl. Opt.*, 28(23):5153–5157, 1989.

[54] Michal Lipson. Guiding, modulating, and emitting light on silicon-challenges and opportunities. *J. Lightwave Technol.*, 23(12):4222, 2005.

[55] Olivier Parriaux and G. J. Veldhuis. Normalized analysis for the sensitivity optimization of integrated optical evanescent-wave sensors. *J. Lightwave Technol.*, 16(4):573, 1998.

[56] Daoxin Dai, Yaocheng Shi, and Sailing He. Comparative study of the integration density for passive linear planar light-wave circuits based on three different kinds of nanophotonic waveguide. *Appl. Opt.*, 46(7):1126–1131, 2007.

[57] Klaus B. Mogensen, Peter Friis, Jrg Hbner, Nickolaj Petersen, Anders M. Jrgensen, Pieter Telleman, and Jrg P. Kutter. Ultraviolet transparent silicon oxynitride waveguides for biochemical microsystems. *Opt. Lett.*, 26(10):716–718, 2001.

[58] F. C. Chang and G. S. Kino. Nitrogen-rich silicon nitride thin films for deep-ultraviolet mirau interferometry. *Opt. Lett.*, 22(8):492–494, 1997.

[59] Keiichiro Fuwa and B. L. Valle. The physical basis of analytical atomic absorption spectrometry. the pertinence of the beer-lambert law. *Analytical Chemistry*, 35(8):942–946, 1963.

[60] Richard Engeln, Giel Berden, Rudy Peeters, and Gerard Meijer. Cavity enhanced absorption and cavity enhanced magnetic rotation spectroscopy. *Review of Scientific Instruments*, 69(11):3763–3769, 1998.

[61] Steve Blair and Yan Chen. Resonant-enhanced evanescent-wave fluorescence biosensing with cylindrical optical cavities. *Appl. Opt.*, 40(4):570–582, 2001.

[62] Kerry J. Vahala. Optical microcavities. *Nature*, 424(6950):839–846, 2003.

[63] John E. Heebner, Robert W. Boyd, and Q. Han Park. Scissor solitons and other novel propagation effects in microresonator-modified waveguides. *J. Opt. Soc. Am. B*, 19(4):722–731, 2002.

[64] Viktor A. Podolskiy and Evgenii E. Narimanov. Chaos-assisted tunneling in dielectric microcavities. *Opt. Lett.*, 30(5):474–476, 2005.

[65] eacute, J. M. rard, B. Sermage, B. Gayral, B. Legrand, E. Costard, and

V. Thierry-Mieg. Enhanced spontaneous emission by quantum boxes in a monolithic optical microcavity. *Physical Review Letters*, 81(5):1110, 1998.

[66] E. Krioukov, D. J. W. Klunder, A. Driessen, J. Greve, and C. Otto. Sensor based on an integrated optical microcavity. *Opt. Lett.*, 27(7):512–514, 2002.

[67] A. Yariv. Universal relations for coupling of optical power between microresonators and dielectric waveguides. *Electronics Letters*, 36(4):321–322, 2000.

[68] D. G. Rabus. *Integrated ring resonators the compendium*. Springer series in optical sciences, 127. Springer, Berlin; New York, 2007.

[69] Joseph Thomas Verdeyen. *Laser electronics*. Prentice-Hall, Englewood Cliffs, N.J., 1981.

[70] P. Rabiei, W. H. Steier, C. Zhang, and L. R. Dalton. Polymer micro-ring filters and modulators. *Journal of Lightwave Technology*, 20(11):1968–1975, 2002.

[71] Arthur Nitkowski, Alexander Gondarenko, and Michal Lipson. On-chip supercontinuum optical trapping and resonance excitation of microspheres. *Opt. Lett.*, 35(10):1626–1628, 2010.

[72] A. Ashkin and J. M. Dziedzic. Optical trapping and manipulation of viruses and bacteria. *Science*, 235(4795):1517–1520, 1987.

[73] D. Psaltis, S. R. Quake, and C. H. Yang. Developing optofluidic technology through the fusion of microfluidics and optics. *Nature*, 442(7101):381–386, 2006.

[74] S. Kuhn, P. Measor, E. J. Lunt, B. S. Phillips, D. W. Deamer, A. R. Hawkins, and H. Schmidt. Loss-based optical trap for on-chip particle analysis. *Lab on a Chip*, 9(15):2212–2216, 2009.

[75] X. Y. Miao, B. K. Wilson, S. H. Pun, and L. Y. Lin. Optical manipulation of micron/submicron sized particles and biomolecules through plasmonics. *Optics Express*, 16(18):13517–13525, 2008.

[76] B. S. Schmidt, A. H. J. Yang, D. Erickson, and M. Lipson. Optofluidic trapping and transport on solid core waveguides within a microfluidic device. *Optics Express*, 15(22):14322–14334, 2007.

[77] D. L. Yin, E. J. Lunt, M. I. Rudenko, D. W. Deamer, A. R. Hawkins, and H. Schmidt. Planar optofluidic chip for single particle detection, manipulation, and analysis. *Lab on a Chip*, 7(9):1171–1175, 2007.

[78] A. Ashkin. Forces of a single-beam gradient laser trap on a dielectric sphere in the ray optics regime. *Biophysical Journal*, 61(2):569–582, 1992.

[79] Alexander Gondarenko, Jacob S. Levy, and Michal Lipson. High confinement micron-scale silicon nitride high q ring resonator. *Opt. Express*, 17(14):11366–11370, 2009.

[80] I. Zeylikovich, V. Kartazaev, and R. R. Alfano. Spectral, temporal, and coherence properties of supercontinuum generation in microstructure fiber. *Journal of the Optical Society of America B-Optical Physics*, 22(7):1453–1460, 2005.

[81] Y. Liu, G. J. Sonek, M. W. Berns, and B. J. Tromberg. Physiological monitoring of optically trapped cells: Assessing the effects of confinement by 1064-nm laser tweezers using microfluorometry. *Biophysical Journal*, 71(4):2158–2167, 1996.

[82] S. Gaugiran, S. Getin, J. M. Fedeli, and J. Derouard. Polarization and particle size dependence of radiative forces on small metallic particles in evanescent optical fields. evidences for either repulsive or attractive gradient forces. *Optics Express*, 15(13):8146–8156, 2007.

[83] C. C. Lam, P. T. Leung, and K. Young. Explicit asymptotic formulas for the positions, widths, and strengths of resonances in mie scattering. *Journal of the Optical Society of America B-Optical Physics*, 9(9):1585–1592, 1992.

[84] P. Li, K. B. Shi, and Z. W. Liu. Optical scattering spectroscopy by using tightly focused supercontinuum. *Optics Express*, 13(22):9039–9044, 2005.

[85] K. B. Shi, P. Li, and Z. W. Liu. Broadband coherent anti-stokes raman scattering spectroscopy in supercontinuum optical trap. *Applied Physics Letters*, 90(14):3, 2007.

[86] F. Vollmer, D. Braun, A. Libchaber, M. Khoshsima, I. Teraoka, and S. Arnold. Protein detection by optical shift of a resonant microcavity. *Applied Physics Letters*, 80(21):4057–4059, 2002.

[87] D. Erickson. Special issue on "optofluidics". *Microfluidics and Nanofluidics*, 4(1-2):1–2, 2008.

[88] C. Y. Chao, W. Fung, and L. J. Guo. Polymer microring resonators for biochemical sensing applications. *Ieee Journal of Selected Topics in Quantum Electronics*, 12(1):134–142, 2006.

[89] J. J. Hu, V. Tarasov, A. Agarwal, L. Kimerling, N. Carlie, L. Petit, and K. Richardson. Fabrication and testing of planar chalcogenide waveguide integrated microfluidic sensor. *Optics Express*, 15(5):2307–2314, 2007.

[90] M. L. Chabinyc, D. T. Chiu, J. C. McDonald, A. D. Stroock, J. F. Christian, A. M. Karger, and G. M. Whitesides. An integrated fluorescence detection system in poly(dimethylsiloxane) for microfluidic applications. *Analytical Chemistry*, 73(18):4491–4498, 2001.

[91] J. Dostalek, J. Ctyroky, J. Homola, E. Brynda, M. Skalsky, P. Nekvindova, J. Spirkova, J. Skvor, and J. Schrofel. Surface plasmon resonance biosensor based on integrated optical waveguide. *Sensors and Actuators B-Chemical*, 76(1-3):8–12, 2001.

[92] K. Schmitt, B. Schirmer, C. Hoffmann, A. Brandenburg, and P. Meyrueis. Interferometric biosensor based on planar optical waveguide sensor chips for label-free detection of surface bound bioreactions. *Biosensors & Bioelectronics*, 22(11):2591–2597, 2007.

[93] W. G. Yang, D. B. Conkey, B. Wu, D. L. Yin, A. R. Hawkins, and H. Schmidt. Atomic spectroscopy on a chip. *Nature Photonics*, 1(6):331–335, 2007.

[94] N. A. Mortensen, S. S. Xiao, and J. Pedersen. Liquid-infiltrated photonic crystals: enhanced light-matter interactions for lab-on-a-chip applications. *Microfluidics and Nanofluidics*, 4(1-2):117–127, 2008.

[95] A. R. Hawkins and H. Schmidt. Optofluidic waveguides: Ii. fabrication and structures. *Microfluidics and Nanofluidics*, 4(1-2):17–32, 2008.

[96] A. M. Armani and K. J. Vahala. Heavy water detection using ultra-high-q microcavities. *Optics Letters*, 31(12):1896–1898, 2006.

[97] R. W. Boyd and J. E. Heebner. Sensitive disk resonator photonic biosensor. *Applied Optics*, 40(31):5742–5747, 2001.

[98] G. Farca, S. I. Shopova, and A. T. Rosenberger. Cavity-enhanced laser absorption spectroscopy using microresonator whispering-gallery modes. *Optics Express*, 15(25):17443–17448, 2007.

[99] M. A. Belkin, M. Loncar, B. G. Lee, C. Pflugl, R. Audet, L. Diehl, F. Capasso, D. Bour, S. Corzine, and G. Hofler. Intra-cavity absorption spectroscopy with narrow-ridge microfluidic quantum cascade lasers. *Optics Express*, 15(18):11262–11271, 2007.

[100] Chuanmin Hu, Frank E. Muller-Karger, and Richard G. Zepp. Absorbance, absorption coefficient, and apparent quantum yield: A comment on common ambiguity in the use of these optical concepts. *Limnology and Oceanography*, 47(4):1261–1267, 2002.

[101] A. Yariv. Critical coupling and its control in optical waveguide-ring resonator systems. *Ieee Photonics Technology Letters*, 14(4):483–485, 2002.

[102] J. T. Robinson, L. Chen, and M. Lipson. On-chip gas detection in silicon optical microcavities. *Optics Express*, 16(6):4296–4301, 2008.

[103] Arthur Nitkowski, Antje Baeumner, and Michal Lipson. On-chip spectrophotometry for bioanalysis using microring resonators. *Biomed. Opt. Express*, 2(2):271–277, 2011.

[104] Yeshaiahu Fainman, Luke Lee, Demetri Psaltis, and Changhuei Yang. *Optofluidics: Fundamentals, Devices, and Applications*. McGraw-Hill, Inc., 2010.

[105] A. Fleck and H. N. Munro. The precision of ultraviolet absorption measurements in the schmidt-thannhauser procedure for nucleic acid estimation. *Biochimica et Biophysica Acta*, 55(5):571–583, 1962.

[106] William E. Groves, Francis C. Davis, and Bruce H. Sells. Spectrophotometric determination of microgram quantities of protein without nucleic acid interference. *Analytical Biochemistry*, 22(2):195–210, 1968.

[107] Tim Mosmann. Rapid colorimetric assay for cellular growth and survival: Application to proliferation and cytotoxicity assays. *Journal of Immunological Methods*, 65(1-2):55–63, 1983.

[108] M. Manafi, W. Kneifel, and S. Bascomb. Fluorogenic and chromogenic

substrates used in bacterial diagnostics. *Microbiological Reviews*, 55(3):335–348, 1991.

[109] V. M. Cooke, R. J. Miles, R. G. Price, and A. C. Richardson. A novel chromogenic ester agar medium for detection of salmonellae. *Applied and Environmental Microbiology*, 65(2):807–812, 1999.

[110] Ehsan Shah Hosseini, Siva Yegnanarayanan, Amir H. Atabaki, Mohammad Soltani, and Ali Adibi. High quality planar silicon nitride microdisk resonators for integratedphotonics in the visible wavelength range. *Opt. Express*, 17(17):14543–14551, 2009.

[111] Juejun Hu, Nathan Carlie, Laeticia Petit, Anu Agarwal, Kathleen Richardson, and Lionel C. Kimerling. Cavity-enhanced ir absorption in planar chalcogenide glass microdisk resonators: Experiment and analysis. *J. Lightwave Technol.*, 27(23):5240–5245, 2009.

[112] Alan Waggoner. Fluorescent labels for proteomics and genomics. *Current Opinion in Chemical Biology*, 10(1):62–66, 2006.

[113] J. R. Crowther. Elisa. theory and practice. *Methods Mol Biol*, 42:1–218, 1995.

[114] M. M. Mesulam. Tetramethyl benzidine for horseradish-peroxidase neuro-histochemistry - non-carcinogenic blue reaction-product with superior sensitivity for visualizing neural afferents and efferents. *Journal of Histochemistry & Cytochemistry*, 26(2):106–117, 1978.

[115] C. A. Barrios, K. B. Gylfason, B. Sanchez, A. Griol, H. Sohlstrom, M. Holgado, and R. Casquel. Slot-waveguide biochemical sensor. *Optics Letters*, 32(21):3080–3082, 2007.

[116] N. Jokerst, M. Royal, S. Palit, L. Luan, S. Dhar, and T. Tyler. Chip scale integrated microresonator sensing systems. *Journal of Biophotonics*, 2(4):212–226, 2009.

[117] J. N. Lee, C. Park, and G. M. Whitesides. Solvent compatibility of poly(dimethylsiloxane)-based microfluidic devices. *Analytical Chemistry*, 75(23):6544–6554, 2003.

[118] P. Heimala, P. Katila, J. Aarnio, and A. Heinamaki. Thermally tunable integrated optical ring resonator with poly-si thermistor. *Lightwave Technology, Journal of*, 14(10):2260–2267, 1996.

[119] David M. Rissin, Cheuk W. Kan, Todd G. Campbell, Stuart C. Howes, David R. Fournier, Linan Song, Tomasz Piech, Purvish P. Patel, Lei Chang, Andrew J. Rivnak, Evan P. Ferrell, Jeffrey D. Randall, Gail K. Provuncher, David R. Walt, and David C. Duffy. Single-molecule enzyme-linked immunosorbent assay detects serum proteins at subfemtomolar concentrations. *Nat Biotech*, 28(6):595–599, 2010.

[120] C F Niven Jr, M B Jeffrey, and D A Corlett Jr. Differential plating medium for quantitative detection of histamine-producing bacteria. *Applied and Environmental Microbiology*, 41(1):321–322, 1981.

[121] M A Jensen, J A Webster, and N Straus. Rapid identification of bacteria on the basis of polymerase chain reaction-amplified ribosomal dna spacer polymorphisms. *Applied and Environmental Microbiology*, 59(4):945–952, 1993.

[122] Douglas A. Boehm, Philip A. Gottlieb, and Susan Z. Hua. On-chip microfluidic biosensor for bacterial detection and identification. *Sensors and Actuators B: Chemical*, 126(2):508–514, 2007.

[123] Shoshana Bascomb and Mammad Manafi. Use of enzyme tests in characterization and identification of aerobic and facultatively anaerobic gram-positive cocci. *Clin. Microbiol. Rev.*, 11(2):318–340, 1998.

[124] Karin Y. Gfeller, Natalia Nugaeva, and Martin Hegner. Rapid biosensor for detection of antibiotic-selective growth of escherichia coli. *Applied and Environmental Microbiology*, 71(5):2626–2631, 2005.

[125] Peter Roslev and Gary M. King. Application of a tetrazolium salt with a water-soluble formazan as an indicator of viability in respiring bacteria. *Applied and Environmental Microbiology*, 59(9):2891–2896, 1993.

[126] Anouar Bensaid, Jacques Thierie, and Michel Penninckx. The use of the tetrazolium salt xtt for the estimation of biological activity of activated sludge cultivated under steady-state and transient regimes. *Journal of Microbiological Methods*, 40(3):255–263, 2000.

[127] Tova Meshulam, Stuart M. Levitz, Laurent Christin, and Richard D. Diamond. A simplified new assay for assessment of fungal cell damage with the tetrazolium dye, (2,3)-bis-(2-methoxy-4-nitro-5-sulphenyl)-(2h)-tetrazolium-5-carboxanilide (xtt). *The Journal of Infectious Diseases*, 172(4):1153–1156, 1995.

[128] Dominic A. Scudiero, Robert H. Shoemaker, Kenneth D. Paull, Anne Monks, Siobhan Tierney, Thomas H. Nofziger, Michael J. Currens, Donna Seniff, and Michael R. Boyd. Evaluation of a soluble tetrazolium/formazan assay for cell growth and drug sensitivity in culture using human and other tumor cell lines. *Cancer Research*, 48(17):4827–4833, 1988.

[129] Nuno Cerca, Silvia Martins, Filipe Cerca, Kimberly K. Jefferson, Gerald B. Pier, Rosrio Oliveira, and Joana Azeredo. Comparative assessment of antibiotic susceptibility of coagulase-negative staphylococci in biofilm versus planktonic culture as assessed by bacterial enumeration or rapid xtt colorimetry. *Journal of Antimicrobial Chemotherapy*, 56(2):331–336, 2005.

[130] Magdalena S. Nawrocka, Tao Liu, Xuan Wang, and Roberto R. Panepucci. Tunable silicon microring resonator with wide free spectral range. *Applied Physics Letters*, 89(7):071110, 2006.

[131] F. Trager. *Springer handbook of lasers and optics*. Springer, New York, 2007.

[132] Gustavo S. Wiederhecker, Long Chen, Alexander Gondarenko, and Michal Lipson. Controlling photonic structures using optical forces. *Nature*, 462(7273):633–636, 2009.

[133] Tryggve Baak. Silicon oxynitride; a material for grin optics. *Appl. Opt.*, 21(6):1069–1072, 1982.

[134] Marvin J. Weber. *Handbook of optical materials*. The CRC Press laser and optical science and technology series. CRC Press, Boca Raton, 2003.

[135] H. M. H. Chong and R. M. De La Rue. Tuning of photonic crystal waveguide microcavity by thermooptic effect. *Photonics Technology Letters, IEEE*, 16(6):1528–1530, 2004.

[136] W. M. Yim and R. J. Paff. Thermal expansion of aln, sapphire, and silicon. *Journal of Applied Physics*, 45(3):1456–1457, 1974.

[137] Allan Harvey, J. S. Gallagher, and Levelt Sengers. Revised formulation for the refractive index of water and steam as a function of wavelength, temperature and density. *Journal of Physical and Chemical Reference Data*, 27(4):761–774, 1998.

[138] Neal W. Roehm, George H. Rodgers, Stephen M. Hatfield, and Andrew L.

Glasebrook. An improved colorimetric assay for cell proliferation and viability utilizing the tetrazolium salt xtt. *Journal of Immunological Methods*, 142(2):257–265, 1991.

[139] Bing He, Brian J. Burke, Xiang Zhang, Roujian Zhang, and Fred E. Regnier. A picoliter-volume mixer for microfluidic analytical systems. *Analytical Chemistry*, 73(9):1942–1947, 2001.

[140] N. Reginald Beer, Benjamin J. Hindson, Elizabeth K. Wheeler, Sara B. Hall, Klint A. Rose, Ian M. Kennedy, and Bill W. Colston. On-chip, real-time, single-copy polymerase chain reaction in picoliter droplets. *Analytical Chemistry*, 79(22):8471–8475, 2007.

[141] D. Huang, E. A. Swanson, C. P. Lin, J. S. Schuman, W. G. Stinson, W. Chang, M. R. Hee, T. Flotte, K. Gregory, and C. A. Puliafito. Optical coherence tomography. *Science (New York, N.Y.)*, 254(5035):1178–81, 1991.

[142] G. Humbert, W. Wadsworth, S. Leon-Saval, J. Knight, T. Birks, P. St. J. Russell, M. Lederer, D. Kopf, K. Wiesauer, E. Breuer, and D. Stifter. Supercontinuum generation system for optical coherence tomography based on tapered photonic crystal fibre. *Opt. Express*, 14(4):1596–1603, 2006.

[143] Vivek Ranjan Sinha, V. Goyal, J. R. Bhinge, B. R. Mittal, and A. Trehan. Diagnostic microspheres: An overview. 20(6):28, 2003.

[144] Adrian Goodey, John J. Lavigne, Steve M. Savoy, Marc D. Rodriguez, Theodore Curey, Andrew Tsao, Glen Simmons, John Wright, Seung-Jin Yoo, Youngsoo Sohn, Eric V. Anslyn, Jason B. Shear, Dean P. Neikirk, and John T. McDevitt. Development of multianalyte sensor arrays composed of chemically derivatized polymeric microspheres localized in micromachined cavities. *Journal of the American Chemical Society*, 123(11):2559–2570, 2001.

[145] Z. Wang, J. El-Ali, M. Engelund, T. Gotsaed, I. R. Perch-Nielsen, K. B. Mogensen, D. Snakenborg, J. P. Kutter, and A. Wolff. Measurements of scattered light on a microchip flow cytometer with integrated polymer based optical elements. *Lab on a Chip*, 4(4):372–377, 2004.

[146] David P. Schrum, Christopher T. Culbertson, Stephen C. Jacobson, and J. Michael Ramsey. Microchip flow cytometry using electrokinetic focusing. *Analytical Chemistry*, 71(19):4173–4177, 1999.

[147] Rigo Pantoja, John M. Nagarah, Dorine M. Starace, Nicholas A. Melosh, Rikard Blunck, Francisco Bezanilla, and James R. Heath. Silicon chip-based patch-clamp electrodes integrated with pdms microfluidics. *Biosensors and Bioelectronics*, 20(3):509–517, 2004.

[148] Y. Ozaki, W. F. McClure, and Alfred A. Christy. *Near-infrared spectroscopy in food science and technology*. Wiley-Interscience, Hoboken, N.J., 2007.

[149] J. Luypaert, D. L. Massart, and Y. Vander Heyden. Near-infrared spectroscopy applications in pharmaceutical analysis. *Talanta*, 72(3):865–883, 2007.

[150] Frank S. Parker. *Applications of infrared spectroscopy in biochemistry, biology, and medicine*. Plenum Press, New York, 1971.

[151] Tom Baehr-Jones, Alexander Spott, Rob Ilic, Andrew Spott, Boyan Penkov, William Asher, and Michael Hochberg. Silicon-on-sapphire integrated waveguides for the mid-infrared. *Opt. Express*, 18(12):12127–12135, 2010.

[152] Mark P. Hiscocks, Kumaravelu Ganesan, Brant C. Gibson, Shane T. Huntington, Franois Ladouceur, and Steven Prawer. Diamond waveguides fabricated by reactive ion etching. *Opt. Express*, 16(24):19512–19519, 2008.

[153] Sarah L. Westcott, Jiangquan Zhang, Robert K. Shelton, Nellie M. K. Bruce, Sachin Gupta, Steven L. Keen, Jeremy W. Tillman, Lara B. Wald, Brian N. Strecker, A. T. Rosenberger, Roy R. Davidson, Wei Chen, Kevin G. Donovan, and John V. Hryniewicz. Broadband optical absorbance spectroscopy using a whispering gallery mode microsphere resonator. *Review of Scientific Instruments*, 79(3):033106–033106–9, 2008.

[154] Edward Eteshola and Michal Balberg. Microfluidic elisa: On-chip fluorescence imaging. *Biomedical Microdevices*, 6(1):7–9, 2004.

[155] Shia-Yen Teh, Robert Lin, Lung-Hsin Hung, and Abraham P. Lee. Droplet microfluidics. *Lab on a Chip*, 8(2):198–220, 2008.